

**FREEZING OF SULFURIC ACID-WATER AND
NITRIC ACID-WATER AEROSOLS AT POLAR
STRATOSPHERIC TEMPERATURES**

by

Allan Kent Bertram

A thesis
presented to the University of Waterloo
in fulfilment of the
thesis requirement for the degree of
Doctor of Philosophy
in
Chemistry

Waterloo, Ontario, Canada, 1998

© Allan Kent Bertram, 1998



National Library
of Canada

Acquisitions and
Bibliographic Services

395 Wellington Street
Ottawa ON K1A 0N4
Canada

Bibliothèque nationale
du Canada

Acquisitions et
services bibliographiques

395, rue Wellington
Ottawa ON K1A 0N4
Canada

Your file Votre référence

Our file Notre référence

The author has granted a non-exclusive licence allowing the National Library of Canada to reproduce, loan, distribute or sell copies of this thesis in microform, paper or electronic formats.

The author retains ownership of the copyright in this thesis. Neither the thesis nor substantial extracts from it may be printed or otherwise reproduced without the author's permission.

L'auteur a accordé une licence non exclusive permettant à la Bibliothèque nationale du Canada de reproduire, prêter, distribuer ou vendre des copies de cette thèse sous la forme de microfiche/film, de reproduction sur papier ou sur format électronique.

L'auteur conserve la propriété du droit d'auteur qui protège cette thèse. Ni la thèse ni des extraits substantiels de celle-ci ne doivent être imprimés ou autrement reproduits sans son autorisation.

0-612-38220-6

Canada

The University of Waterloo requires the signatures of all persons using or photocopying this thesis. Please sign below, and give address and date.

ABSTRACT

The freezing of H₂SO₄-H₂O and HNO₃-H₂O particles of sub-micron diameter was measured using FTIR extinction spectroscopy and a low-temperature flow tube. Temperatures ranging from approximately 190 K to approximately 150 K were employed in the HNO₃-H₂O experiments, and temperatures from approximately 240 K to approximately 180 K were employed in the H₂SO₄-H₂O experiments.

In dilute H₂SO₄-H₂O particles (<35 wt % H₂SO₄), ice formed at approximately 35 K below the corresponding solid-liquid equilibrium temperatures. The freezing temperatures of these particles are in reasonable agreement with theoretical calculations and other experimental data. The homogeneous nucleation rate associated with our freezing temperatures is between $1 \times 10^9 \text{ cm}^{-3} \text{ sec}^{-1}$ and $4 \times 10^{10} \text{ cm}^{-3} \text{ sec}^{-1}$. In contrast to dilute H₂SO₄-H₂O aerosols, concentrated H₂SO₄-H₂O aerosols (>35 wt % H₂SO₄) did not freeze. From the experimental results, an upper limit of $4 \times 10^{10} \text{ cm}^{-3} \text{ sec}^{-1}$ was calculated for the nucleation rate. This result agrees with other laboratory results on this system and the suggestion that stratospheric sulfate aerosols are liquid.

Nitric acid-water aerosols with compositions of 2:1 (moles H₂O:moles HNO₃) and 3:1 froze as NAD and NAT, respectively. The measured nucleation rate constants for the 2:1 particles are between (in units of $\text{cm}^{-3} \text{ s}^{-1} \times 10^{11}$) 0.26 ± 0.05 and 16 ± 9 at temperatures between 178.8 and 175.8. The rates for 3:1 particles are between (in units of $\text{cm}^{-3} \text{ s}^{-1} \times 10^{11}$) 0.38 ± 0.18 and 97 ± 63 at temperatures ranging from 167.2 K to 163.5 K. Freezing of non-stoichiometric nitric acid aerosols was also investigated. Aerosols with compositions ranging from 1.2 to 1.4 did not crystallize at any of the temperatures investigated. NAD formed in particles with compositions ranging from 1.4:1 to 2:1, and both NAD and NAT formed in aerosols with compositions ranging from 2.7:1 to 3:1. The highest freezing temperature in this composition range (1.2:1 to 3:1) corresponds to a composition of approximately 2:1. Based on this information and the nucleation rates determined from the 2:1 experiments, it is unlikely that concentrated nitric acid-water particles (1.2:1 to 3:1), if formed in the polar stratosphere, will freeze.

ACKNOWLEDGEMENTS

My five years at the University of Waterloo have been an extremely positive experience. One of the reasons for this has been Professor Jim Sloan, my supervisor. Jim has been a constant source of advice, encouragement, guidance, and, most of all, unconditional support. For these things I am eternally grateful. Thanks for everything Jim!

I would also like to thank Bill Neil, the Sloan group technician during my first 2-1/2 years at Waterloo. Bill, who was always available for advice and assistance, taught me many things about experimental physical chemistry.

Several other members of the Sloan group also deserve special recognition: Nicole August and Nancy Ford worked on the Mie scattering code discussed in this thesis. Dawn Patterson assisted in the sulfuric acid experiments, and both Dustin Dickens and Jessie Rowsell helped with some of the nitric acid experiments. To these people, I am indebted. I would also like to thank the rest of members of the Sloan group (past and present) for fruitful discussions, assistance, and their friendship.

Finally, I would like to thank the rest of the faculty, students, and staff of the chemistry department, for making my stay a pleasant and enjoyable one.

DEDICATION

To my parents for their continuous support.

TABLE OF CONTENTS

Abstract	(iv)
Acknowledgements	(v)
Dedication	(vi)
Table of Contents	(vii)
List of Figures and Tables	(ix)
Chapter One: Introduction	1
1.1 Introduction	1
1.2 Polar Stratospheric Clouds	3
1.3 Thesis Overview	5
Chapter Two: Kinetic Feasibility	6
2.1 Introduction	6
2.2 Homogeneous Nucleation	6
2.3 Crystal Growth	8
2.4 Freezing Rates	9
Chapter Three: General Experimental	11
3.1 Introduction	11
3.2 Freezing Experiments	11
3.3 IR spectroscopy	13
3.4 Aerosol Size Determination	14
Chapter Four: H₂SO₄-H₂O Aerosols	20
4.1 Introduction	20
4.2 Experimental	22
4.3 Size Determination	25
4.4 Concentration Determination	33

4.5 Dilute H ₂ SO ₄ -H ₂ O Aerosols	40
4.5.1 Results	40
4.5.2 Discussion	51
4.6 Concentrated H ₂ SO ₄ -H ₂ O Aerosols	53
4.6.1 Results	53
4.6.2 Discussion	57
Chapter Five: HNO₃-H₂O Aerosols	59
5.1 Introduction	59
5.2 Nitric Acid Dihydrate Aerosols	63
5.2.1 Experimental	63
5.2.2 Results	70
5.2.3 Discussion	77
5.3 Nitric Acid Trihydrate Aerosols	81
5.3.1 Experimental	82
5.3.2 Results	87
5.3.3 Discussion	90
5.4 Non-stoichiometric HNO ₃ -H ₂ O Aerosols	95
5.4.1 Experimental	95
5.4.2 Results	98
5.4.3 Discussion and Conclusions	112
Chapter Six: Concluding Remarks	115
6.1 Conclusions	115
6.2 Considerations for Further Work	116
References	118

LIST OF FIGURES AND TABLES

	<i>Figure</i>	<i>Page</i>
Chapter 1		
1.1	Schematic diagram representing the changes in composition and phase which could occur as the stratospheric aerosol cools.	(4)
Chapter 2		
2.1	Change in Gibbs Free Energy as a function of the embryo radius.	(7)
2.2	Overlap of the crystal growth rate and the nucleation rate for two chemically different systems.	(10)
Chapter 3		
3.1	Calculated extinction spectra of 0.1, 0.5, and 1.0 micron ice particles.	(16)
3.2	Contour plot generated for a sodium chloride aerosol.	(18)
Chapter 4		
4.1	The phase diagram of the sulfuric acid-water system.	(21)
4.2	Schematic diagram of the temperature-controlled flow tube used in the sulfuric acid-water experiments.	(24)
4.3	Spectra of 85 wt % H ₂ SO ₄ particles.	(27)
4.4	Contour plot generated for a 85 wt % H ₂ SO ₄ aerosol.	(28)
4.5	Contour plot generated for a calculated aerosol spectrum with parameters $r_g=0.25$ (μm) and $\sigma_g=1.4$.	(30)
4.6	Contour plot generated for a calculated aerosol spectrum with parameters $r_g=0.5$ (μm) and $\sigma_g=1.4$.	(31)
4.7	Contour plot generated for a calculated aerosol spectrum with parameters $r_g=1.0$ (μm) and $\sigma_g=1.4$.	(32)

- 4.8 Room-temperature spectrum of a 50 wt % H₂SO₄ aerosol. (34)
- 4.9 Infrared spectra of a 36 wt % H₂SO₄ aerosol at 237, 225, and 196 K. (36)
- 4.10 Room-temperature spectrum of a 50 wt % H₂SO₄ aerosol with size parameters of $r_g=0.36$ (μm) and $\sigma_g=1.0$. (38)
- 4.11 Calibration curves used to determine the H₂SO₄ particle concentration from the ratio of the hydroxyl and sulfate bands. (39)
- 4.12 Temperature dependence of the observed extinction spectrum of a 30 wt % H₂SO₄ aerosol. (41)
- 4.13 Subtraction of the two lowest extinction spectra in figure 4.12. (43)
- 4.14 Rate of change of the 3230 cm⁻¹ feature in figure 4.13. (46)
- 4.15 Freezing curve for dilute sulfuric acid aerosols. (48)
- 4.16 Comparison of theoretical freezing curves of dilute H₂SO₄ aerosols with experiments. (52)
- 4.17 The vertical lines represent the concentrations and temperatures used in the concentrated H₂SO₄ freezing measurements. (54)
- 4.18 Temperature dependent spectra of a 36 wt % H₂SO₄ aerosol. (55)
- 4.19 Temperature dependent spectra of a 60 wt % H₂SO₄ aerosol. (56)

Chapter 5

- 5.1 Expected composition of polar stratospheric aerosols as a function of temperature. (60)
- 5.2 Phase diagram of the nitric acid-water system. (62)
- 5.3 Schematic cross section of the double walled flow tube apparatus used in the NAD experiments. (64)
- 5.4 Low-temperature spectra used to determine the flows which produced a 2:1 H₂O:HNO₃ aerosol. (67)
- 5.5 Plot used to establish the flows which produced an exact 2:1 H₂O:HNO₃ aerosol in the flow tube. (69)
- 5.6 Changes in the absorbance spectrum of a 2:1 H₂O-HNO₃ aerosol upon freezing. (71)

5.7	An enlarged view of seven spectra chosen for the freezing point measurement of NAD.	(72)
5.8	Change in the OH region (3650 to 3100 cm^{-1}) of the 2:1 spectrum as a function of temperature.	(74)
5.9	Contour plot generated by comparing a measured NAD spectrum with calculated spectra of NAD particles.	(76)
5.10	Comparison of measured NAD spectrum with a calculated spectrum having the log-normal parameters indicated.	(78)
5.11	Comparison of the nucleation rates of NAD derived from measurements with values which have been calculated.	(80)
5.12	Low-temperature nitric acid trihydrate aerosol spectra.	(83)
5.13	Plot used to establish the flows which produced an exact 3:1 aerosol in the flow tube.	(84)
5.14	Schematic cross section of the flow tube is shown at the top of the figure. The temperature profiles used in the NAD and NAT experiments are at the bottom.	(86)
5.15	Changes in the absorbance spectra of a 3:1 aerosol upon freezing.	(88)
5.16	Change in the nitrate band of the 3:1 spectrum as a function of temperature.	(89)
5.17	Contour plot used to determine the log-normal size parameters of NAT aerosols.	(91)
5.18	Comparison of a measured NAT spectrum with a calculated spectrum of NAT.	(92)
5.19	Comparison of the rate constants reported here for NAT nucleation in a 3:1 aerosol with the nucleation of NAD in a 2:1 aerosol.	(93)
5.20	Schematic diagram of the apparatus used in the non-stoichiometric freezing experiments.	(97)
5.21	IR spectra of nitric acid and water vapors.	(99)
5.22	$\text{HNO}_3(\text{g})$ calibration curve for the non-stoichiometric experiments.	(100)
5.23	$\text{H}_2\text{O}(\text{g})$ calibration curves for the non-stoichiometric experiments.	(101)

5.24	Temperature dependent spectra of a HNO ₃ -H ₂ O aerosol with a composition of 1.2:1.	(102)
5.25	Comparison of a NAM spectrum with a spectrum of a 1.2:1 aerosol at 156 K.	(104)
5.26	Spectra of a H ₂ O-HNO ₃ aerosol with a composition of 1.6:1.	(105)
5.27	Spectra showing the result of subtracting a pure NAD spectrum from a spectrum of a 1.6:1 aerosol at 174.6 K.	(107)
5.28	Temperature dependent spectra of a H ₂ O-HNO ₃ aerosol with a composition of 2.8:1.	(108)
5.29	Spectra showing the result of subtracting a pure NAD spectrum from a spectrum of a 2.8:1 aerosol at 171.6 K.	(110)
5.30	Plot of the change in the OH region of a 2.8:1 spectrum as a function of temperature.	(111)
5.31	Freezing data from the stoichiometric and non-stoichiometric experiments.	(113)

Table

Page

Chapter 5

5.1	Nucleation rate constants in 2:1 solutions as a function of temperature.	(77)
-----	--	------

CHAPTER ONE

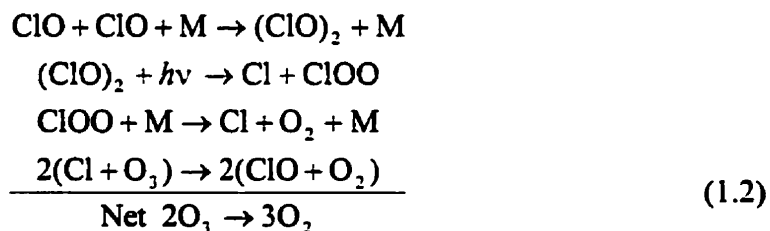
INTRODUCTION

1.1 INTRODUCTION

Prior to 1985, stratospheric ozone research focused on the gas-phase chemistry responsible for ozone destruction. This research identified man-made halocarbons, including several chlorofluorocarbons (CFCs), as the premier threat to the ozone layer.¹ Halocarbons migrate from the earth's surface to the stratosphere where they are photolyzed by ultraviolet light, producing chlorine and bromine radicals. The radicals then destroy ozone by several catalytic cycles, including the following:^{1,2}



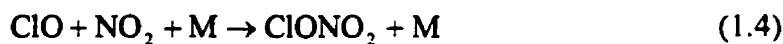
and



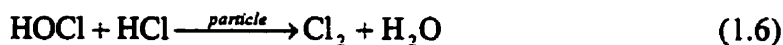
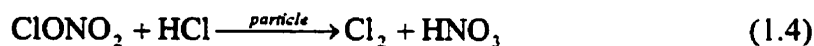
The 1985 publication of the discovery of very large depletions of stratospheric ozone over Antarctica in the springtime³ shocked the scientific community because the current gas phase models of ozone depletion were incapable of explaining these observations. This indicated that gas-phase chemistry alone was inadequate to represent stratospheric ozone destruction. An explosion of research followed the 1985 publication on the discovery of the Antarctic ozone hole. This research concluded that heterogeneous

reactions occurring on the surfaces of polar stratospheric clouds (PSCs) play an essential role in chlorofluorocarbon-induced polar ozone depletion.^{4,5,6,7}

Heterogeneous reactions contribute to ozone depletion by converting unreactive temporary reservoirs of chlorine into photolytically-active forms. Chlorine radicals produced from the photolysis of halocarbons can react with other trace stratospheric species to form unreactive compounds, commonly referred to as reservoir species. For example, chlorine radicals can react with methane or nitrogen dioxide to form HCl and ClONO₂, both of which are inert to ozone.



Ordinarily, a majority of the stratospheric inorganic chlorine is in these unreactive forms, and liberation from these reservoir species is rather slow. In the presence of PSCs, however, the conversion to photolytically-active chlorine is enhanced. The heterogeneous reactions responsible for this conversion include the following:



The gas phase product of these heterogeneous reactions, molecular chlorine, photodissociates readily to yield active chlorine which subsequently destroys ozone.

While the nature of these heterogeneous reactions is now relatively well established, the phase and composition of polar stratospheric clouds remains an uncertainty. The phase and composition are particularly important because heterogeneous reactions are sensitive to these properties.⁸ For example, recent calculations show that liquid ternary particles are 30 to 300% more reactive than nitric acid dihydrate particles for temperatures below approximately 195 K.⁹

The project reported in this thesis was proposed and designed to contribute to the understanding of the phase and composition of polar stratospheric clouds. The goal is to provide data on the physical chemistry of PSCs and, consequently, improve predictions of stratospheric ozone depletion.

1.2 POLAR STRATOSPHERIC CLOUDS (PSCs)

PSCs are a type of aerosol (a suspension of particles in a gas) that is unique to the polar stratospheric regions. This uniqueness stems from the formation temperature of the aerosol. Type II PSCs only form when stratospheric temperatures drop below approximately 189 K, and type I PSCs exist at temperatures between 195 K and 189 K.¹⁰ The phase of type II PSCs has been identified as crystalline ice,¹⁰ but the phase and composition of type I PSCs is less certain.

A limited amount of information on the phase and composition of type I PSCs has been obtained from both field and laboratory measurements. For example, field measurements indicate that they contain large amounts of nitric acid¹¹ and that they exist as both solids and liquids.^{12,13} Laboratory measurements have also suggested that various phases are possible, including nitric acid trihydrate (NAT)^{5,14} nitric acid dihydrate (NAD)^{15,16}, nitric acid pentahydrate (NAP)¹⁷, mixed hydrates¹⁸, and supercooled ternary solutions.¹⁹

At present, there are several theories on how the composition and phase of type I PSCs change as the aerosol cools.²⁰ The transition diagram shown in figure 1.1 summarizes these theories. In this figure, (aq) indicates that the aerosol contains an aqueous phase, either a pure liquid or a solid-liquid mixture. NAX and SAX indicate that the aerosol contains nitric acid and sulfuric acid hydrates, respectively, and the arrows represent possible transitions.

The transition diagram consists of three branches. The first branch involves a liquid-to-solid phase transition of a H₂SO₄-H₂O particle (step 1) followed by gas phase condensation of nitric acid and water (step 2). This branch was the first mechanism proposed to explain observations of solid PSCs.²¹ If the H₂SO₄-H₂O particle does not freeze, the liquid particle takes up gas phase nitric acid and water and forms a liquid ternary

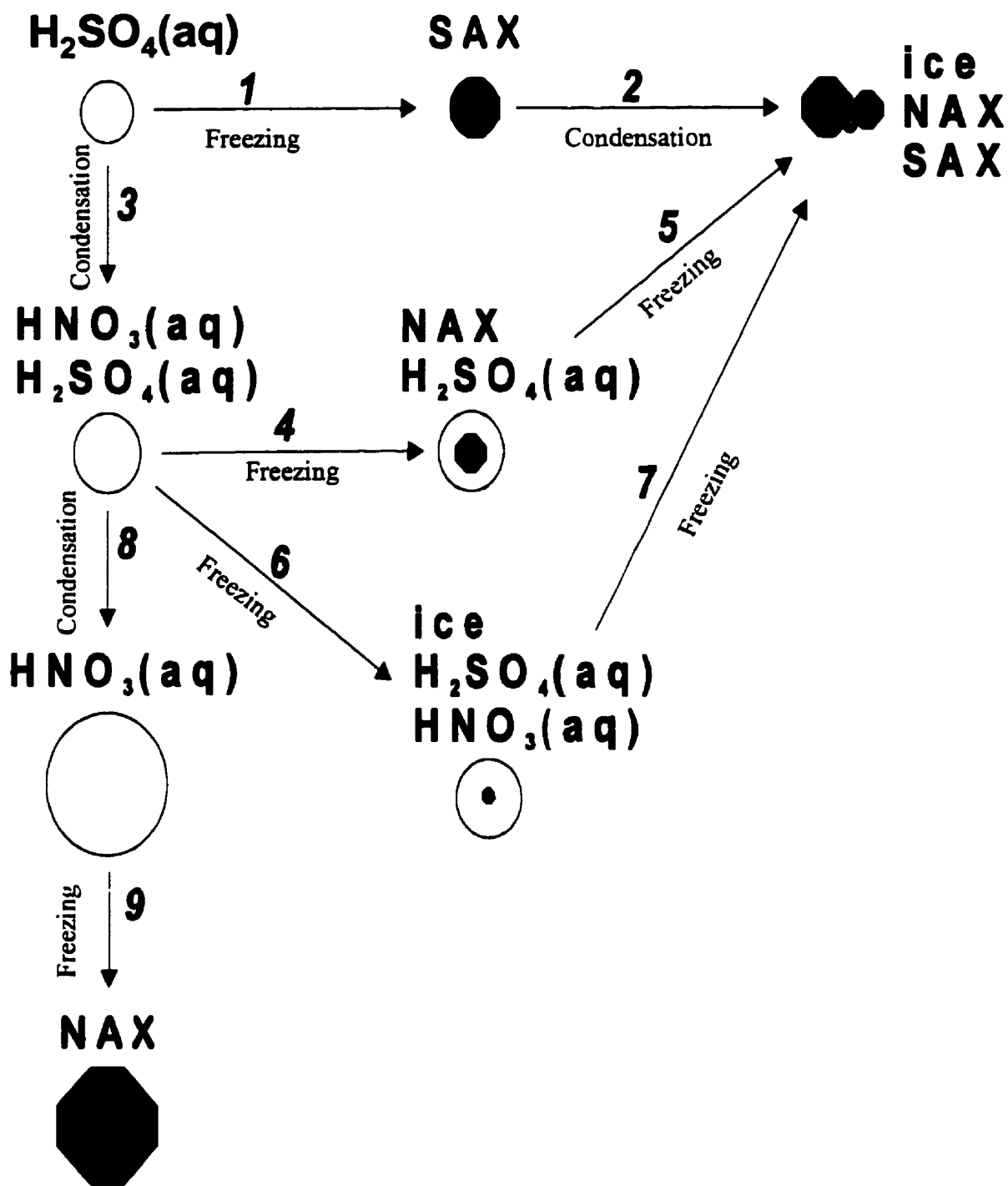


Figure 1.1 Schematic diagram representing the changes in composition and phase which could occur as the stratospheric aerosol cools.

particle (step 3).^{22,23} The second branch in the diagram involves the freezing of this ternary particle (steps 4, 5, 6 and 7). The first solid to precipitate out of the liquid ternary particle can be either nitric acid trihydrate²⁴ (step 4) or ice²⁵ (step 6). Steps 5 and 7 involve the freezing of the remainder of the particle. The ternary particle can also approach binary HNO₃-H₂O concentrations if rapid temperature fluctuations occur (step 8).^{26,27} The freezing of this liquid particle represents the final branch in the diagram (step 9).^{26,27}

The steps in the transition diagram represent thermodynamically possible pathways under polar stratospheric conditions, but thermodynamic stability is not the only prerequisite for the transitions. The kinetic feasibility of these steps must also be determined. This thesis addresses this issue. In particular, the work presented in this thesis focuses on liquid-to-solid phase transitions of sulfuric acid-water and nitric acid-water systems and probes the kinetics of these systems at polar stratospheric temperatures. This work will directly determine the feasibility of steps 1 and 9 in figure 1.1.

1.3 THESIS OVERVIEW

This thesis contains 6 chapters. Chapters 1, 2, and 3 cover the introduction, theory and methods. This includes an overall description of PSCs and their relation with ozone hole formation (chapter 1), a brief discussion on freezing rates, homogeneous nucleation, and crystal growth (chapter 2), and a description of the tools and methods used to carry out the experiments and data analysis (chapter 3). Chapters 4 and 5 present the results obtained on the nitric acid-water and sulfuric acid-water systems. This includes freezing measurements on dilute sulfuric acid aerosols (section 4.5), freezing measurements on concentrated sulfuric acid aerosols (section 4.6), nucleation measurements on 2:1 nitric acid aerosols (sections 5.2), temperature cycling and freezing of 3:1 nitric acid aerosols (sections 5.3) and freezing of non-stoichiometric nitric acid aerosols (sections 5.4). Finally, in Chapter 6, conclusions and an overall discussion related to the phase and composition of PSCs are presented.

CHAPTER TWO

KINETIC FEASIBILITY

2.1 INTRODUCTION

Under most polar stratospheric conditions, one or more crystalline phases are the thermodynamically stable states for the H₂SO₄-H₂O and HNO₃-H₂O systems. However, as mentioned in the previous chapter, if a solid is thermodynamically stable, it doesn't necessarily follow that a liquid-to-solid phase transition will occur. A substance can remain in a metastable liquid state well below the freezing temperature.²⁸ This metastability of the liquid state arises from the kinetics of liquid-to-solid phase transitions, which are controlled by the rates of homogeneous nucleation (J) and crystal growth (ω).^{29,30}

2.2 HOMOGENEOUS NUCLEATION

Continuous, transient, random structural fluctuations occur in liquids. These lead to the formation of crystalline regions, termed "embryos". The formation of an embryo leads to a decrease in free energy, ΔG_x , if the solid is thermodynamically stable and if only the thermodynamics of the bulk material is considered. One must also take into account, however, the contribution of the interface's surface energy. When this energy is included, the net change in free energy on forming the embryo, W , is a function of embryo size.³¹

$$W = \frac{4}{3}\pi r^3 \Delta G_x + 4\pi r^2 \sigma \quad (2.1)$$

In this equation, ΔG_x is the change in free energy/volume when only the thermodynamics of the bulk is considered, and σ is the surface energy of the interface. Figure 2.1 shows the variation of W with embryo size. When r is less than r^* , W increases with r . Therefore, the free energy of the system will decrease if the crystalline region remelts. If a fluctuation

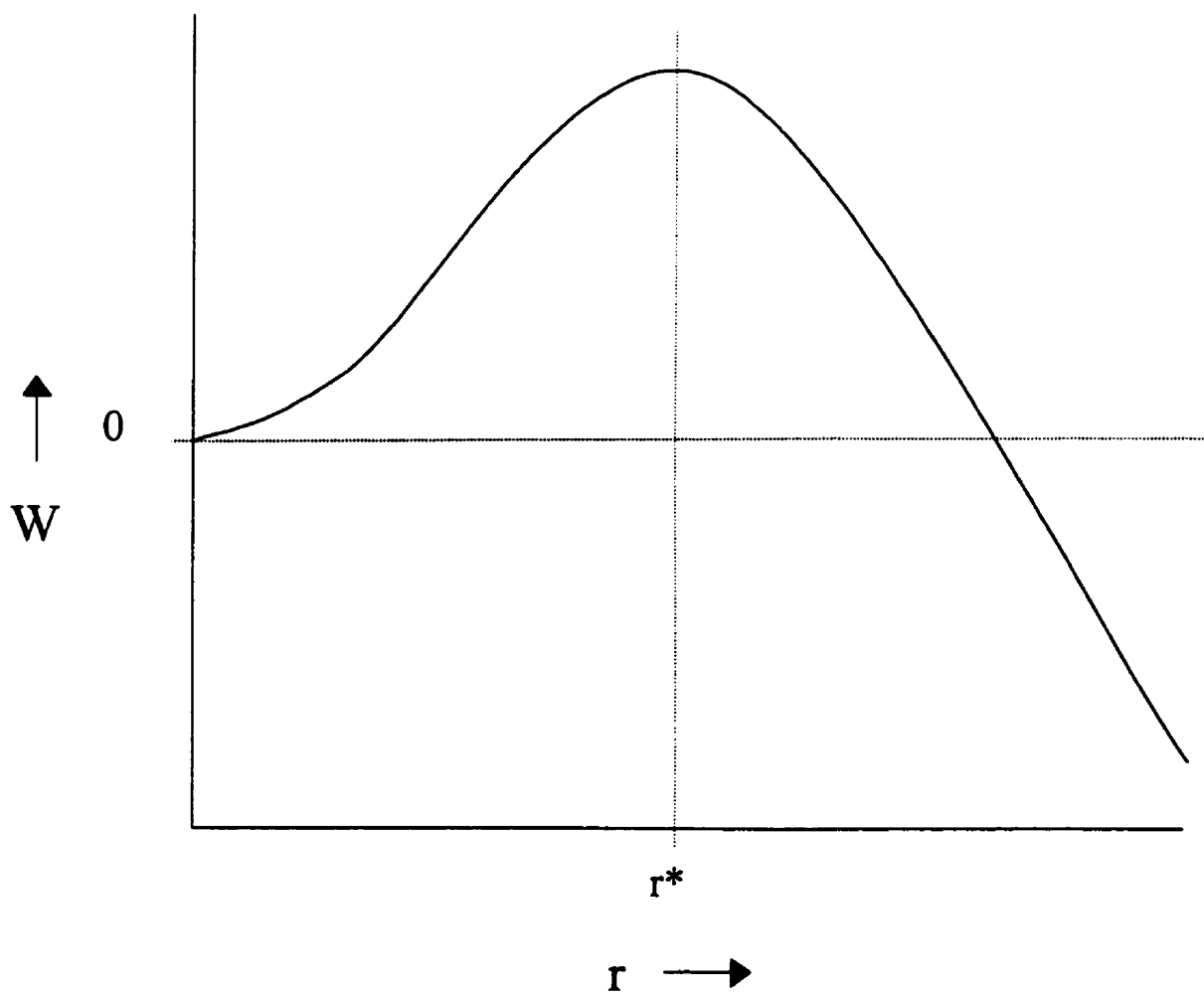


Figure 2.1 Change in Gibbs Free Energy (W) as a function of the embryo radius (r). The formation of an embryo with a radius greater than r^* results in a stable nucleus.

occurs which produces a crystalline region of radius greater than r^* , a stable nucleus will result. The process by which these stable nuclei form is referred to as homogeneous nucleation. Crystallization requires the existence of stable nuclei to act as centers from which larger crystals can grow; consequently, the rate of homogeneous nucleation can determine the kinetics of a liquid-to-solid phase transition.

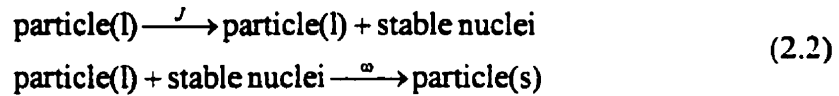
Homogeneous nucleation implies the absence of any foreign material or body that initiates crystallization. The opposite, heterogeneous nucleation, involves initiation of crystallization on some foreign surface, such as a container wall or a dust particle. The experiments described in this thesis were carried out on particles suspended in a gas. Therefore, the possibility of heterogeneous nucleation from container walls was eliminated. In addition, care was taken to ensure that all parts of the apparatus used in our freezing measurements were free from dust. Based on this information and experimental evidence discussed in section 4.5, homogeneous nucleation was assumed to be the dominant nucleation process in our work.

2.3 CRYSTAL GROWTH

Crystal growth involves the addition of molecules to the stable crystal nucleus. The rate of crystal growth depends on the rate at which atoms or molecules arrive and remain at the surface of the stable nucleus. For a stoichiometric solution (a mixture of substances that can freeze to give a crystal with the same stoichiometry as the original mixture), all the components needed for crystal growth are always present near the stable crystal nucleus. In this case, the molecules merely have to reorient to be integrated into the crystal lattice. For non-stoichiometric solutions, however, long-range diffusion processes are necessary to carry the components to the stable crystal nucleus in the required proportions. Consequently, the rate of crystal growth depends on the stoichiometry of the solution. Because viscosity limits the rate of reorientation in stoichiometric solutions and the rate of diffusion in non-stoichiometric solutions, the rate of crystal growth also depends on the viscosity of the solution.

2.4 FREEZING RATES

Both the homogeneous nucleation rate (J) and the crystal growth rate (ω) can control the freezing rate. This is clear when the two steps that control the kinetics of the freezing process are considered:



Consequently, both the nucleation rate and crystal growth rate must be larger than a certain threshold value before the crystal can grow to a detectable size. For the purposes of this discussion, this threshold value is defined as γ_{critical} . Having nucleation and crystal growth rates above γ_{critical} , however, is not the only prerequisite for freezing. A region of overlap between the two rates at a particular temperature must exist. Figure 2.2 illustrates this point. In figure 2.2b, there is no overlap between the nucleation and crystal growth rates. In this case, for temperatures where the nucleation rate is greater than γ_{critical} , the crystal growth rate is smaller than γ_{critical} , and at temperatures where the crystal growth rate is greater than γ_{critical} , the nucleation rate is less than γ_{critical} . For A system described by this diagram, the phase transition is kinetically inhibited. Figure 2.2a shows the case where there is a region of overlap between the two rate curves. Stable nuclei will form and grow in this overlap region; consequently, freezing will occur.

Freezing can also occur for systems that are described by figure 2.2b if temperature cycling is implemented. This concept is used in section 5.3 to explain the freezing kinetics of nitric acid trihydrate. Temperature cycling involves first lowering the temperature to a value where the nucleation rate is larger than γ_{critical} and then raising the temperature to a value where the crystal growth rate is larger than γ_{critical} . Stable nuclei form at the lower temperature and then grow at the higher temperature, with the result that the sample freezes.

Fig 2.2a

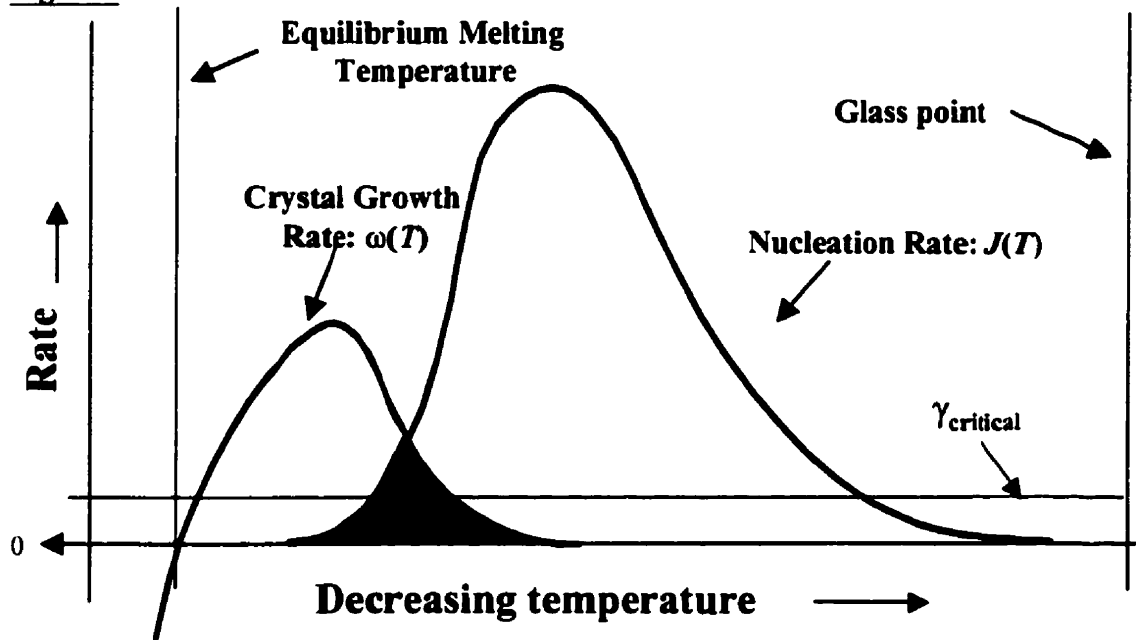


Fig 2.2b

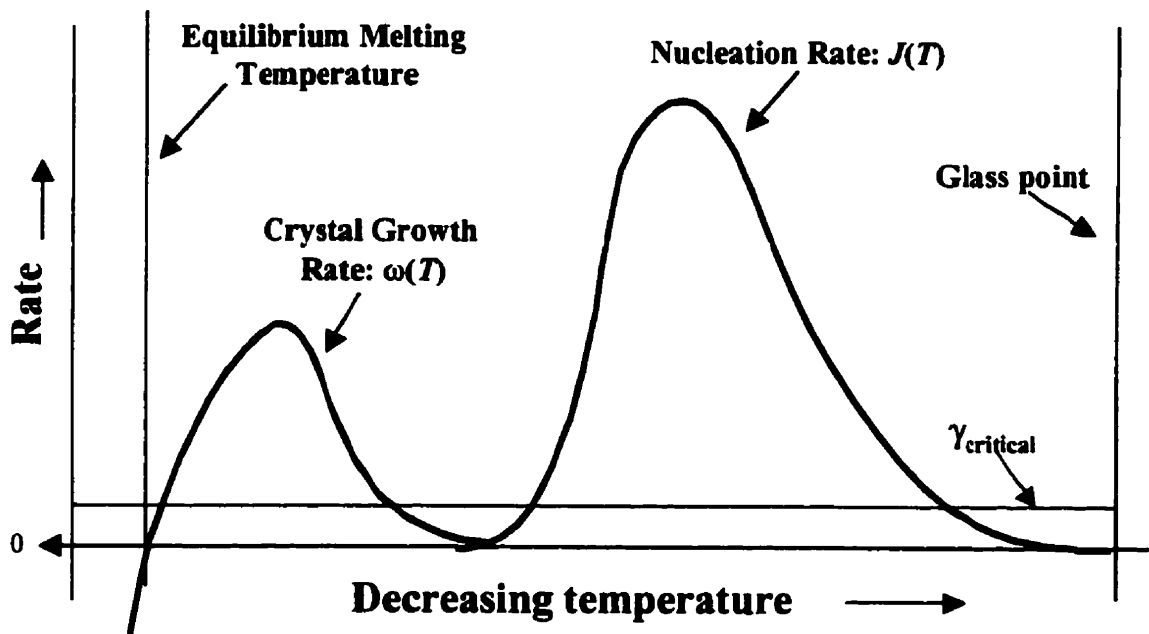


Figure 2.2 Overlap of the crystal growth rate and the nucleation rate for two chemically different systems.

CHAPTER THREE

GENERAL EXPERIMENTAL

3.1 INTRODUCTION

Previously, researchers have used thin films and bulk samples to measure phase transition kinetics of model PSCs,^{24,25,32,33,34,35} but these experimental methods have two limitations. First, the material under investigation is in contact with a surface. This introduces the possibility for heterogeneous contributions by the container walls to the process under investigation. Second, the size of the samples in these experiments is usually much larger than the aerosols found in the polar stratosphere. As a result, the possibility of size-dependent effects exists. To overcome these two limitations, we have measured the phase transition kinetics of model PSCs using suspended particles that have average sizes similar to those found in the polar stratosphere. This eliminates the possibility of heterogeneous contributions from container walls as well as size dependent effects.

Chapters 4 and 5 present results of measurements carried out on sulfuric acid and nitric acid aerosols. The experimental details for the two systems are different, but the general technique is the same. The following is a description of this general technique. Included is a description of how the freezing experiments are performed and how the physical properties of the aerosols are determined. The details of the experiments are left to the respective sections.

3.2 FREEZING EXPERIMENTS

Freezing experiments consisted of generating liquid aerosols, cooling them to a well-defined temperature, holding the aerosol at this temperature for a specific exposure time, and finally, determining the fraction of aerosol that crystallized during the exposure time.

The method of generating liquid aerosols, the first step in our freezing experiments, varied depending on the system under investigation. For sulfuric acid aerosols, the gas

phase reaction of SO₃ with H₂O was used, and for nitric acid aerosols, gas phase condensation of nitric acid and water vapour was used (see the respective sections for a detailed description).

Once the liquid aerosol is generated, it is cooled to an accurately known temperature for a specified time. This is accomplished using temperature-controlled flow cells. The aerosol particles and carrier gas flow through the temperature-controlled cells at a known rate, so the time the particles are exposed to a particular temperature is accurately known. Typically, the flow rate is 1-3 standard litres per minute (SLPM), and the residence time is 10-30 seconds. The temperature of the aerosol particles is determined from several thermocouples that are attached to the walls of the flow cells. In a separate experiment using similar flow conditions (see section 5.2 for details of this experiment), it was found that the carrier gas rapidly came into equilibrium with the wall. In addition, the time for relaxation of the temperature of the particle to that of the surrounding gas was determined using the equation³⁶

$$\tau = \frac{r^2}{\alpha} \quad (3.1)$$

where τ is the characteristic time for temperature equilibration of the particle with the surrounding atmosphere, r is the radius of the particle, and α is the thermal diffusivity of the particle medium. Using values typical of our experiments, a characteristic time of a few tens of milliseconds was calculated. Because the aerosol particles come into equilibrium with the carrier gas rapidly and the carrier gas comes into equilibrium with the walls of the flow cell rapidly, the temperature of the aerosol particles is essentially that of the walls. Thus, the temperature of the particles is accurately represented by the thermocouples attached to the walls.

The final step in our freezing measurement is the determination of the fraction of aerosol that has frozen during the exposure time. This is accomplished with IR spectroscopy. IR extinction spectra of the flowing aerosols are recorded and the fraction of the aerosols frozen are determined directly from these spectra (see section 4.5).

Experiments are carried out by first establishing a particular temperature profile in the flow cell. Then the temperature is varied over the temperature range of interest while extinction spectra are recorded at equal temperature intervals. The result is extinction spectra as a function of temperature. From these spectra and the measured residence times, the freezing kinetics are determined (see section 4.5). It is important to note here that the total residence time of a sample of particles in the flow tube is less than one minute, whereas the temperature scan takes several hours. The experiment thus consists of the continuous creation, cooling and observation of new particles, rather than the observation of the same sample of particles over a long time period. This has the advantages that the particle size distribution is invariant with time, and the residence time for each particle is known and constant.

3.3 IR SPECTROSCOPY

From the IR spectrum of an aerosol, three essential pieces of information are determined. First, the phase of the aerosol particles is determined from the shape and intensity of the IR bands. Amorphous liquids or solids exhibit broad absorption bands because the molecules occupy a variety of different sites in the sample; in contrast, crystals give rise to sharp absorption peaks due to the ordered arrangement of the molecules in the crystal lattices. Second, compositional information is extracted from the aerosol IR spectrum. Under the conditions of our experiments, the magnitude of the absorbance of a species is proportional to the concentration of that species. If two different absorbing species are present in the aerosol, the ratio of the individual absorption bands is proportional to the ratio of the concentrations of the two species. Finally, the size distribution of the aerosol particles is determined by comparing Mie scattering calculations with the aerosol extinction spectrum. More information on this topic is given in section 3.4.

The compositions of the sulfuric acid aerosols and the stoichiometric nitric acid aerosols were determined directly from the IR extinction spectra. The compositions of non-stoichiometric $\text{HNO}_3\text{-H}_2\text{O}$ aerosols, however, were determined in a slightly different way. The modified technique involved vaporizing the aerosol and determining the ratio of

nitric acid to water from the gas phase IR spectrum of the resulting vapour. More details on this technique are given in section 5.4.

3.4 AEROSOL SIZE DETERMINATION

Before kinetics can be extracted from our freezing experiments, the size of the aerosol particles under investigation must be determined. This task is further complicated because the aerosols generated in our experiments are not monodisperse. In other words, our aerosol particles have a distribution of sizes. Therefore, a mathematical function that accurately describes this distribution must be determined. A log-normal function is used in our work for this purpose because it has been employed extensively in the literature to successfully model artificially produced aerosols.^{37,38,39,40} This log-normal function is

$$f(r) = \frac{1}{r \ln \sigma_g (2\pi)^{0.5}} \exp \left[-\frac{(\ln r - \ln r_g)^2}{2 \ln^2 \sigma_g} \right] \quad (3.2)$$

where

$$\int_0^{\infty} f(r) dr = 1 \quad (3.3)$$

The two unknowns in this function are the geometric radius (r_g) and the geometric standard deviation (σ_g).

The extinction spectrum of an aerosol has contributions from absorption as well as scattering.⁴¹ This contribution of scattering and absorption to the extinction spectrum is described mathematically by Beer's law which states that the irradiance of a beam of light is exponentially attenuated from I_i to I_t in transversing a slab of aerosol particles a distance l :

$$I_t(\nu) = I_i(\nu) \exp(-NC_{ext}(\nu)l) \quad (3.4)$$

where

$$C_{ext}(\nu) = C_{abs}(\nu) + C_{sca}(\nu) \quad (3.5)$$

$C_{ext}(\nu)$, $C_{abs}(\nu)$ and $C_{sca}(\nu)$ are the frequency dependent extinction, absorption and scattering cross sections and N is the number of particles per unit volume. For particle sizes comparable to the wavelength, the $C_{sca}(\nu)$ of an aerosol varies in a complicated and rapid way with radius⁴²; consequently, the extinction spectrum of an aerosol varies in a similar manner. The calculated extinction spectra for .1, .5 and 1 micron ice particles shown in figure 3.1 demonstrate this point. This size dependence of the extinction spectrum (clearly discernible in figure 3.1) permits the determination of the particle size parameters (σ_g , r_g) from the experimental extinction spectrum of the aerosol.

The technique of extracting the true size distribution parameters (σ_g , r_g) from the experimental extinction spectrum involves calculating aerosol spectra for a range of σ_g and r_g using *Mie theory*,^{42,43,44} and comparing these calculated spectra with the experimental extinction spectrum. The σ_g and r_g that generates the best fit to the experimental spectrum are considered the true size distribution parameters.

In practice, this size-determining technique involves the following steps. First, cross section spectra for a range σ_g and r_g are calculated from a modified version of a Fortran code based on that in Bohren and Huffman.⁴² The original code, which only calculates an efficiency (Q_{ext}) for one wavelength and one radius, has been modified to calculate a cross section (C_{ext}) for multiple wavelengths and for a distribution of particle sizes. The following equation is used in the modified code to relate the cross section to the efficiency:

$$C_{ext} = Q_{ext} \times \pi r^2 \quad (3.6)$$

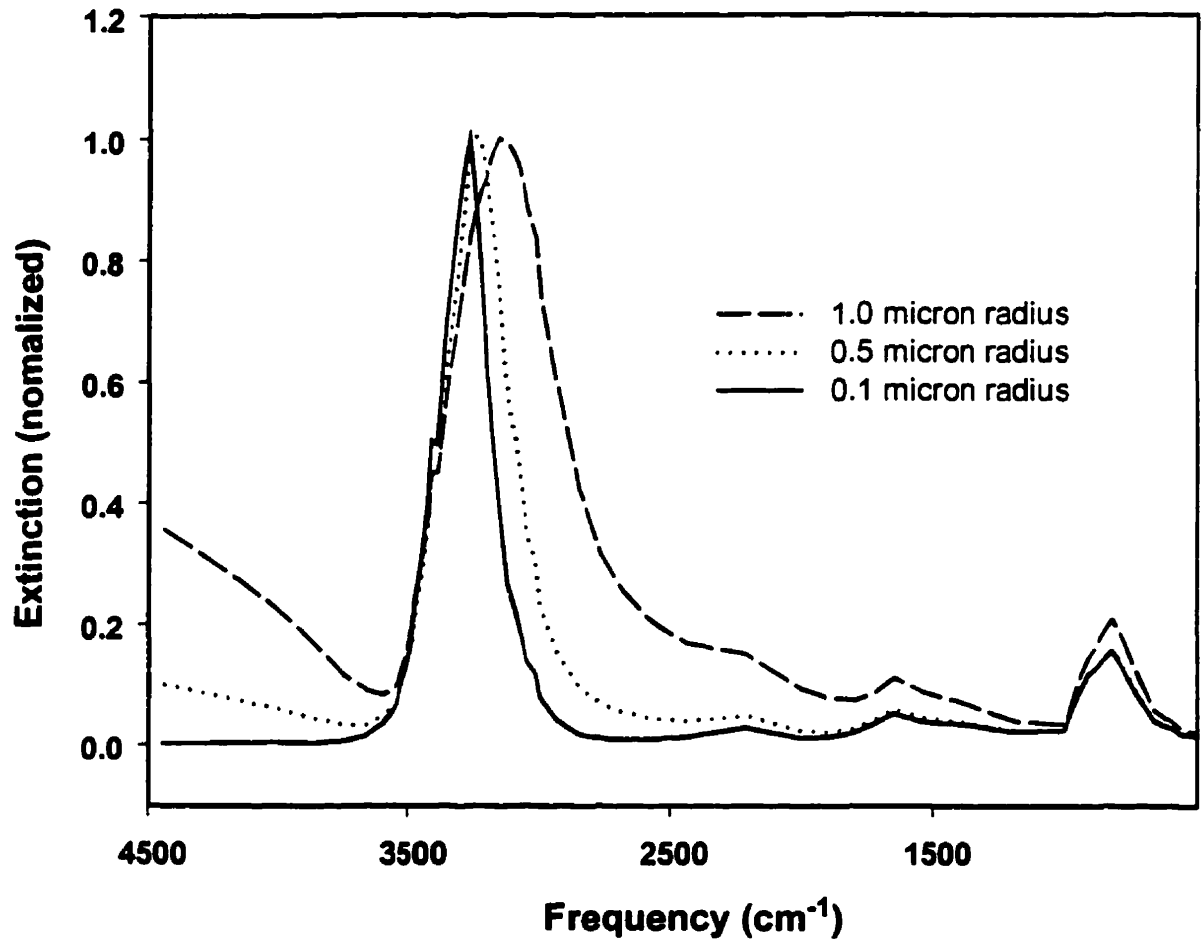


Figure 3.1 Calculated extinction spectra of 0.1, 0.5, and 1.0 micron ice particles. The maximum intensities have been normalized to 1.0.

In addition, the cross section for the distribution of sizes is calculated using the following equation:

$$C_{avg} = \sum_{r_{min}}^{r_{max}} f(r)C_{ext}(r) \quad (3.7)$$

A cross section spectrum is related to an extinction spectrum through the following equation:

$$\text{extinction spectrum} = -\ln\left(\frac{I_t(\nu)}{I_i(\nu)}\right) = C_{avg}(\nu) \times N \times l = C_{avg}(\nu) \times Z \quad (3.8)$$

where N is the particle density, l is the optical path length, and Z is the scaling factor. Consequently, the second step in the size determination involves determining a scaling factor for each calculated spectrum and, subsequently, generating scaled, calculated spectra from equation 3.8. A scaling factor for each calculated spectrum is determined by dividing the average intensity of the experimental extinction spectrum by the average intensity of the calculated spectrum. After the calculated spectra are scaled to the experimental extinction spectrum, the sum of the squares of the differences between the experimental extinction spectrum and the scaled, calculated spectra are determined. This whole process generates an array of values with columns of σ_g , r_g , N , and the sum of the squares of the differences. Each row in the array corresponds to the parameters of one calculated spectrum.

The final step involves plotting the sum of the squares of the differences between the experimental extinction spectrum and the scaled calculated spectra in the form of a contour plot with σ_g and r_g on the axes. Figure 3.2, generated from a sodium chloride aerosol produced in our laboratory, is an example of this. The contour lines in this figure represent the sum of the squares of the differences between the experimental sodium chloride spectrum and the calculated sodium chloride spectra. The true σ_g and r_g associated with the best fit to the experimental spectrum is given by the minimum in the contour plot.

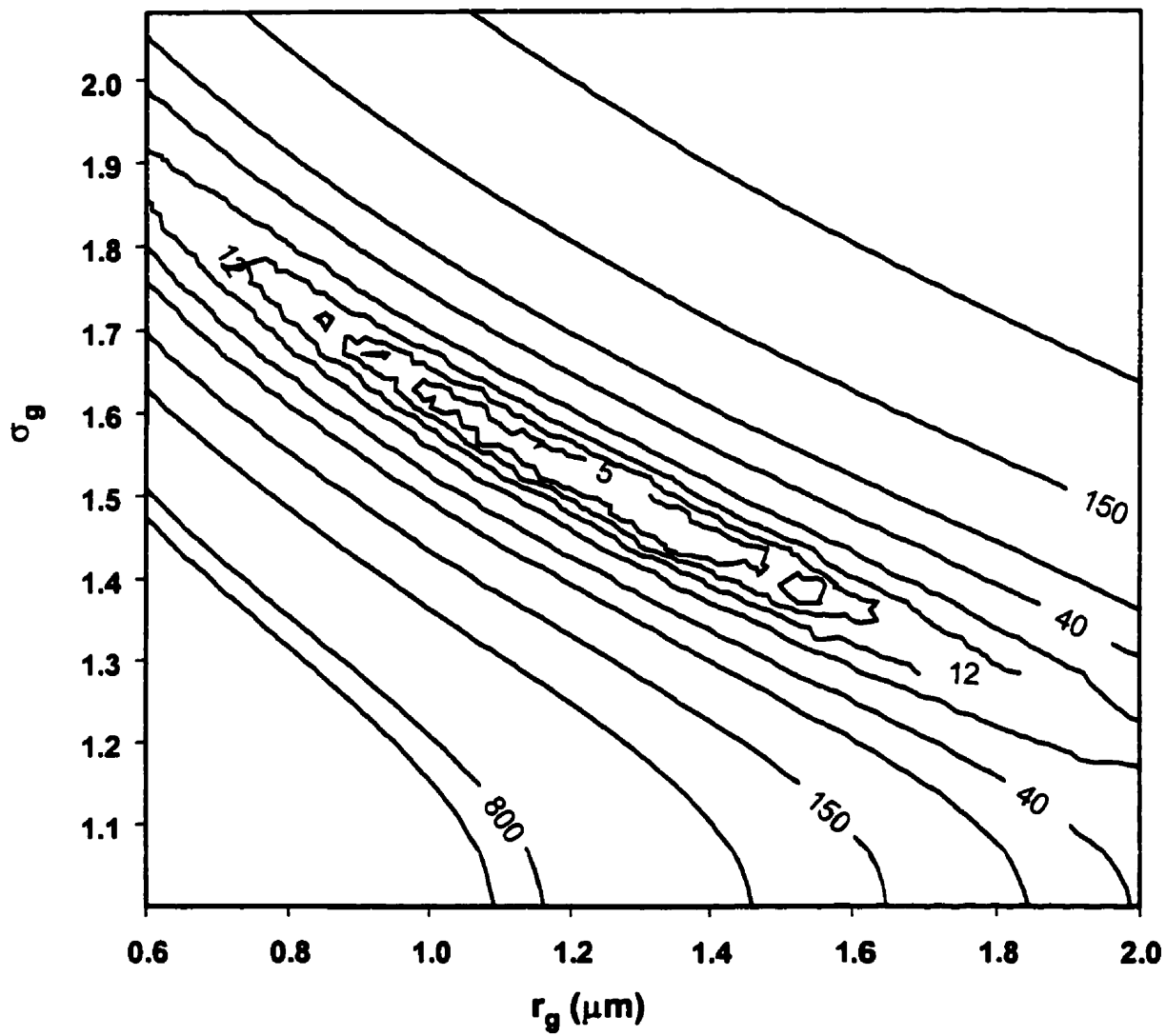


Figure 3.2 Contour plot generated for a sodium chloride aerosol. The minimum in the plot indicates $r_g=1.25$ (μm) and $\sigma_g=1.55$.

A geometric radius of 1.25 (μm) and a geometric standard deviation of 1.55 are implied from this figure. The contour plot shown in figure 3.2 was chosen to illustrate the final step in our size-determining technique because the topography of this contour map showed a single deep well. This result, however, is not always the case. The reason for this and the implications for size determination are discussed in section 4.3.

Mie theory, the theory used in our size inversion technique, is only exact for spherical particles. Thus, our inversion technique is also only exact for spherical particles. This is a serious constraint because most of the work described in later chapters involves solid aerosols, which are possibly nonspherical. Nevertheless, there is evidence that suggests that scattering from non-spherical particles differs very little from spherical particles when a range of particle sizes, shapes, and orientations is involved. For example, Pope *et al.* measured the angular dependence of scattering from solid ammonia particles that were cubic.⁴⁵ They found that the scattering could be described very well by Mie theory. Perry and co-workers also investigated the angular dependence of scattering from cubic salt particles and found similar results.⁴⁶ In addition, other researchers have found that a range of particle sizes removes effects due to nonspherical particles.⁴⁷ This experimental evidence suggests that Mie theory and our size inversion technique adequately describe the aerosols studied in this work.

CHAPTER FOUR

H₂SO₄-H₂O AEROSOLS

4.1 INTRODUCTION

In the stratosphere, sulfuric acid-water aerosols have a mean diameter of about 0.1 μm , and a number density of about 5 particles/cm³.⁴⁸ These number densities, however, can increase by as much as two orders of magnitude from volcanic activity.⁴⁹ The concentration of stratospheric sulfuric acid-water aerosols (SSAs) varies depending on the temperature.^{50,51} Under normal mid-latitude stratospheric conditions, approximately 220 K at an altitude of 20 km, these aerosol particles have a composition in the range of 70-75 weight percent sulfuric acid (wt % H₂SO₄), whereas at polar stratospheric temperatures, the aerosol can approach 45 wt % H₂SO₄.^{22,23}

The first mechanism proposed to account for the presence of nitric acid in PSCs involved the freezing of this stratospheric sulfate aerosol followed by nitric acid trihydrate condensation on the solid surface²¹ (see steps 1 and 2 in figure 1.1). The major assumption in this mechanism, freezing of sulfuric acid-water aerosols, was based on the phase diagram for the sulfuric acid-water system, which is displayed in figure 4.1.⁵² The labeling of the hydrates in this figure has been slightly modified from the original publication to include the hexahemihydrate, which Gable incorrectly identified as the hexahydrate.¹⁹ The solid curves in this figure separate the regions of stability for the various phases (ice, solid H₂SO₄, the liquid and the stable hydrates), and the curves themselves represent conditions of coexistence for two different phases. Also included in the figure, represented by the dashed curve, is the expected concentration of the stratospheric sulfate aerosol as a function of temperature. This curve was calculated using the model of Tabazadeh *et al.*⁵¹ with parameters of 5 ppmv of water vapor and 50 mbar total pressure. For polar stratospheric conditions, the dashed curve is well below the stability region of the liquid phase. This led researchers to suggest SSAs are crystalline under polar stratospheric conditions. This postulate, however, assumes that the kinetics of liquid-to-solid phase transitions of sulfuric acid solutions are fast under polar stratospheric conditions. Researchers have since

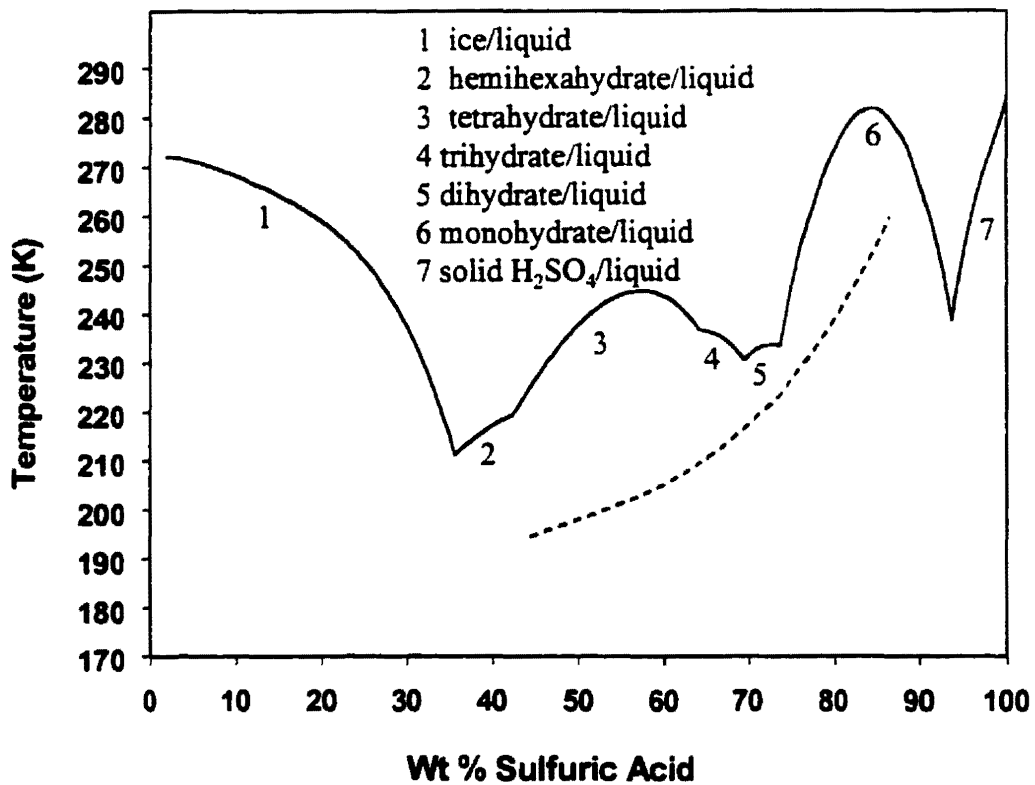


Figure 4.1 The temperature-composition phase diagram of the H₂SO₄-H₂O system. The dashed line is the expected compositions of stratospheric sulfate aerosols exposed to 5 ppmv of water vapor at 50 mbar altitude. The solid curves correspond to the liquid-solid equilibrium temperatures for the stable hydrates.

investigated the validity of this assumption by probing the freezing properties and kinetics of the sulfuric acid-water system.

Research published on this topic prior to late-1994 included theoretical calculations, but lack of thermodynamic information limited the accuracy of this work. Initial calculations by Lou and co-workers on 60 wt % H₂SO₄ solutions suggested that freezing of a large fraction of the aerosol to sulfuric acid tetrahydrate (SAT) could occur under certain polar stratospheric conditions (time scale of a few hours and temperatures from 195 to 205 K),⁵³ yet recent calculations by the same group indicated insignificant freezing under similar conditions.⁵⁴ In contrast, calculations by Jensen and Toon indicate that ice will have a significant nucleation rate ($> 2 \times 10^{11} \text{ cm}^{-3} \text{ sec}^{-1}$) in dilute sulfuric acid solutions at approximately 35 K below the ice-liquid equilibrium temperatures.⁵⁵

Prior to late 1994, several freezing experiments on bulk solutions of sulfuric acid and water were performed. In these studies, both high^{56,57} and low²⁴ freezing probabilities under polar stratospheric conditions were observed. Because the solutions were in contact with the container walls, the observed freezing could have been initiated by heterogeneous nucleation.

By late-1994, we began a series of extensive studies on the freezing properties of H₂SO₄-H₂O aerosols because it was clear that the freezing kinetics of sulfuric acid solutions had not been resolved at that time. This research, which has been partially reported in the literature⁵⁸, is described in this chapter. In addition, the current knowledge of sulfuric acid freezing kinetics and their relationship to PSCs is discussed.

4.2 EXPERIMENTAL

The liquid H₂SO₄-H₂O aerosols are generated externally to the temperature-controlled flow cell by reacting H₂O(g) with SO₃(g). H₂O(g) is generated by bubbling nitrogen through liquid water, and SO₃(g) is generated by bubbling nitrogen through fuming sulfuric acid (18-24 wt % SO₃). The two separately metered flows of N₂-SO₃ and N₂-H₂O combine at the top of a one-meter-long glass column in which the reaction forming the aerosol occurs. At the exit of the glass column, the newly formed aerosol passes through approximately one meter of Teflon tubing before entering a vertical flow tube.

The distance from the top of the glass column to the entrance of the flow tube permits adequate time for the $\text{H}_2\text{O-SO}_3$ reaction to occur.

After the sulfuric acid-water aerosols are generated, they are studied in a temperature-controlled flow tube, which consists of two cooling sections. A diagram of this vertical flow tube is shown in figure 4.2. The first section, a foam insulated stainless steel tube 4" ID by 10" long, is maintained at approximately 238 K for all of these experiments by recirculating a refrigerant through cooling coils soldered to the tube walls. The refrigerant is either methanol, cooled by a commercial refrigerator (Harris Mfg. Co. Cascade Refrigeration System Model 3-RS2-W-L), or the boil-off from liquid nitrogen. The second cooling section, shown at the bottom of the figure, is made of copper and measures 25.6 inches long by 4 inches square. This cooling section is housed in a second chamber, which is evacuated to provide thermal isolation. The temperature of this cooling section is controlled by circulating chilled nitrogen through tubing attached to the walls. Using this method of cooling, we obtained temperatures as low as 163 K in the final section. The temperature of the flow cell is monitored with two copper-constantan thermocouples attached to the wall of the top section and four attached to the wall of the bottom section. As discussed in section 3.2, the temperature of the particles is accurately determined by this method. Typically, the flow rate was 2 SLPM at a pressure of 400 torr. This gave a residence time (the time the aerosol was exposed to the final temperature) of approximately 1 minute.

The final cooling section is equipped with three sets of windows through which IR spectra can be recorded. For the measurements reported in this chapter, only the bottom set of windows was used. The mounts, which hold these windows, were designed so that the window surfaces are a few centimetres back from the main gas flow. This ensures that the windows are not exposed to the aerosol flowing in the central core of the flow tube, and hence eliminates deposits on the windows. This was verified by taking background spectra before the aerosol was introduced into the flow cell and at the end of the experiments, after the aerosol flow was turned off. In all cases the spectra were identical and no absorption features due to the aerosol were present.

During a freezing experiment, the temperature of the aerosol was lowered in two

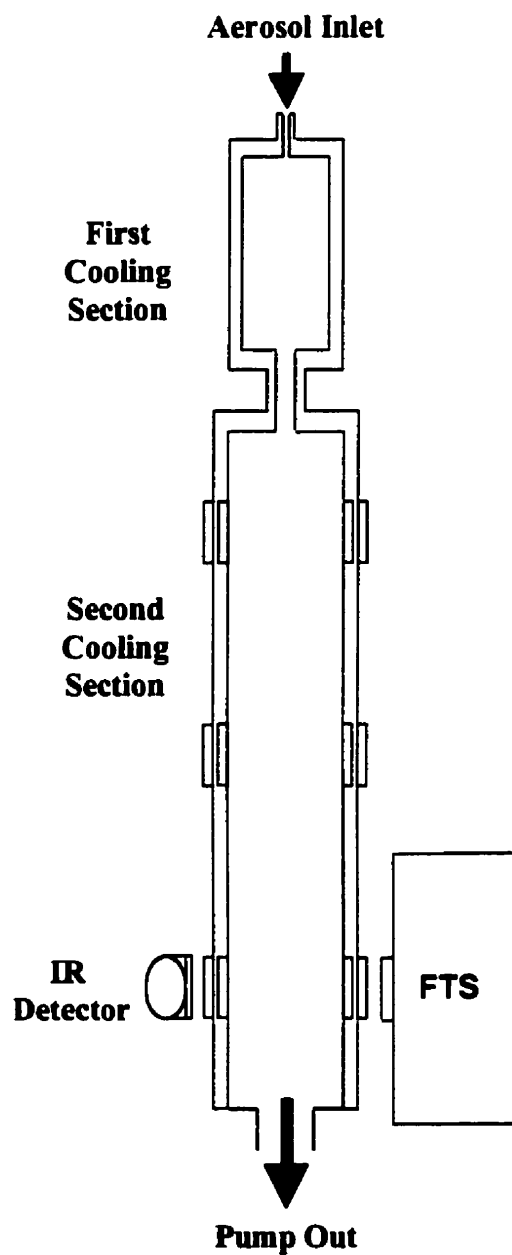


Figure 4.2 Schematic diagram of the temperature-controlled flow tube used in the $\text{H}_2\text{SO}_4\text{-H}_2\text{O}$ experiments. The aerosols enter from the top and are pumped out from the bottom.

stages. In the top section of the flow cell, the aerosol temperature was lowered to approximately 238 K, and in the bottom section, it was lowered to the final observation temperature. This method of cooling the aerosol prevents water vapor in the carrier gas from homogeneously condensing and forming ice particles. The H₂SO₄-H₂O particles produced externally to the temperature-controlled flow cell have a significant water vapor pressure. For example, a particle with a concentration of 40 wt % H₂SO₄ has a water vapor pressure of approximately 10 torr at room temperature. When this aerosol is cooled rapidly to a low temperature, the water vapor can either condense on the existing acid aerosol or homogeneously condense and form ice particles. In our experiments, however, the aerosol is first cooled to 238 K, a temperature too high for condensation of ice. (Verification of this is presented in section 4.5.) Consequently, the water vapor only condenses on the existing acid aerosol. Further cooling after the first section does not cause ice particle formation external to the sulfuric acid-water particles because the first section has significantly reduced the water vapor.

A freezing experiment consisted of first adjusting the SO₃ flow and H₂O flow until the desired aerosol concentration was produced. Once the desired composition was achieved, the temperatures of both sections were set to 238 K. Finally, IR spectra of the aerosol were recorded while the temperature of the final section was varied from 238 K to approximately 160 K. The first section was maintained at 238 K throughout this procedure.

4.3 SIZE DETERMINATION

Our size inversion technique, which is based on Mie theory, requires the optical constants of the material under investigation in order to compute aerosol extinction spectra. The optical constants used to simulate spectra of sulfuric acid-water aerosols were taken from reference 59. This work reported optical constants at 6 concentrations: 95.6 wt %, 84.5 wt %, 75 wt %, 50 wt %, 38 wt %, and 25 wt % sulfuric acid. Optical constants for concentrations between these values were generated using splines having nodes at the measured values.

Because the optical constants of sulfuric acid-water solutions are concentration dependent, the concentration of our aerosol particles must be known before our size inversion technique can be used. This apparent problem is overcome by including the concentration as a variable in the size inversion technique. In practice, this involves making an intelligent guess, based on published spectra,¹⁹ about the sulfuric acid concentration in the particles. Then spectra are calculated for a range of r_g and σ_g using the optical constants that correspond to this guessed concentration. Next, the sum of squares of the differences between the experimental spectrum and the calculated spectra are plotted in the form of a contour plot (see section 3.4 for a further discussion on this). This whole process is then repeated for a range of concentrations. The result of these calculations is several contour plots, each associated with a different concentration. The size parameters, r_g and σ_g , of our aerosol particles are determined from the contour plot with the lowest sum of the squares of the differences. The concentration used to generate this contour is assumed to be the concentration of the aerosol particles.

The solid line in figure 4.3 is an experimental spectrum of a sulfuric acid-water aerosol. 85 wt % H_2SO_4 optical constants gave the best fit to this experimental spectrum, and the corresponding contour plot is shown in figure 4.4. The topography of this contour plot is quite different from that of the contour plot shown in figure 3.2. A single minimum is evident in figure 3.2. In contrast, no well-defined minimum appears in figure 4.4. Instead a minimum contour runs diagonally from the upper left to the lower right. Along the minimum of figure 4.4, the sums of the squared differences between the experimental and calculated spectra are nearly equal. This indicates that there is a range over which an increase in r_g can be nearly compensated by a decrease in σ_g . For this reason, unique size distribution parameters cannot be determined from this contour plot.

This result led to the following question: does a unique solution only occur for big particles, such as the NaCl particles described in section 3.4? To address this question, a series of calculations were performed. First, three spectra were calculated with the following parameters: $\sigma_g=1.4$ and $r_g=1.0, 0.5,$ and $0.25 \mu m$. Our size inversion technique was then used to determine the size parameters of these spectra. This consisted of importing these calculated spectra into our size inversion code and treating them as

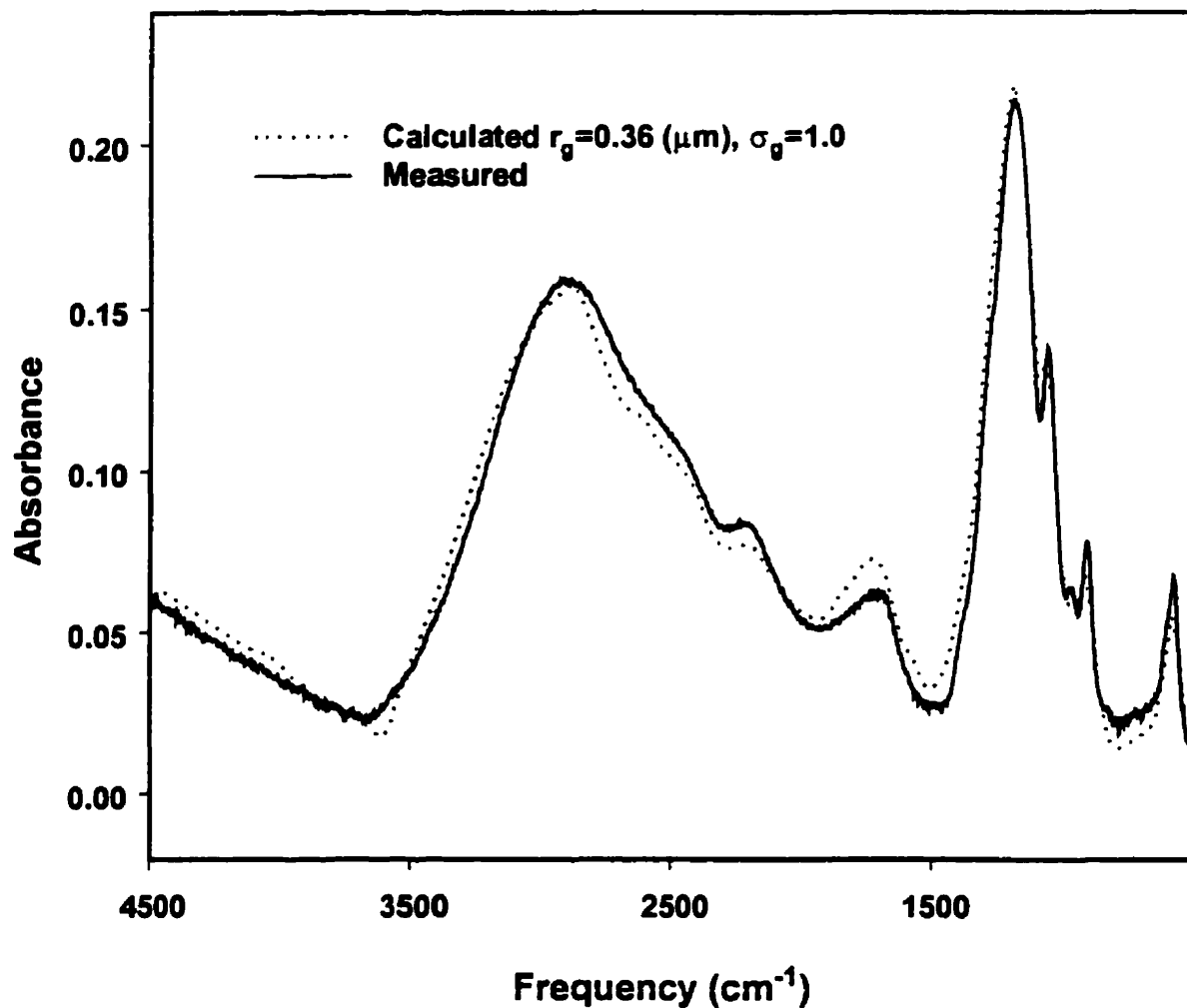


Figure 4.3 Spectra of 85 wt % H₂SO₄ particles. The solid line is an experimental spectrum of an aerosol at 250 K. The dashed line is a calculated spectrum that was generated with the parameters $r_g=0.36$ (μm) and $\sigma_g=1.0$.

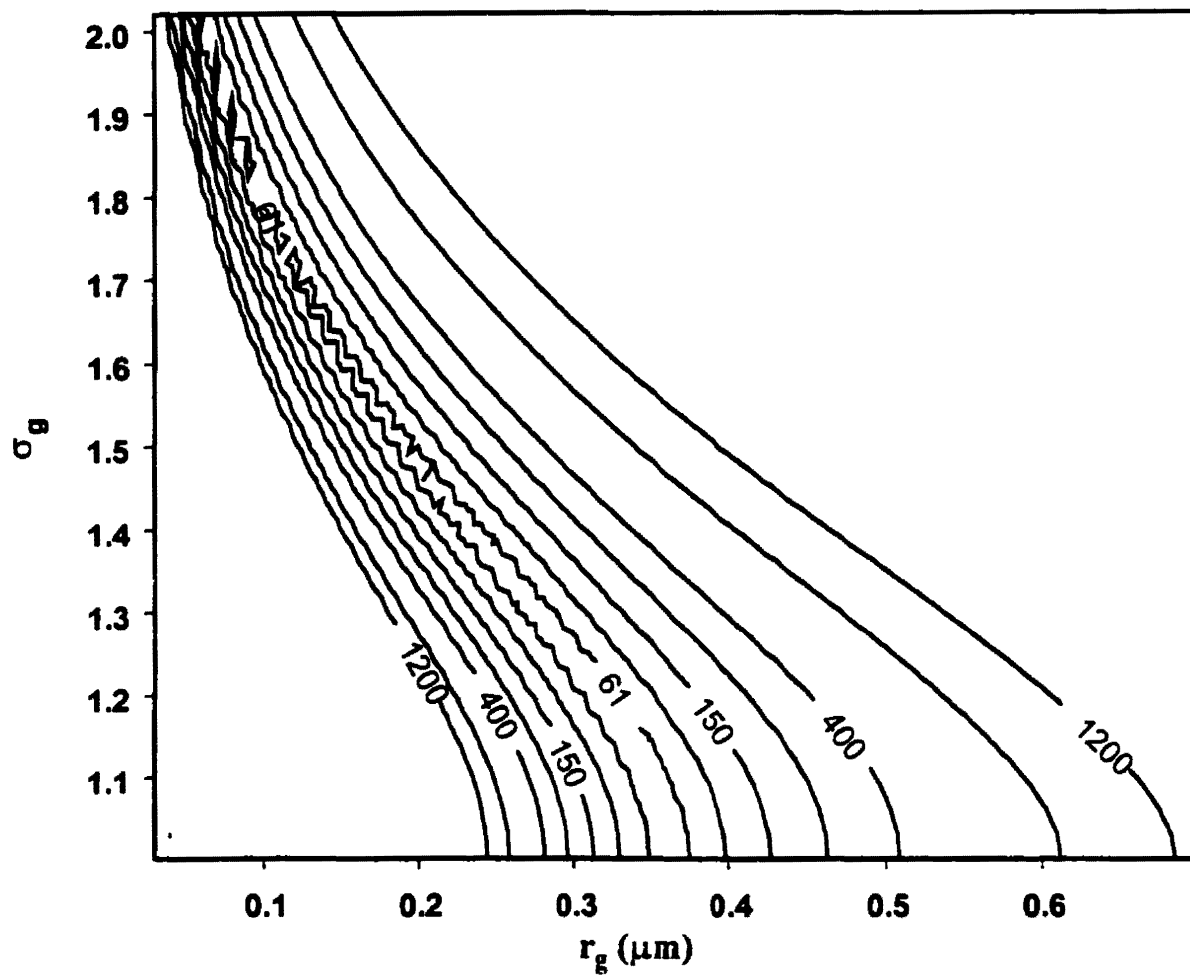


Figure 4.4 Contour plot generated for a 85 wt % H_2SO_4 aerosol.

experimental spectra with unknown size parameters. The resulting contour plots are shown in figure 4.5, 4.6 and 4.7. Figure 4.5, the contour generated from the spectrum with a geometric radius of $0.25 \mu\text{m}$, is very similar to the contour displayed in figure 4.4. The minimum contour runs diagonally from the upper left to the lower right, and along the minimum contour, the sum of the squares of the differences are nearly equal. The topography of the contours in both figure 4.6 and 4.7, however, show a single deep minimum. The size parameters inferred from these deep minima are $\sigma_g=1.4$ and $r_g=0.5 \mu\text{m}$ for figure 4.6 and $\sigma_g=1.4$ and $r_g=1.0 \mu\text{m}$ for figure 4.7. These values are identical to the parameters used to calculate the spectra initially. This suggests that our size inversion technique will give correct results for large size parameters if accurate optical constants are used in the Mie calculations. Conversely, figure 4.5 suggests that our size inversion technique will not give a unique solution for small size parameters.

From figure 4.4, we cannot determine unique size distribution parameters for our $\text{H}_2\text{SO}_4\text{-H}_2\text{O}$ aerosols. Despite this caveat, it is clear that the lowest contour in this figure is wider at the lower right end of the minimum and becomes progressively narrower until it begins to disappear around $r_g=0.13 \mu\text{m}$ and $\sigma_g=1.7$. Thus, limits of the size distribution parameters can be inferred from the shape of the contour plot. The best fit to the experimental spectrum occurs for parameters corresponding to this lowest contour with upper limits of $r_g=0.13 \mu\text{m}$ and $\sigma_g=1.7$ and lower limits of $r_g=0.36 \mu\text{m}$ and $\sigma_g=1.0$. ($\sigma_g=1.0$ is the lower limit because it corresponds to a monodisperse aerosol.) The dashed line in figure 4.3 is a spectrum calculated with parameters $r_g=0.36 \mu\text{m}$ and $\sigma_g=1.0$. Clearly, the calculated spectrum reproduces the experimental spectrum very well.

The results shown in figure 4.4 are typical of the results we obtained from fitting spectra of aerosols with concentrations greater than approximately 75 wt % H_2SO_4 . In all cases, the limits on the size parameters were very similar to the values determined from figure 4.4 (upper limits of $r_g=0.13 \mu\text{m}$ and $\sigma_g=1.7$ and lower limits of $r_g=0.36 \mu\text{m}$ and $\sigma_g=1.0$). However, when we investigated aerosol particles with concentrations less than approximately 75 wt %, a serious problem became evident: the optical constants reported in reference 59 are incapable of reproducing low-temperature spectra of dilute aerosols (<75 wt %). These optical constants were recorded at room temperature, whereas the

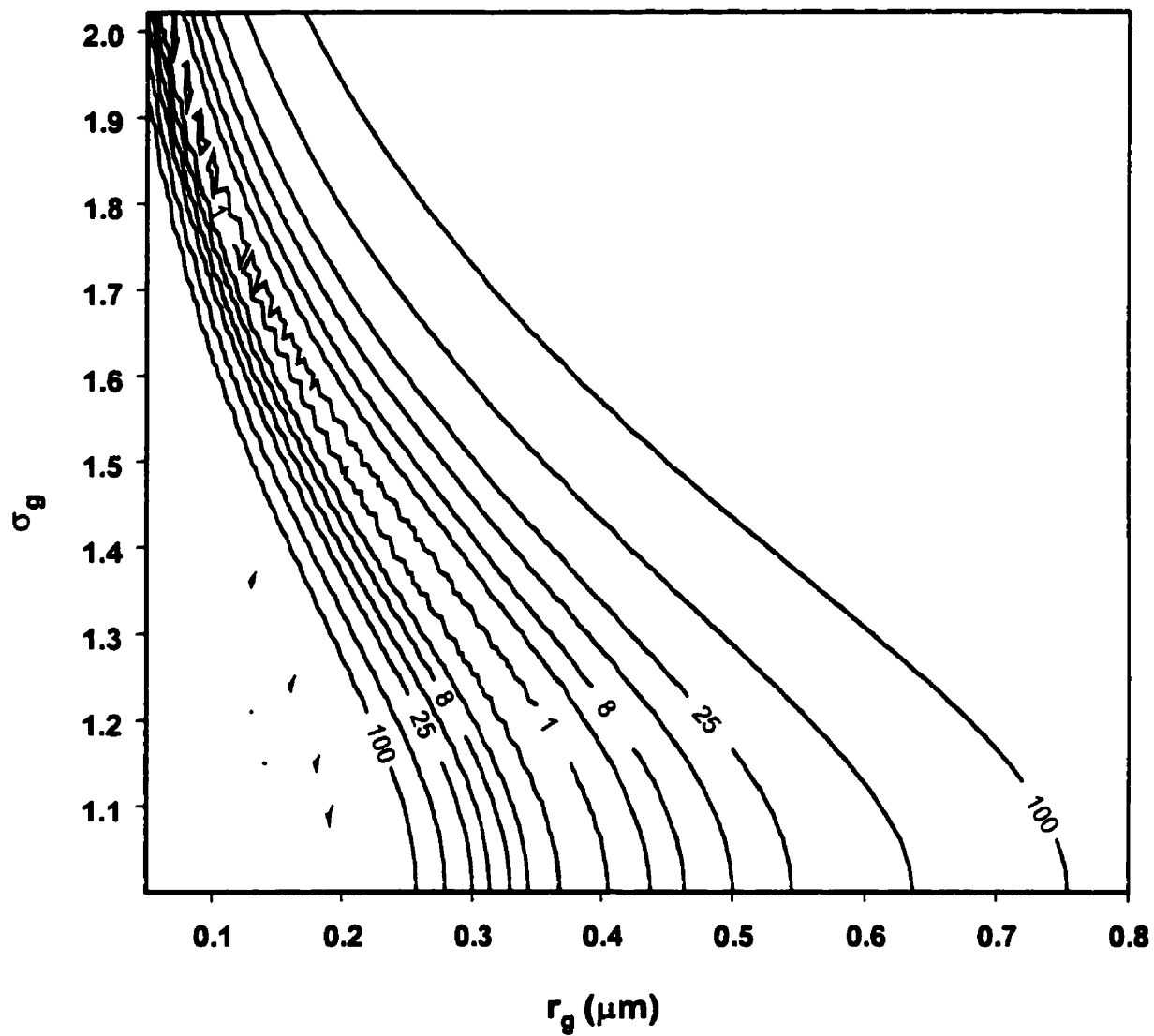


Figure 4.5 Contour plot generated for a calculated spectrum with parameters $r_g=0.25$ (μm) and $\sigma_g=1.4$.

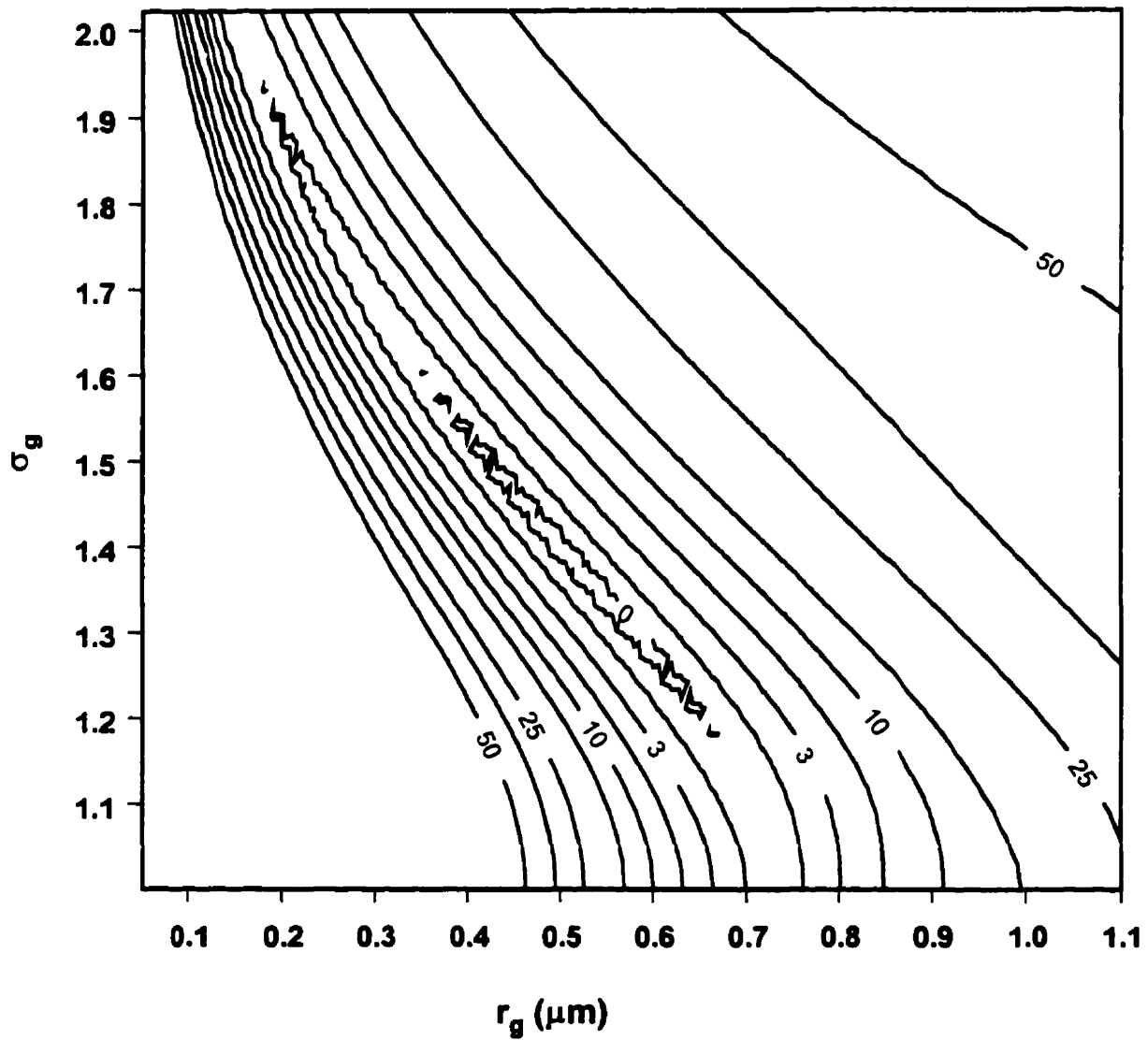


Figure 4.6 Contour plot generated for a calculated spectrum with parameters $r_g=0.5$ (μm) and $\sigma_g=1.4$.

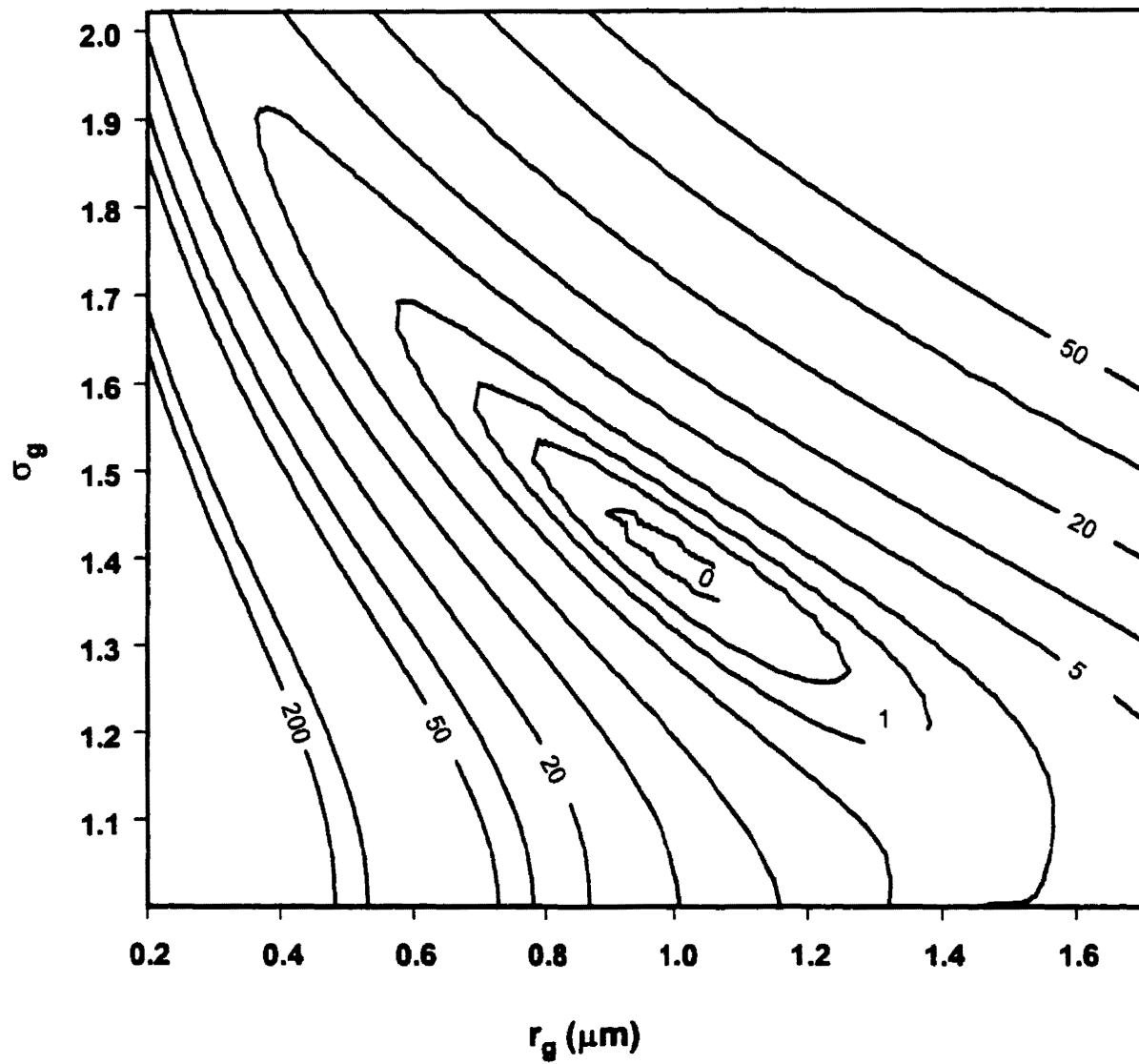


Figure 4.7 Contour plot generated for a calculated spectrum with parameters $r_g=1.0$ (μm) and $\sigma_g=1.4$.

aerosol spectra were recorded at low temperatures. This is not a significant problem for concentrated (> 75 wt % H₂SO₄) aerosols, because the spectrum of concentrated solutions is relatively insensitive to temperature.¹⁹ In contrast to this, the spectra of solutions with concentrations less than 75 wt % H₂SO₄ are sensitive to temperature. (This will be discussed in greater detail in the following sections.) As a result of this temperature dependence, we are unable to determine log-normal size parameters for concentrations less than 75 wt %. We make the approximation that aerosols with concentrations less than 75 wt % H₂SO₄ generated in our apparatus have similar size parameters to the concentrated aerosols generated in our apparatus (upper limits of $r_g=0.13 \mu\text{m}$ and $\sigma_g = 1.7$ and lower limits of $r_g=0.36 \mu\text{m}$ and $\sigma_g=1.0$). These limits are used exclusively in the remainder of this chapter to parameterize our H₂SO₄-H₂O aerosols.

4.4 CONCENTRATION DETERMINATION

The acid composition was determined directly from the aerosol extinction spectra. This spectroscopically based method uses the relative areas of the bands associated with water and sulfate ions, near 3300 and 1000 cm⁻¹, respectively, as a measure of the acid concentrations. The location of these bands in the room-temperature spectrum of a 50 wt % H₂SO₄ aerosol is indicated in figure 4.8. The L1 lines displayed in the figure encompass the OH stretching band of water and the L2 lines encompass the sulfate band. A ratio of these two bands equals the ratio of H₂SO₄ and H₂O in the aerosol multiplied by a calibration factor. If this calibration factor is known, the acid concentration of the aerosol can be determined directly from the extinction spectrum.

One method of obtaining this calibration factor involves recording IR spectra of thin films of known acid concentrations, and then relating the area of the sulfate and OH bands in the spectra to the known concentrations. Anthony *et al.* employed this method and found the ratio of the area of the OH band to the area of the sulfate band was proportional to the weight percent of sulfuric acid through the following equation.⁶⁰

$$\text{Weight percent acid} = -0.133 + 1.076 \times \left[\frac{\text{OH area}}{\text{sulfate area}} \right]^{-0.414} \quad (4.1)$$

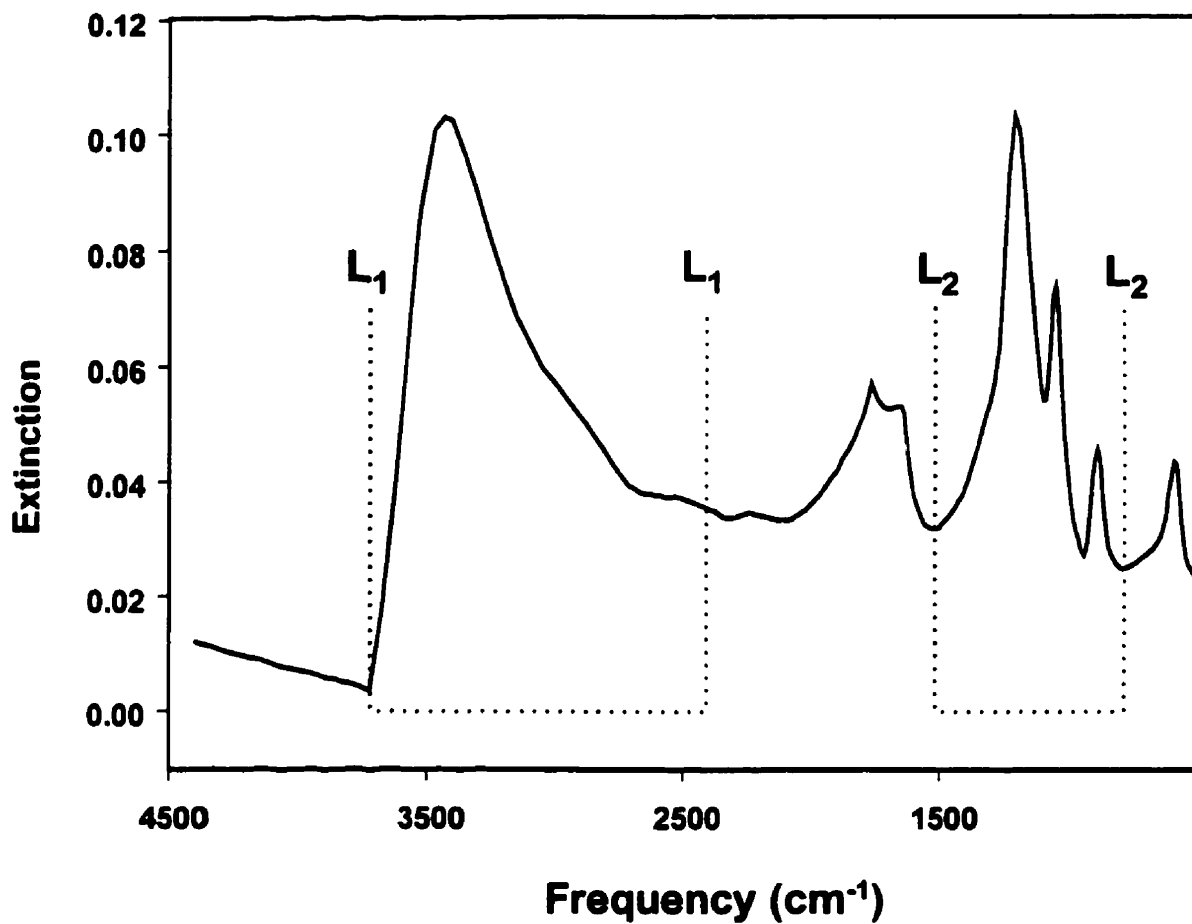


Figure 4.8 Room-temperature spectrum of a 50 wt % H₂SO₄ aerosol. The L1 lines indicate the position of the OH band, and the L2 lines indicate the position of the sulfate band.

The limits used to define these bands were 3650 and 2409 cm^{-1} for the OH band and 1470 and 820 cm^{-1} for the sulfate band.

The major limitation associated with this method is that the IR bands and intensities are temperature dependent. Therefore, the use of calibration data based on room-temperature spectra of thin-films introduces some uncertainties when applied to low-temperature aerosol spectra. The temperature dependence of the spectra stems from the fact that the dissociation of H_2SO_4 varies with temperature. Figure 4.9 illustrates this point. Shown are spectra from 1450 to 750 cm^{-1} of 36 wt % H_2SO_4 particles at 237, 225 and 196 K. Also included in this figure are the frequencies of the HSO_4^- ion (1167, 1054, and 898 cm^{-1}) and the frequencies of the SO_4^{2-} ion (1125, 980 cm^{-1}).⁶¹ Clearly, HSO_4^- increases with increasing temperature, while SO_4^{2-} increases with decreasing temperature. This change with temperature has two consequences. First, the limits over which the band intensities are determined must be chosen carefully, to include all of the important absorption bands, and second, the assumption must be made that the IR spectral absorption coefficients of the different species (HSO_4^- and SO_4^{2-}) are approximately the same. The determination of the correct integration limits may be done by careful inspection of the spectra, but the latter assumption cannot be quantified, so the approximation is made that the two sulfate ions have equal absorption strengths. This approach, nevertheless, appears to give good results: the data reported in reference 60 show that the concentrations derived from thin-film spectra taken at room temperature and at low temperatures differ by only 3%.

Another problem associated with using the area of the bands in thin-film spectra to determine concentrations of aerosols stems from the fact that scattering associated with aerosols is not present in thin films. Scattering can shift and broaden absorption bands as well as modify band intensities. Consequently, thin-film calibration curves may be inappropriate for determining aerosol composition. This issue will be addressed in the following paragraphs.

The second method that can be used to obtain calibration factors involves calculating extinction spectra for various known concentrations of the acid, and relating the concentration to the ratio of the hydroxyl and sulfate bands in these calculated spectra.

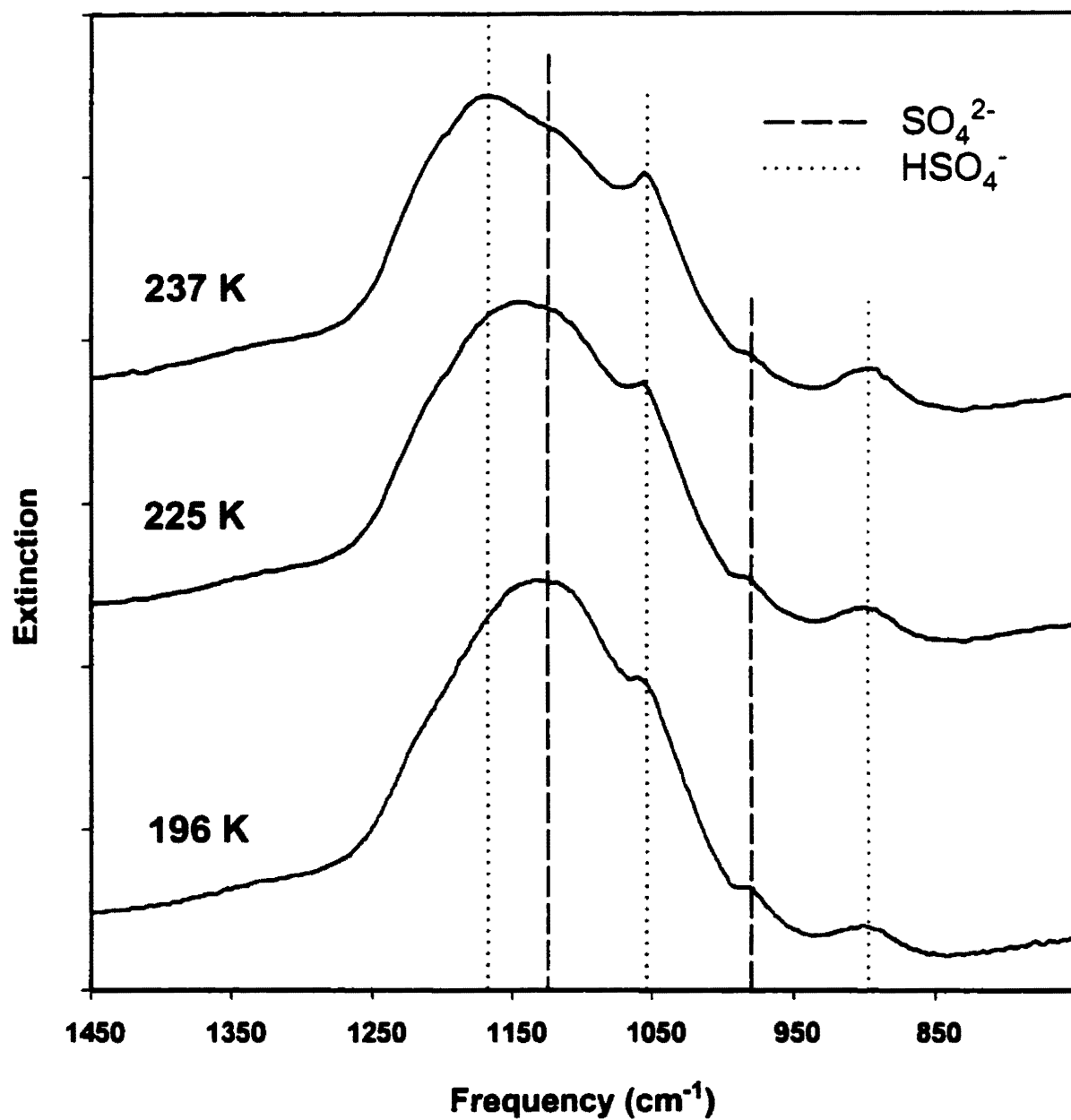


Figure 4.9 Infrared spectra of a 36 wt % H₂SO₄ aerosol at 237, 225, and 196 K. The dashed lines indicate the positions of the SO₄²⁻ bands (1125, 980 cm⁻¹), and the dotted line indicates the positions of the HSO₄⁻ bands (1167, 1057, and 898 cm⁻¹). The spectra have been offset in the vertical direction for clarity.

This method has the advantage that it takes into account the effects of scattering, but because only room temperature indices of refraction are available for H₂SO₄-H₂O system, this method still has uncertainty from the temperature dependence of the spectra (see above).

Extinction spectra for room-temperature aerosols having various concentrations were calculated, and from these spectra, calibration curves that relate the concentration of the aerosol to the ratio of the areas of the hydroxyl and sulfate bands were generated. To measure the areas of the absorption bands, it was necessary to establish limits to begin and end the integration. Shown in figure 4.10 are the limits suggested in reference 60, as well as a calculated aerosol spectrum ($r_g=0.36 \mu\text{m}$ and $\sigma_g=1.0$). These integration limits, represented by the vertical lines, do a reasonable job of including all of the appropriate bands, but close inspection reveals that the limit at 3650 cm^{-1} does not include the entire hydroxyl band. To include all of the bands and follow the small shifts introduced by both scattering and temperature dependence, we have used only one fixed limit (2409 cm^{-1}) and set the others at the ends of the respective bands. In practice, the end of the band is defined to be the location of the minimum in the spectrum that immediately follows the last absorption feature.

The error associated with estimating concentrations from a thin film calibration curve can be determined with this new calibration technique. First, the calibration curve of a thin film is approximated with the calibration curve of an aerosol having a small particle size ($r_g=0.03 \mu\text{m}$ and $\sigma_g=1.0$). Aerosols in this size range do not scatter light significantly; hence, the calculated aerosol extinction spectrum is similar to the spectrum of a thin film. Next, this calibration curve is compared to the calibration curve generated for an aerosol having a particle size of that under investigation. Typical size parameters of our H₂SO₄-H₂O aerosols are $r_g=0.36 \mu\text{m}$ and $\sigma_g=1.0$. Shown in figure 4.11 is the calibration curve that was generated with these parameters, and the calibration curve that was generated for an aerosol with $r_g=0.03 \mu\text{m}$. Clearly, these two calibration curves are different. In fact, the concentration of $r_g=0.36 \mu\text{m}$ aerosol is underestimated by about 4 % using the calibration curve that approximates a thin-film calibration curve. Note that the parameters $r_g=0.36 \mu\text{m}$ and $\sigma_g=1.0$ are only one of the limits which describe the size of our aerosols (see section

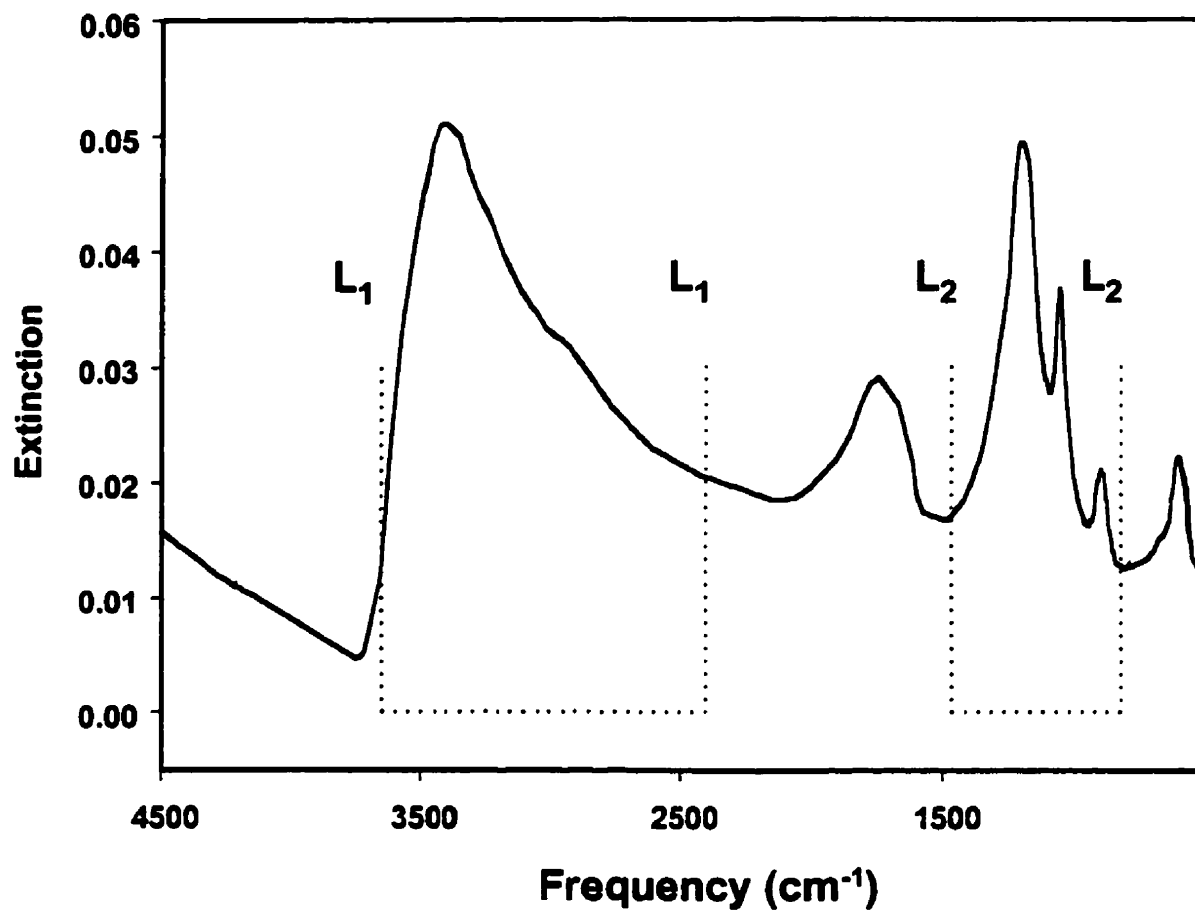


Figure 4.10 Room-temperature spectrum of a 50 wt % H_2SO_4 aerosol. The size parameters of this aerosol are $r_g=0.36$ (μm) and $\sigma_g=1.0$. The L1 and L2 lines indicate the integration limits used in reference 60.

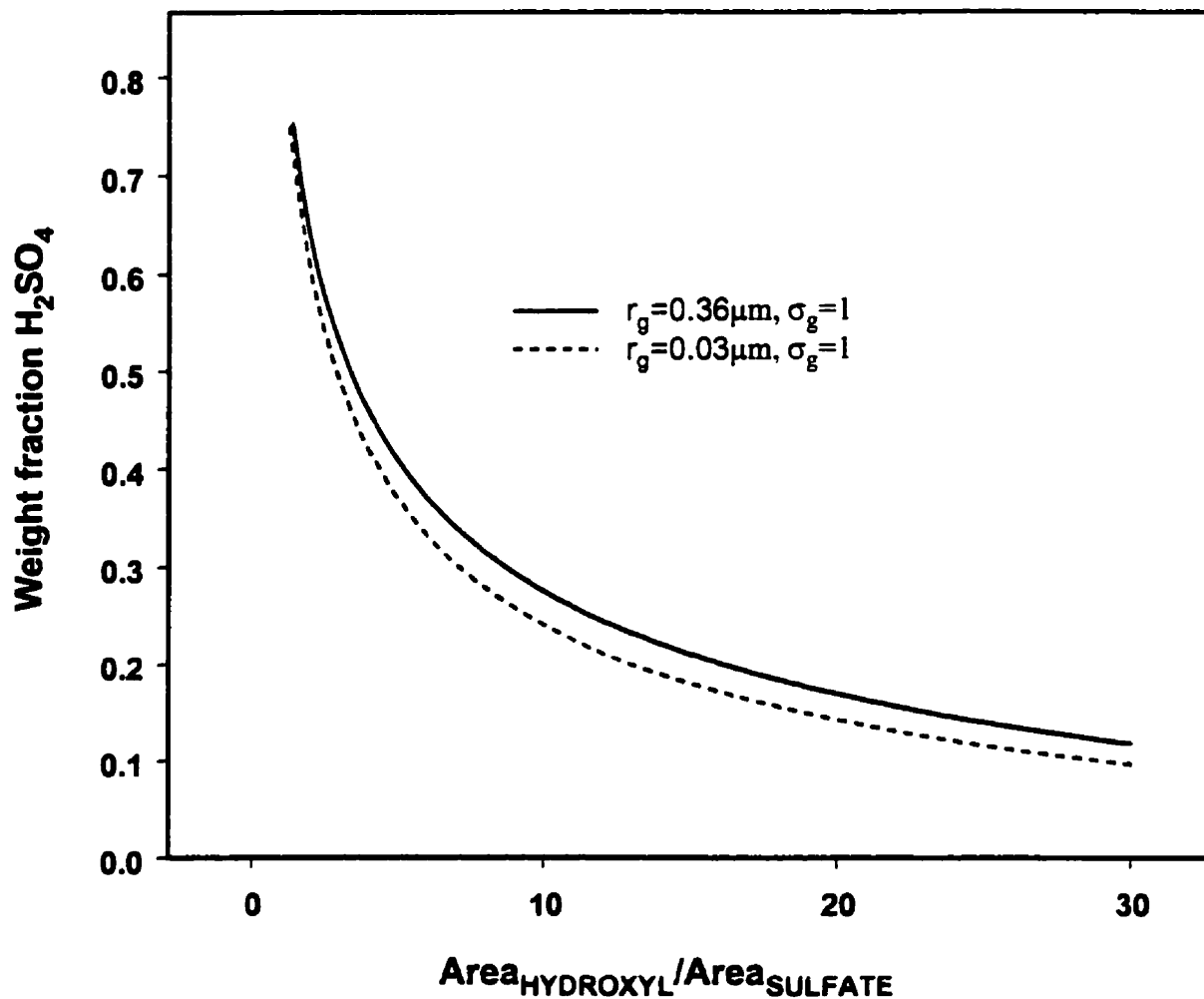


Figure 4.11 Calibration curves used to determine the H₂SO₄ particle concentration from the ratio of the hydroxyl and sulfate bands. The solid curve was calculated with the parameters $r_g=0.36 \mu\text{m}$ and $\sigma_g=1.0$, and the dashed curve was calculated with the parameters $r_g=0.03 \mu\text{m}$ and $\sigma_g=1.0$. These curves are based on spectra calculated from room-temperature optical constants.

4.3). Nevertheless, calibration curves calculated for any combination of r_g and σ_g that lie along the bottom contour of figure 4.4 are identical to the calibration curve calculated with the parameters $r_g=0.36 \mu\text{m}$ and $\sigma_g=1.0$.

The calibration curves shown in figure 4.11 are parameterised in the same form as that of reference 60: $[\text{H}_2\text{SO}_4]=a+bx^c$, where x is the ratio of hydroxyl band to the sulfate band and $[\text{H}_2\text{SO}_4]$ is the acid weight fraction. The values of the parameters are, for $r_g=0.03 \mu\text{m}$, $a=-0.173$, $b=1.01$, and $c=-0.388$ and, for $r_g=0.36 \mu\text{m}$, $a=-0.268$, $b=1.124$ and $c=-0.3164$. The parameters corresponding to $r_g=0.36 \mu\text{m}$ were used to determine the concentration of all the low-temperature aerosols composed of sulfuric acid and water. The error associated with this calibration technique due to the temperature dependence of the spectra is estimated to be $\pm 3 \text{ wt } \%$ (the temperature dependent error reported in reference 60).

4.5 DILUTE H_2SO_4 - H_2O AEROSOLS

4.5.1 Results

During initial experiments on the sulfuric acid-water system, we observed that ice precipitates out of sulfuric acid-water aerosol particles with compositions less than 35 wt % H_2SO_4 (verification of this is given below). Accordingly, we performed a series of measurements to determine the precise temperature at which ice first appears. The concentrations investigated in these experiments (<35 wt % H_2SO_4) are less than the concentrations predicted by current stratospheric models (75 to 45 wt % H_2SO_4); nevertheless, these measurements are of atmospheric interest because cirrus clouds are believed to form by the precipitation of ice in aerosols with a sulfuric acid concentration less than 35 wt %.^{62,63} Furthermore, in the future, dilute H_2SO_4 aerosols may be important in the stratosphere if conditions such as temperature or trace gas concentrations change.

Freezing experiments on dilute (<35 wt %) sulfuric acid-water aerosols consisted of recording spectra of the aerosols over a wide temperature range. Shown in figure 4.12 are results from one of these experiments. Displayed are spectra of 30 wt % H_2SO_4 particles at temperatures ranging from 220 K to 170 K. The lowest three spectra in this figure are very similar. In fact, as the aerosol is cooled from room temperature to 206 K, all the features in

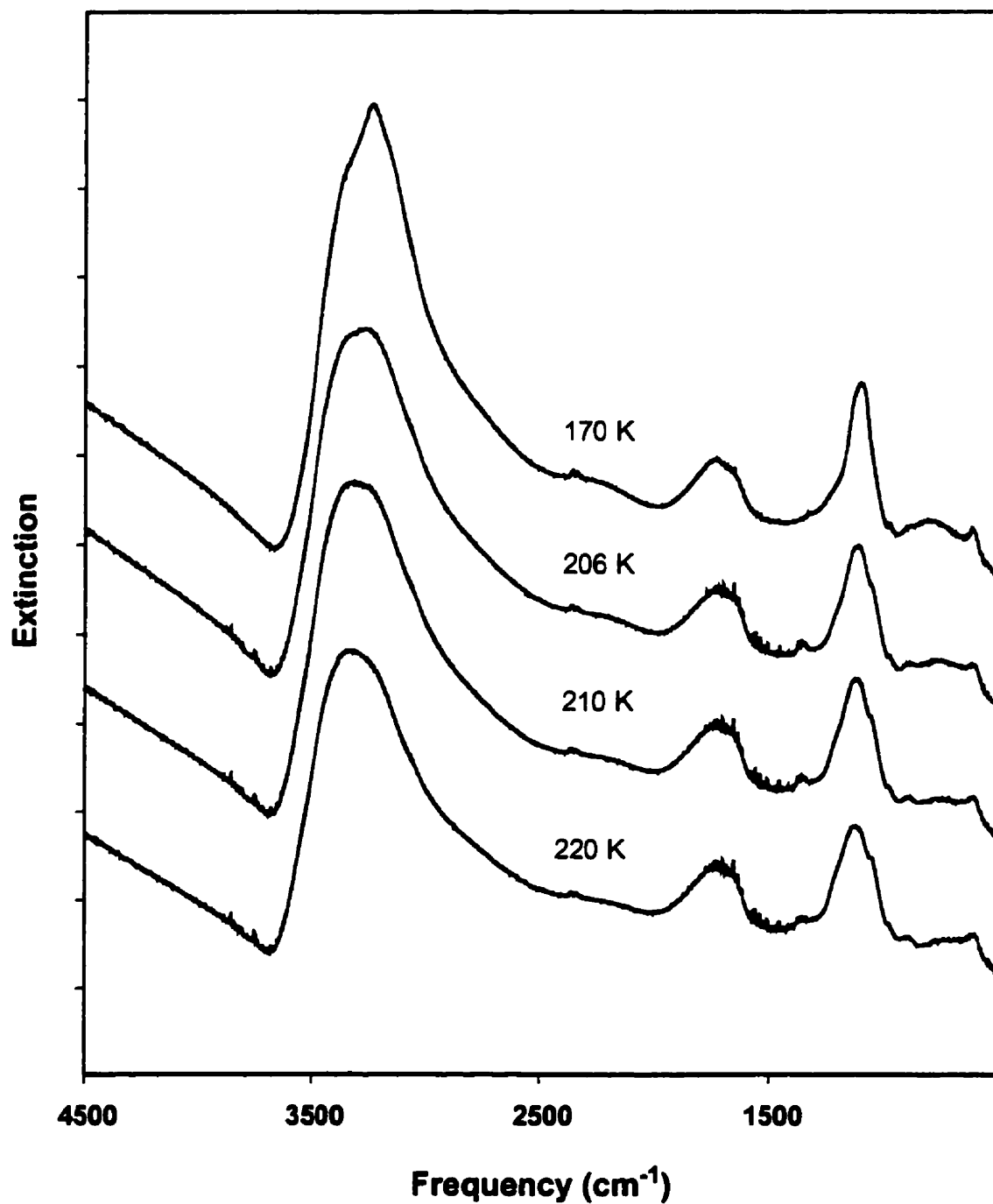


Figure 4.12 Temperature dependence of the observed extinction spectrum of a 30 wt % H₂SO₄ aerosol. The spectra have been offset in the vertical direction for clarity.

the IR spectrum show only very small changes, which are consistent with cooling of the liquid aerosol. The broad maximum of the OH feature shifts slowly with temperature from its room temperature value near 3430 cm^{-1} to near 3360 cm^{-1} , and the sulfate absorptions change in a way which is consistent with the temperature dependence of the equilibrium constants from H_2SO_4 ionization. (See section 4.4 for a further discussion of this shift.)

The three higher temperature spectra in figure 4.12 also have sharp (but weak) features in both the 3000 cm^{-1} and 1500 cm^{-1} regions. These features are due to water vapor, which is in equilibrium with the aerosol. Note that these sharp features are not caused by water vapor external to the cell. The optical path is purged from source to detector, and the final spectrum consists of the ratio of the sample to the background. In principle, the intensities of these water vapor absorptions could be used to provide a direct determination of the aerosol concentration, but because the signal to noise of these peaks is poor, such a calibration was not attempted. To produce extinction features arising from the aerosol particles alone, we have removed the water vapor lines from all other aerosol spectra displayed in this chapter. This was accomplished by subtracting from the aerosol spectra a spectrum of only water vapor.

The OH stretching region in the 170 K spectrum is significantly different than the OH stretching region in the higher temperature spectra: the OH band in the 170 K spectrum is more intense and the maximum is sharper. The subtraction of the 170 K spectrum from the 180 K spectrum makes these changes more apparent, as shown in figure 4.13. The solid line is the result of subtracting the higher temperature spectrum from the lower one. Thus, components that increase in concentration with decreasing temperature show an absorption change that is greater than zero. The significant changes that have occurred over the temperature range are indicated by arrows. There is an increase in the absorption intensity at 3230 cm^{-1} , which signals the appearance of ice in the aerosol particle, and also, there is a decrease in the absorption intensity at 3530 cm^{-1} , which signals the disappearance of liquid water. There are smaller changes in the sulfate ion features near 1000 cm^{-1} : the intensity of the SO_4^{2-} absorption band increases and the intensity of the HSO_4^- absorption band decreases.

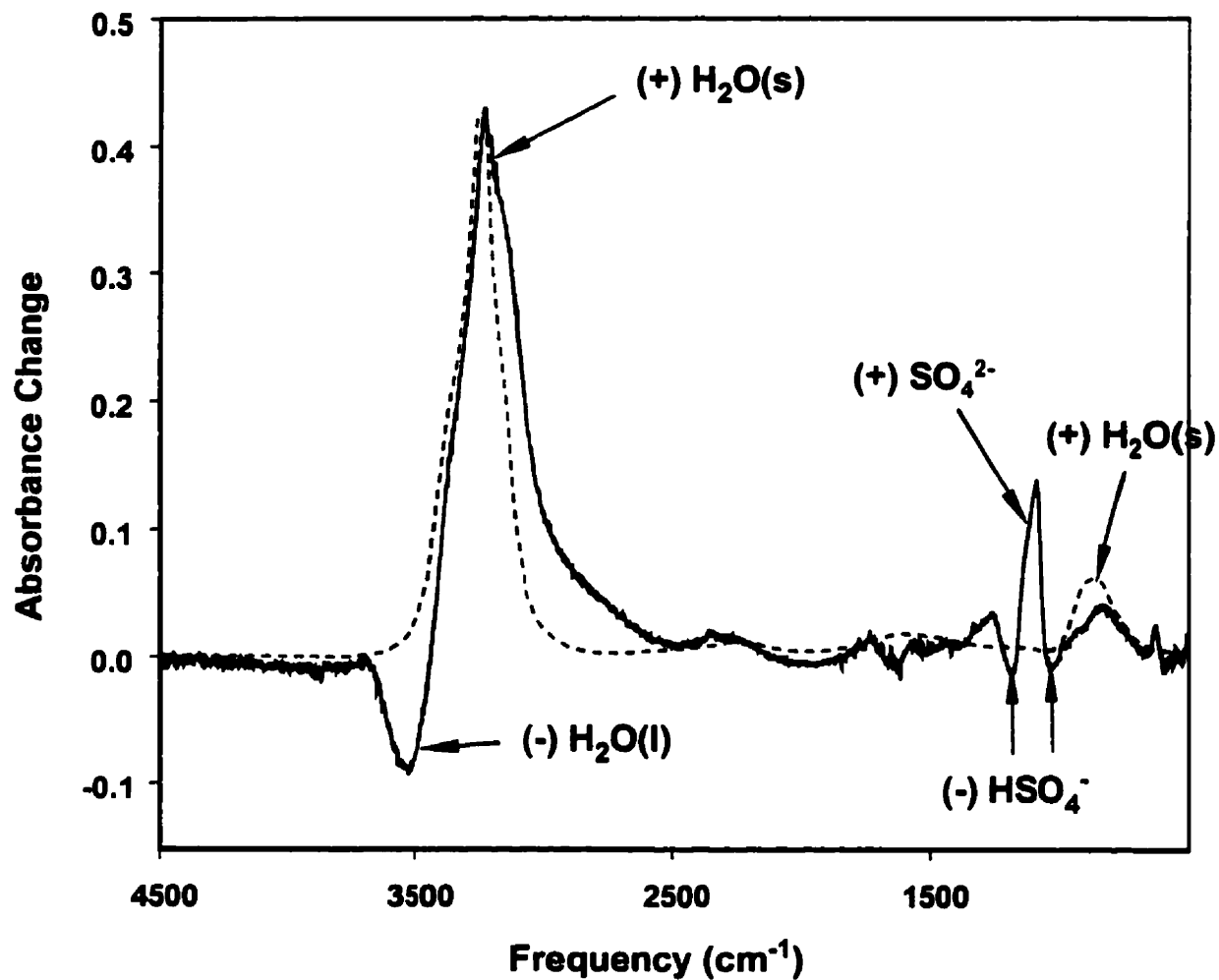


Figure 4.13 Solid spectrum: subtraction of the two lowest extinction spectra in figure 4.12. Excursions upward and downward from zero signify (respectively) increases and reductions in the concentrations of the components. Dashed spectrum: calculated spectrum of a H₂O(s) particle with size parameters $r_g=0.1 \mu\text{m}$ and $\sigma_g=1.0$.

To support our contention that the feature at 3230 cm^{-1} in the subtracted spectra represents the formation of ice, we show, as the dashed curve in the figure 4.13, a calculated spectrum of a monodisperse sample of ice particles that have radii of $0.1\text{ }\mu\text{m}$. The fact that the calculated curve matches the measured spectrum closely supports the suggestion that a very small crystal of ice has appeared in the sample. A radius of $0.1\text{ }\mu\text{m}$ was chosen because it is the largest size that gives a spectrum of this shape. The spectra of particles of this size and smaller all have essentially the same shapes.

The small differences between the calculated and measured curves in figure 4.13 are qualitatively in the directions expected from our proposed freezing mechanism. The measured curve should be below the calculated one on the high-frequency side, due to the disappearance of liquid water. The difference on the low-frequency side may be due to the assumption that the ice crystal is isolated; whereas, in reality the ice crystal is enclosed by an envelope of unfrozen sulfuric acid solution. This system would be more appropriately represented by a coated sphere calculation.

The changes just described and modelled represent ice formation inside the H_2SO_4 aerosol droplet, as opposed to the formation of an ice aerosol external to the H_2SO_4 droplets. The first cooling stage in the flow tube eliminates the latter possibility (this has been discussed in section 4.2). We have verified that no nucleation of ice particles occurs when pure water vapour is passed through the flow tube with the temperature profile used in our freezing experiments. The observed nucleation of ice in these experiments, therefore, must occur inside the aerosol droplet.

The precise temperature at which ice formed in the aerosol particles was determined by monitoring the 3230 cm^{-1} peak as a function of temperature. Initially, the intensity of this peak was determined directly from the absorption spectra, but the intensity changes were not large enough to determine the precise freezing temperature. To get a more accurate measure of the freezing point, we subtracted each spectrum from the one measured at the next lower temperature, as shown in figure 4.13. Then the measured change in the intensity of the 3230 cm^{-1} peak (determined from these subtraction spectra) was divided by the temperature difference between the two spectra. The result is the rate of change of the 3230 cm^{-1} feature with temperature. Results from this procedure are shown

in figure 4.14. We interpret the intensity of the feature at 3230 cm^{-1} in the subtracted spectra to be proportional to the amount of ice which has precipitated as a result of the decrease in temperature, so the amplitudes of the curves in Figure 4.14 are proportional to the amount of material which precipitates per degree K. Each of these curves has a rapid rise on the higher temperature side, goes through a maximum, then decreases until it reaches a point where the slope changes and a “tail” extends toward lower temperatures. These curves are approximately the numerical derivative of the change in amount of ice, so this shape indicates that, with decreasing temperature, the precipitation rate of ice increases rapidly at first, then decreases smoothly until the break in the curve, where the amount of ice continues to increase, but at a slower rate.

For the crystal growth rate to be important in the freezing process represented by figure 4.14, the diffusion time of H_2O molecules in the solution must be longer than the time the aerosols are at the freezing temperature. The diffusion time can be estimated with the following equation:

$$t = \frac{\pi}{D} \left(\frac{\langle x \rangle}{2} \right)^{1/2} \quad (4.2)$$

where $\langle x \rangle$ is the net distance travelled on average by a molecule in a time t if it is diffusing in a medium with a diffusion coefficient D . The diffusion coefficient, needed for equation 4.2, is defined as

$$D = \frac{kT}{6\pi\eta a} \quad (4.3)$$

where η is the solution viscosity, a is the effective radius of a H_2O molecule, T is the temperature, and k is the Boltzmann constant. Using these two equations, a solution viscosity of 5.0 P at 200 K, and an effective radius of 300 pm, we calculated that an H_2O molecule would take, on average, only 0.5 seconds to diffuse 0.75 microns which is the average diameter of our particles. Since this time is much shorter than the time the aerosol

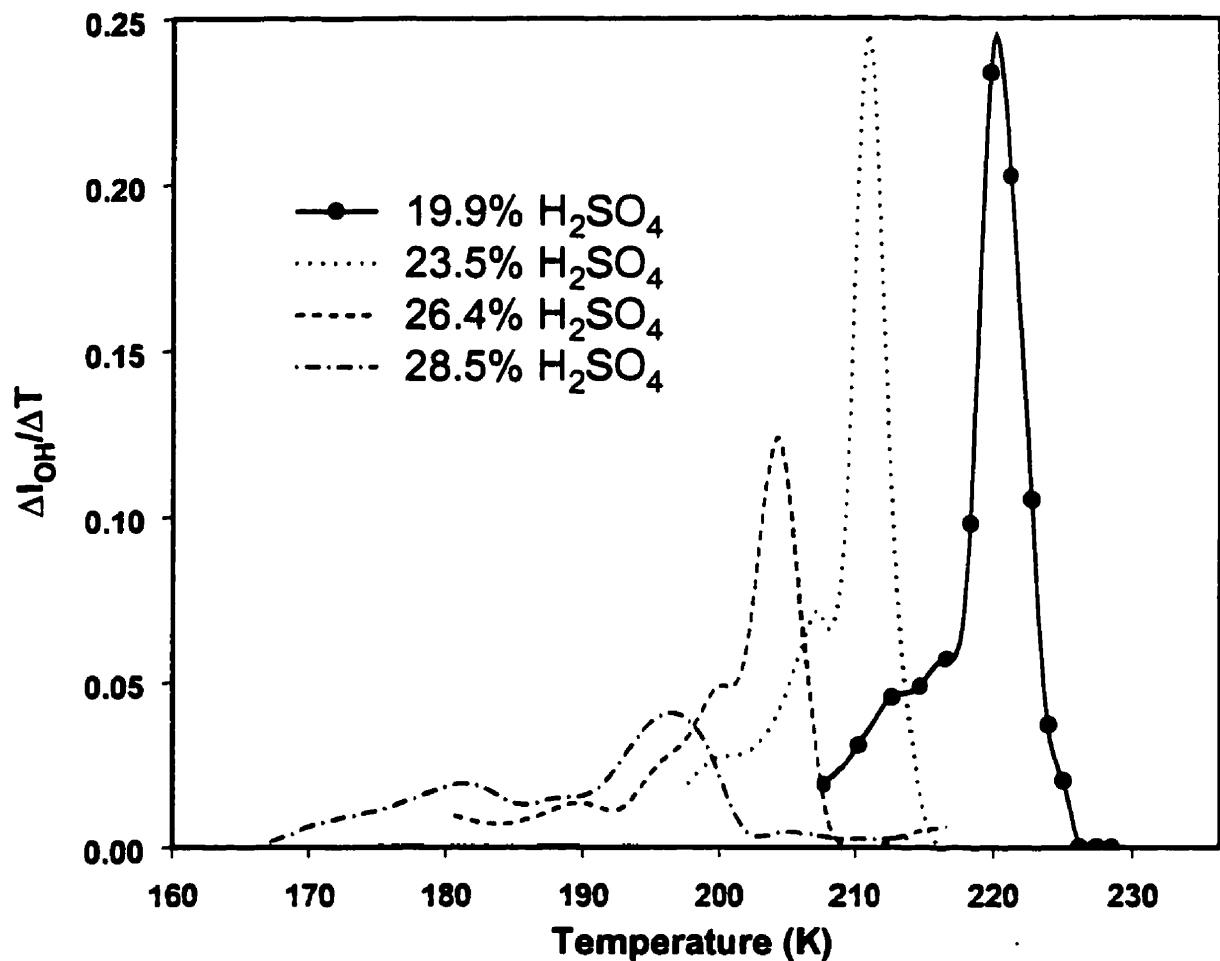


Figure 4.14 Rate of change of the 3230 cm⁻¹ feature, labeled (+)H₂O(s) in figure 4.13, with decreasing temperature for a range of aerosol concentrations. The curves are spline fits to the data points, which have been omitted from all except the 19.9 wt % data for clarity.

is at the low temperature (approximately 1 minute), crystal growth does not limit the freezing process.

Because the crystal growth rate is fast on the time scale of our experiments, the nucleation rate must determine the freezing rate. Accordingly, the finite width of the curves in figure 4.14 must reflect the fact that an ice nucleus forms and grows to its equilibrium size in an increasing number of the aerosol particles as the temperature decreases. In this event, the break in slope on the low-temperature side of the curves corresponds to the point at which an ice crystal has formed in all of the aerosol particles. The remaining “tails” on the curves denote the additional ice that precipitates as the system follows the solid-liquid equilibrium curve downward with decreasing temperature.

A freezing curve for dilute sulfuric acid aerosols, shown in figure 4.15, was constructed by plotting the temperatures at which ice first appears in the IR spectrum versus the concentration of the aerosols. The solid circular points are the results from the freezing measurements and the line going through the points is a least squares fit to the data. The point at zero wt % H₂SO₄ represents the freezing temperature of a liquid water aerosol, which we measured by the same spectroscopic technique in an earlier experiment. The particles used in the latter experiment were somewhat larger ($r_g = 1.2 \mu\text{m}$ and $\sigma_g = 1.55$). In view of this difference, an error bar of $\pm 3 \text{ K}$ is associated with this point; the other data have a temperature uncertainty of approximately $\pm 1.5 \text{ K}$. Also shown in figure 4.15 is part of the phase diagram for the sulfuric acid-water system. Our measured freezing points are about 35 K below the freezing temperatures predicted by the phase diagram.

The rate of homogeneous nucleation associated with the freezing curve in figure 4.15 curve can be calculated from classical nucleation theory.^{64,53} The rate limiting step in our H₂SO₄-H₂O experiments is homogeneous nucleation:



where J is the rate of formation of stable nuclei per unit volume and per unit time. Since the freezing process is not limited by the growth of the stable nuclei (proof of this was

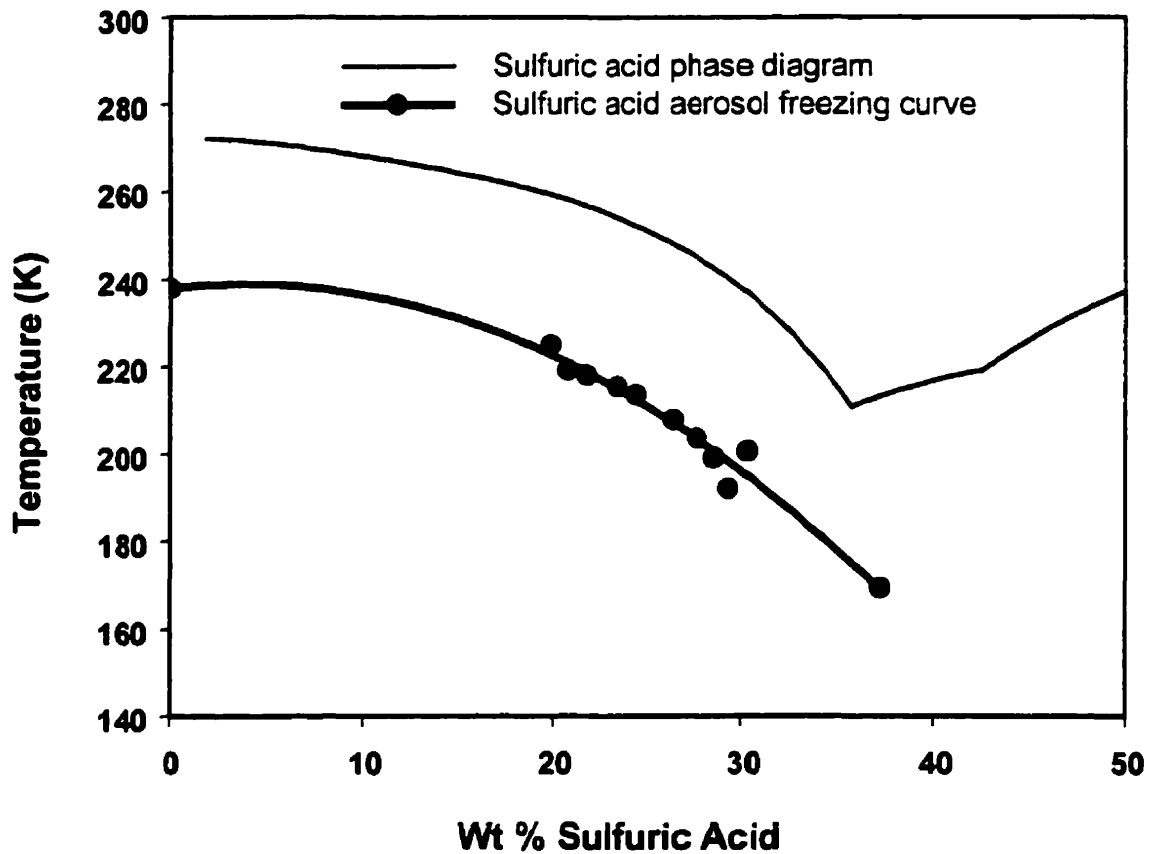


Figure 4.15 Freezing curve for dilute sulfuric acid aerosols. The solid circular points are the results from the freezing measurements and the line going through the points is a least squares fit to the data.

given above), the fraction of particles frozen [$F_s(t)$] reflects the homogeneous nucleation rate (J).^{64,53}

$$F_s(t) = 1 - \exp[-J(T)Vt] \quad (4.5)$$

where V is the volume of the particle and t is the time that the particles are held at the freezing temperature. This equation, however, only applies to monodisperse aerosols. As discussed in section 3.4, our aerosols are described by a log-normal function:

$$f(r) = \frac{1}{r \ln \sigma_g (2\pi)^{0.5}} \exp\left[-\frac{(\ln r - \ln r_g)^2}{2 \ln^2 \sigma_g}\right] \quad (4.6)$$

When the log-normal distribution is included in equation 4.5, the result is an equation that relates the homogeneous nucleation rate to experimental observables:

$$Volume_F_s(t) = \frac{\int_0^\infty f(r)V(r)[1 - \exp(-J(T)V(r)t)]dr}{\int_0^\infty f(r)V(r)dr} \quad (4.7)$$

In this equation, $Volume_F_s(t)$ represents the fraction of the total aerosol volume that has frozen in time t .

All the variables in equation 4.7, except J , are known from our experiment. Consequently, we can use equation 4.7 to calculate the J value associated with the freezing curve shown in figure 4.15. The time (t) that the aerosol is exposed to the freezing temperature is approximately 1 minute. The log-normal size distribution parameters (r_g and σ_g) are known from our size inversion technique (see section 4.3). In addition, the fraction of the total aerosol volume that has frozen [$Volume_F_s(t)$] in time t can be determined from figure 4.14 (see below).

As discussed above, the break in the slope of the low-temperature side of the curves in figure 4.14 corresponds to the point at which all the aerosol particles have an ice crystal,

and also, these curves represent the derivative of the change in the amount of ice. Consequently, the integral under one of these curves (from the high temperature side to the point where the slope on the low-temperature side breaks) is proportional to the total volume frozen. It follows that integrating a fraction of a freezing curve and dividing by the total area under the curve gives the fraction of the aerosol volume that has frozen [$Volume_{Fs}(t)$]. The fraction frozen associated with the freezing curve in figure 4.15 was determined by integrating from the onset of the freezing curve to the temperature where ice first appeared in the IR spectrum and by dividing this fractional area by the total area under the curve. For each point in figure 4.15, the calculated fraction frozen was slightly different. The average value was 5 % with an upper and lower limit of 7 % and 2 %, respectively. These limits were included in the uncertainty of the rate constant.

Using equation 4.7 and the experimental observables discussed in the previous two paragraphs, we determined that the homogeneous nucleation rate (J) associated with our freezing curve (figure 4.15) is between $4 \times 10^{10} \text{ cm}^{-3} \text{ sec}^{-1}$ and $1 \times 10^9 \text{ cm}^{-3} \text{ sec}^{-1}$. The uncertainty in J stems from the uncertainty in residence time of the aerosol, the uncertainty in the fraction frozen, and the uncertainty in the size parameters determined from figure 4.4.

In the above paragraphs, it was assumed that homogeneous nucleation was the dominant mechanism for the formation of stable nuclei. If heterogeneous nucleation had occurred several experimental inconsistencies would have resulted. First, freezing temperatures would have varied irreproducibly for different experiments, different gas bottles, and so forth, due to the different amounts of contamination expected to occur as the apparatus is disassembled for cleaning, window change, etc. Our observed freezing temperatures, however, followed a consistent and reproducible trend, as shown in figure 4.15. Furthermore, the typical particle number density for these experiments is approximately $1 \times 10^7 \text{ cm}^{-3}$ (this number was determined from Mie scattering calculations), and if dust particles contributed substantially to the freezing, either each of the particles would have to contain a dust particle, implying a very dirty gas supply, or some fraction of the sample would freeze at a notably different temperature from the rest, which was never observed.

4.5.2 Discussion

Mackenzie *et al.*⁶⁵, Jensen *et al.*⁵⁵, and Clapp *et al.*⁶⁶ have investigated the temperatures at which ice precipitates out of sulfuric acid-water particles and the associated homogeneous nucleation rates of this freezing process. The freezing curves and points determined by these authors as well as our freezing points are displayed in figure 4.16, which has been taken from Mackenzie *et al.* The solid curves, which were calculated by MacKenzie *et al.* using the "Turbull correlation", correspond to J values of, from the upper curve, 6.9×10^{-7} , 6.9×10^{-2} , 6.9×10^3 , 6.9×10^8 , and $6.9 \times 10^{13} \text{ cm}^{-3} \text{ sec}^{-1}$. The dashed curve, which was calculated by Jensen *et al.* using classical nucleation theory, corresponds to a J of $2.3 \times 10^{11} \text{ cm}^{-3} \text{ sec}^{-1}$. The triangles, which are the freezing temperatures reported by Clapp *et al.*, correspond to a J value of $7.4 \times 10^9 \text{ cm}^{-3} \text{ sec}^{-1}$, and finally, the rhombic points represent the freezing points from our measurements, which as mentioned previously correspond to a J value between $1 \times 10^9 \text{ cm}^{-3} \text{ sec}^{-1}$ and $4 \times 10^{10} \text{ cm}^{-3} \text{ sec}^{-1}$. Our J values are in reasonable agreement with both theory and the experimental data. At concentrations less than 25 wt % H_2SO_4 , our results are very similar to the calculations, whereas at higher concentrations, our measured freezing temperatures are approximately 10 K below the calculations. Similarly, our freezing temperatures agree with the Clapp *et al.* data at 25 wt % H_2SO_4 , but our freezing temperatures are approximately 10 K below the Clapp *et al.* data at concentrations greater than 30 wt % H_2SO_4 . The Clapp *et al.* experimental technique is very similar to our technique; therefore, the difference in the final results is likely due to the different methods of concentration determination. Our concentrations were determined by a size dependent calibration curve, whereas Clapp *et al.* determined their concentrations with a thin-film calibration curve.

Our work has shown that ice precipitates out of sub-micron aerosols in less than approximately 1 minute for acid concentrations less than 35 wt % H_2SO_4 . Recent models, however, have suggested that the stratospheric sulfate aerosol will not become more dilute than approximately 45 wt % H_2SO_4 .^{22,23} Consequently, the formation of ice in a binary $\text{H}_2\text{SO}_4\text{-H}_2\text{O}$ aerosol is not a possible mechanism for solid PSC formation. Cirrus clouds, however, are believed to form by this mechanism.^{62,63} Prior to the publication of our

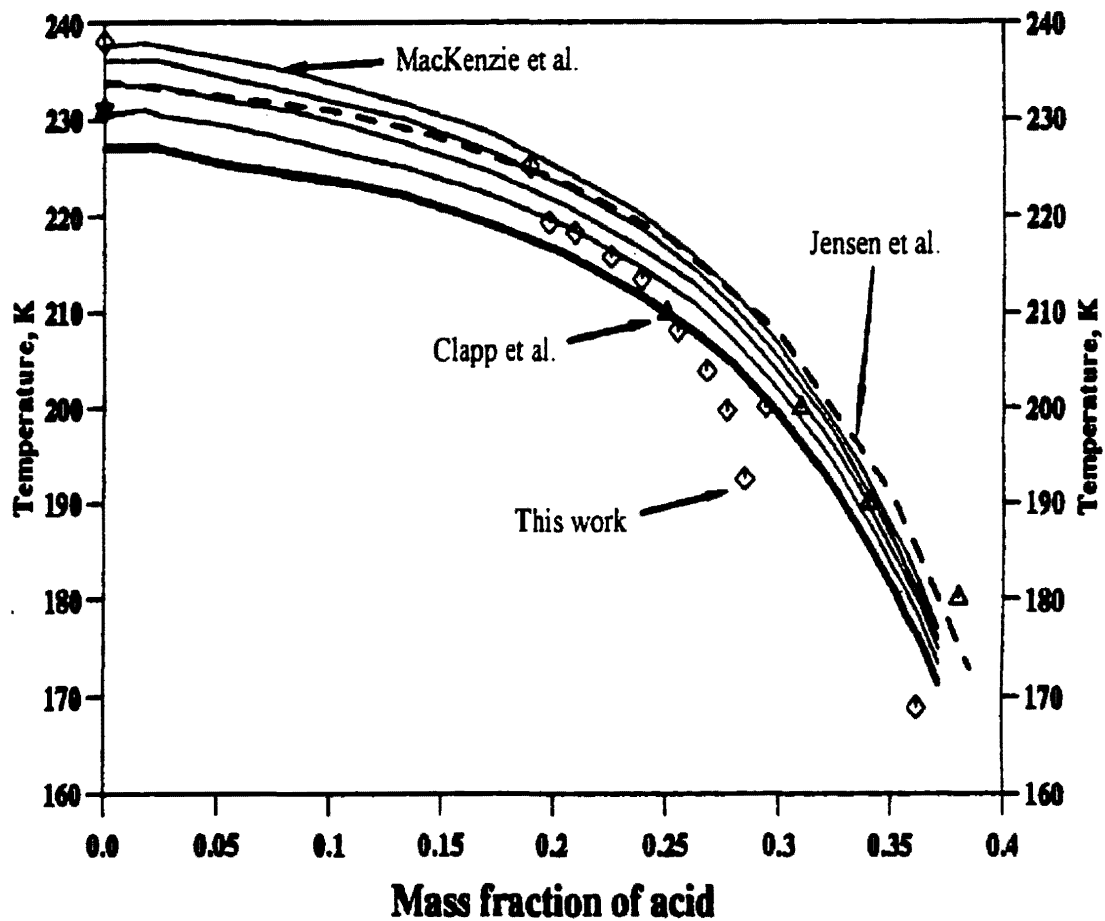


Figure 4.16 Comparison of theoretical freezing curves with experiments. The solid curves correspond to J values of, from the upper curve, 6.9×10^{-7} , 6.9×10^{-2} , 6.9×10^3 , 6.9×10^8 , and $6.9 \times 10^{13} \text{ cm}^{-3}\text{sec}^{-1}$. The dashed curve corresponds to a J value of $2.3 \times 10^{11} \text{ cm}^{-3}\text{sec}^{-1}$, and the triangles correspond to a J value of $7.4 \times 10^9 \text{ cm}^{-3}\text{sec}^{-1}$. A J value between 1×10^9 and $4 \times 10^{10} \text{ cm}^{-3}\text{sec}^{-1}$ is associated with the rhombic points. (Figure taken from reference 65)

results, no experimental data existed that could confirm this mechanism. Our results have confirmed this mechanism, as well as provided rate constants, which can be used in modelling studies of cirrus cloud formation.

4.6 CONCENTRATED H₂SO₄-H₂O AEROSOLS

4.6.1 Results

Freezing measurements similar to the ones described in the previous section were performed on concentrated (>35 wt %) H₂SO₄-H₂O aerosols. The concentrations investigated in this work cover the entire range of importance to current stratospheric models. The primary goal was to determine if H₂SO₄-H₂O aerosols with these concentrations freeze when exposed to stratospheric temperatures. The vertical lines in figure 4.17 show the concentration and temperature ranges investigated. Each solid line corresponds to one experiment where an aerosol of a certain composition was monitored over a range of temperatures. Included in this figure for comparison purposes is the phase diagram of the sulfuric acid-water system, our freezing curve which was described in the previous section, and the temperature-concentration trend of SSAs predicted by the Tabazadeh *et al.*⁵¹ model.

Figure 4.18 shows results from the freezing experiment performed on a 36 wt % H₂SO₄ aerosol. The only major change in the aerosol spectrum with cooling is ratio of SO₄²⁻ and HSO₄⁻. At the warmest temperature, the three peaks due to HSO₄⁻ (1167, 1054, and 898 cm⁻¹) are predominant, while at the coldest temperature the largest SO₄²⁻ peak (1125 cm⁻¹) predominates. In addition to the change in the sulfate region, there is also a minor narrowing and shifting of the OH band with decreasing temperature. However, there are no distinctive features in the spectrum that indicate freezing of the particles. (If ice or a hydrate did form in the liquid particles, the band shapes and intensities in the spectrum would be significantly different.)^{19,56}

Figure 4.19 shows a second series of spectra from these experiments. In this case, spectra as function of temperature are shown for a 60 wt % H₂SO₄ aerosol. The only major change with decreasing temperature is the shift in the SO₄²⁻ and HSO₄⁻ ratio. This is the same trend that was observed in the 36 wt % H₂SO₄ spectra. In fact, a similar trend was

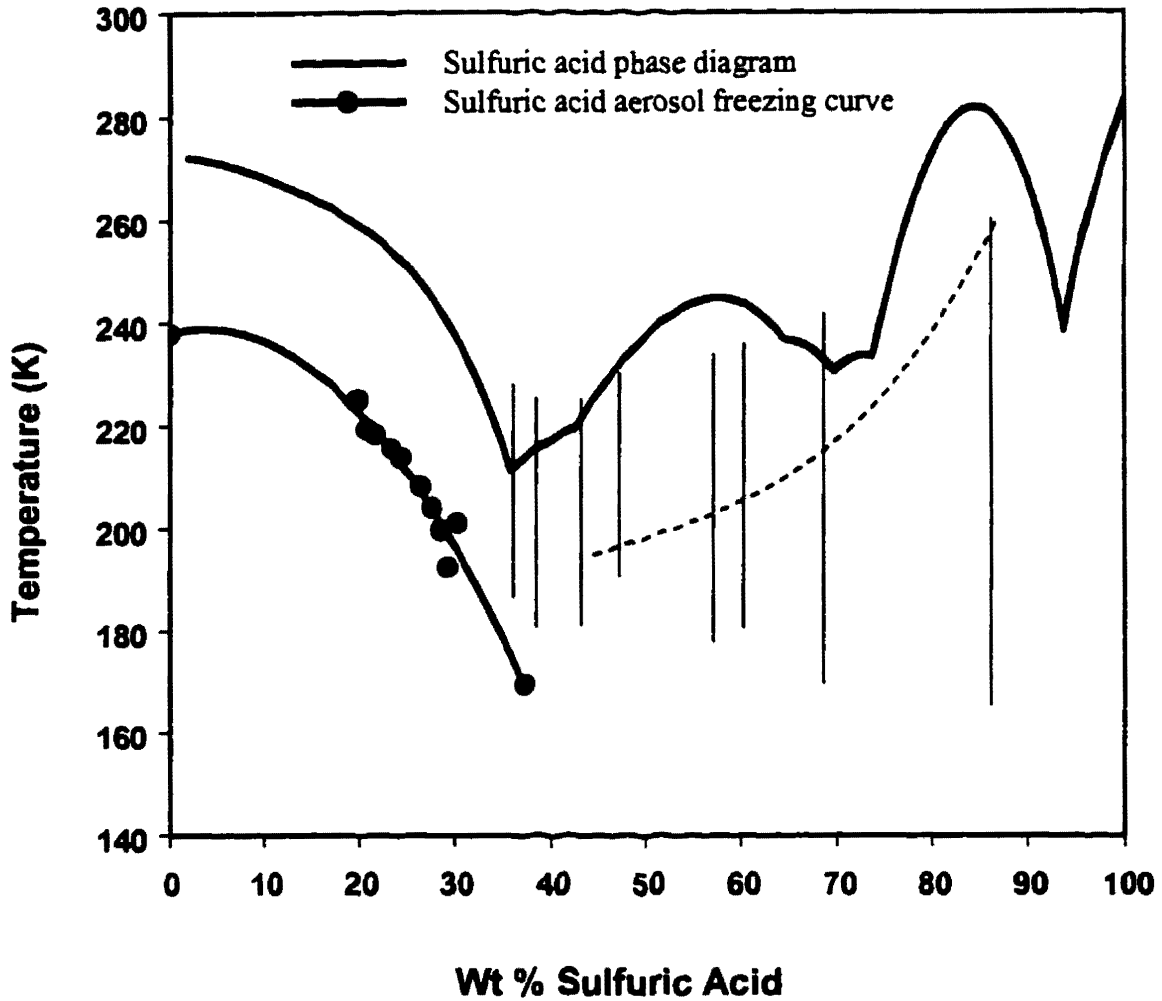


Figure 4.17 The vertical lines represent the concentrations and temperatures used in the freezing measurements. Each solid line corresponds to one experiment where an aerosol of a certain composition was monitored over a range of temperatures. The dashed line is the expected compositions of stratospheric sulfate aerosols exposed to 5 ppmv of water vapor at 50 mbar altitude.

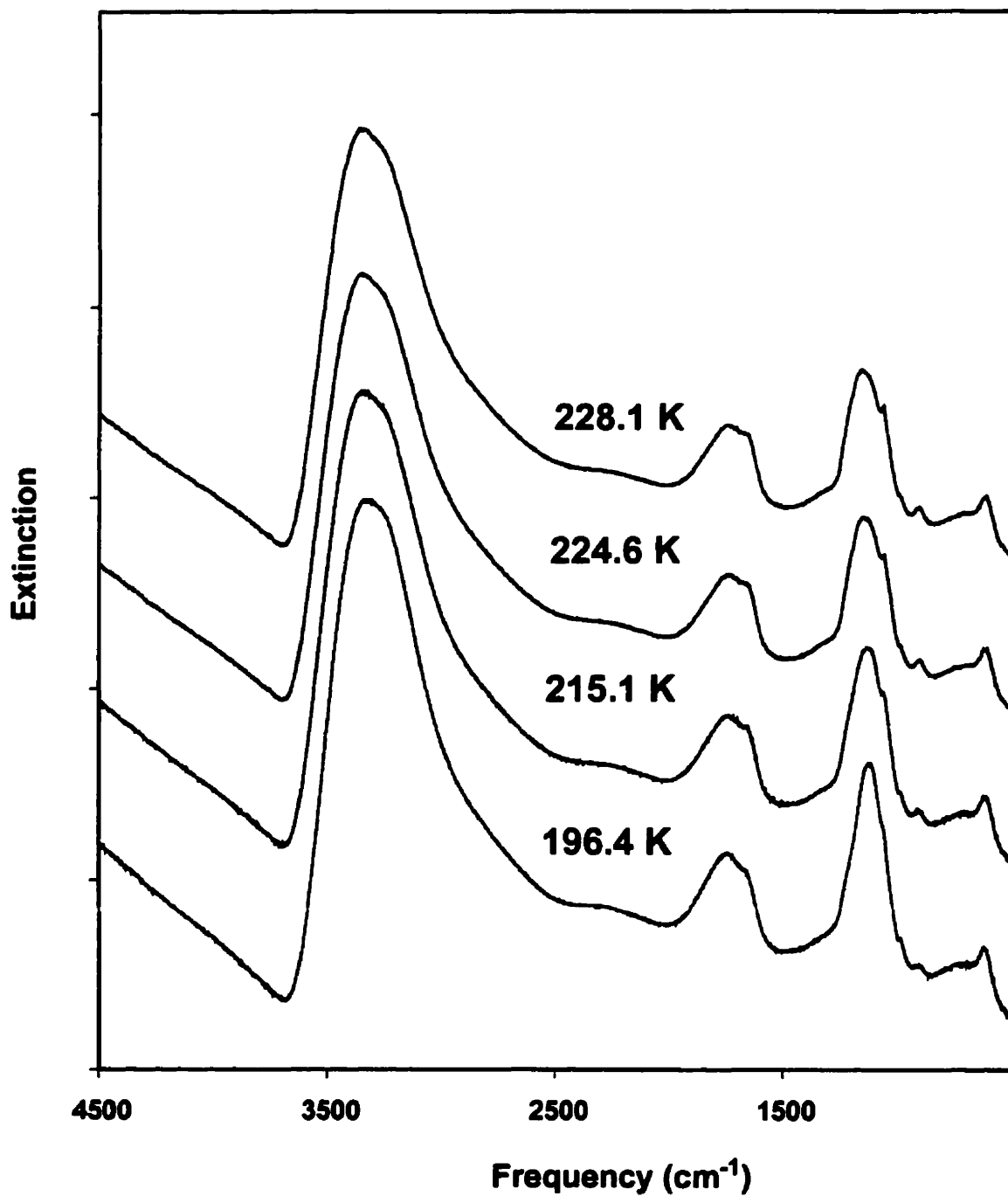


Figure 4.18 Temperature dependent spectra of a 36 wt % H₂SO₄ aerosol. The spectra have been offset in the vertical direction for clarity.

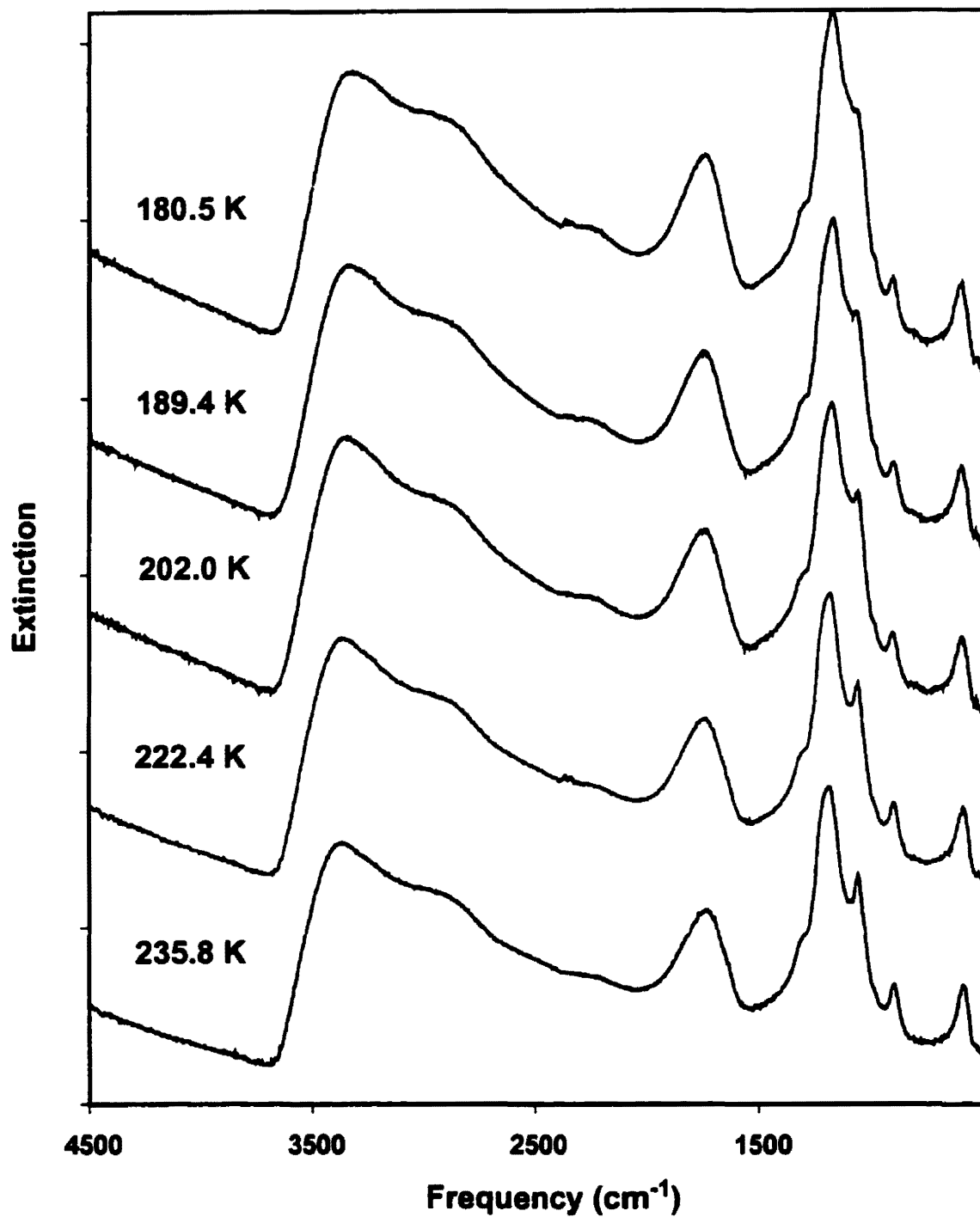


Figure 4.19 Temperature dependent spectra of a 60 wt % H₂SO₄ aerosol. The spectra have been offset in the vertical direction for clarity.

observed for all concentrated aerosols (>35 wt % H₂SO₄): no changes occurred which could be attributed to crystallization of the aerosol. In addition to monitoring absorption spectra as a function of temperature, we also took ratios of successive spectra to make changes more discernable. (This technique was also used in the dilute work to detect the precise temperature at which ice formed in the aerosol.) Even using this sensitive technique, we did not see any changes that could be associated with freezing.

The compositions and temperatures we investigated cover the relevant stratospheric temperatures and compositions, as illustrated by the overlap of the vertical lines and the composition-temperature trend in figure 4.17. In these experiments, no signs of freezing were observed. Therefore, our results show that sub-micron aerosols of sulfuric acid and water do not freeze in less than approximately 1 minute when stratospheric temperatures and compositions are used.

From our measurements, we can estimate an upper limit of the homogeneous nucleation rate for concentrated H₂SO₄-H₂O aerosols. Since the conditions (flow rates and particle sizes) for the concentrated experiments were approximately the same as the dilute experiments, the upper limit is the largest J value determined in the previous section: $4 \times 10^{10} \text{ cm}^{-3} \text{ sec}^{-1}$. This, of course, assumes that our sensitivity to freezing, which was previously estimated to be 5 % of the total aerosol volume, is the same in both the dilute and concentrated experiments.

4.6.2 Discussion

Since our original investigation of sulfuric acid-water aerosols, several researchers have reported on the freezing properties of micron and sub-micron droplets of sulfuric acid and water.^{60,66,67,68} In all these studies, no freezing was observed for concentrated droplets (>35 wt % H₂SO₄) at stratospherically relevant temperatures (>194 K), a result which is consistent with our findings. Upper limits for J ranging from 1×10^{10} to $1 \times 10^3 \text{ cm}^{-3} \text{ sec}^{-1}$ were determined in these studies.

One group of researchers, Imre *et al.*, did observe freezing of H₂SO₄-H₂O droplets with concentrations greater than 35 wt %.⁶⁹ These authors reported that 44 wt % H₂SO₄-H₂O particles freeze to sulfuric acid octahydrate at 166 K. This finding is not inconsistent

with other results because 166 K is well below the temperatures investigated by most researchers. Researchers, including ourselves, who did investigate freezing properties at this low temperature, did not see the octahydrate form because of the differences in observation times. Imre *et al.* noted that it took approximately 4 to 5 hours for the aerosol to completely crystallize as sulfuric acid octahydrate.

For 10 % of the stratospheric sulfate aerosol to freeze within 1 year (comparable to the natural lifetime of the sulfate aerosol) sulfuric acid solutions must have a J value larger than $1 \times 10^6 \text{ cm}^{-3} \text{ sec}^{-1}$. This value was determined from equation 4.5 and from the assumption that stratospheric particles have a diameter of 0.1 microns. Carleton *et al.*, however, reported for stratospheric conditions an upper limit of approximately $1 \times 10^3 \text{ cm}^{-3} \text{ sec}^{-1}$ for J .⁶⁷ In addition, recent experiments indicate that bulk samples of sulfuric acid and water do not freeze under stratospheric conditions.^{24,70} These measurements provide an even better constraint for the homogeneous nucleation rate because of the larger sample sizes and longer observations times used in bulk experiments. For example, Koop *et al.* determined an upper limit of $1 \times 10^{-2} \text{ cm}^{-3} \text{ s}^{-1}$ using bulk samples.⁷⁰ This experimental evidence reveals that homogenous freezing of stratospheric $\text{H}_2\text{SO}_4\text{-H}_2\text{O}$ aerosols is an unimportant step in the transition diagram displayed in figure 1.1.

CHAPTER FIVE

HNO₃-H₂O AEROSOLS

5.1 INTRODUCTION

Recent equilibrium models predict that stratospheric sulfate particles take up gas phase HNO₃ at temperatures below approximately 200 K.^{22,23} (This of course assumes the sulfate aerosol remains liquid down to 200 K.) These models predict that stratospheric particles are sulfuric acid-water solutions at temperatures greater than approximately 200 K, ternary solutions at temperatures between 200 K and 190 K, and dilute solutions of nitric acid and water, with a small fraction of sulfuric acid (< 5 wt %) at temperatures below approximately 190 K. This change in particle composition with decreasing temperature is shown in figure 5.1. The curves, reproduced from reference ²³, were calculated with the following parameters: 5 ppmv of H₂O, 5 ppbv of HNO₃, 0.036 mg/m³ of H₂SO₄ and a total pressure of 100 mbar. The solid line in this figure shows how the composition of the binary sulfuric-acid aerosol would change if gas phase uptake of HNO₃ did not occur.

In addition to the equilibrium models, Meilinger *et al.*²⁶ and Tsias *et al.*²⁷ showed that rapid temperature fluctuations in the stratosphere can cause the liquid ternary aerosols described above to depart considerably from their equilibrium compositions due to the diffusively hindered uptake of HNO₃ by large droplets. (Such rapid temperature fluctuations can be produced from mountain waves: a sudden rise in an air mass as it passes over a mountainous region.) These non-equilibrium models predict that the composition of the small droplets can approach a pure binary nitric acid solution with nitric acid concentrations ranging from 52 to 58 wt % acid and sulfuric acid concentrations less than .01 wt % (step 8 in figure 1.1). This finding led the authors of the non-equilibrium models to speculate that the nitric acid-water aerosols formed during rapid temperature fluctuations would freeze as nitric acid trihydrate or nitric acid dihydrate (step 9 in figure 1.1).

The nitric acid-water system has received considerable attention in the past. Previous work, which has included phase diagram,^{71,72} vapor pressure,^{73,16} and

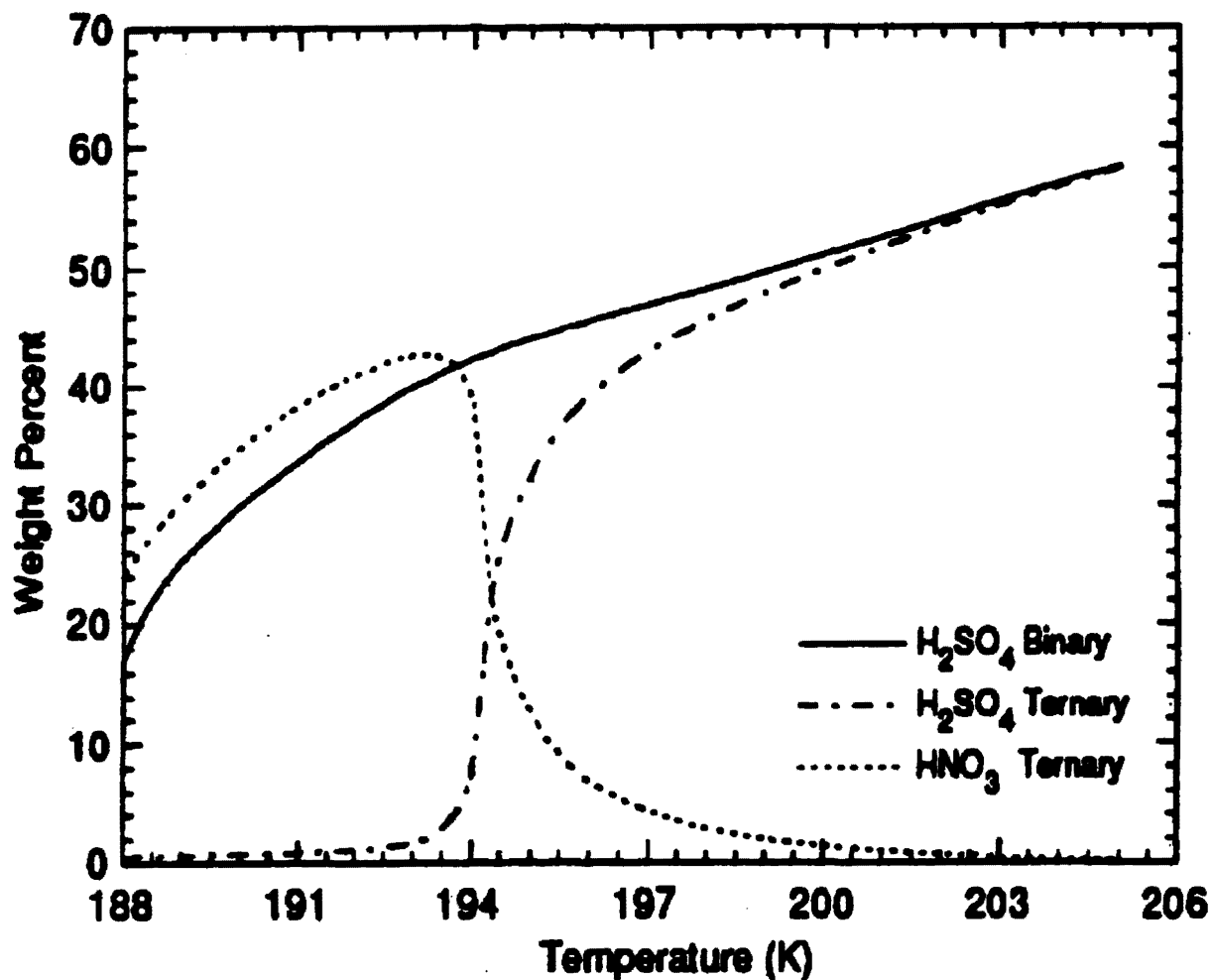


Figure 5.1 Expected composition of polar stratospheric aerosols as a function of temperature. The curves were calculated using the following conditions: 5 ppmv of H₂O, 5 ppbv of HNO₃, 0.036 mg/m³ of H₂SO₄ and a total pressure of 100 mbar. The solid line shows how the composition of the binary sulfuric acid-water aerosol would change with temperature if gas phase uptake of HNO₃ did not occur. (Figure reproduced from reference 23)

spectroscopic studies,^{74,75} has identified three stable hydrates: nitric acid monohydrate (NAM), nitric acid dihydrate (NAD), and nitric acid trihydrate (NAT). The stability regions of these hydrates as well as the stability regions of ice and solid nitric acid are displayed in figure 5.2.⁷² Clearly, the solid-liquid co-existence temperature for all compositions is well above polar stratospheric temperatures. This supports the “Meilinger *et al.* and Tsias *et al.* freezing mechanism,” but as mentioned repeatedly in this thesis, the kinetics of liquid-to-solid phase transitions must also be considered.

Several researchers have investigated the freezing kinetics of bulk nitric acid solutions with concentrations similar to those predicted by Meilinger *et al.* and Tsias *et al.* (52 to 58 wt % HNO₃). Molina *et al.* observed crystallization in less than 12 minutes at 196 K for 48 % wt HNO₃ solutions.²⁴ Song observed freezing within one hour at temperatures ranging from 217 K to 205 K for concentrations ranging from 53 to 64 % wt HNO₃.³³ Finally, Koop *et al.*, using concentrations ranging from 45 to 64 wt % HNO₃, observed rapid freezing at temperatures ranging from 214 K to 226 K.⁷⁰ The work from these three groups suggest that solutions with concentrations ranging from 45 to 64 wt % exhibited fast nucleation and crystallization at polar stratospheric temperatures. The solutions probed by these researchers, however, were in contact with a surface. As a result, the observed freezing temperatures are only upper limits to the true homogenous freezing temperatures due to the possibility of heterogeneous nucleation. It is not clear from these results whether the same fast rates will be observed for micron sized droplets free of heterogeneous nucleation sites.

The uncertainties about the freezing kinetics of nitric acid-water aerosols make it clear that direct laboratory measurements on HNO₃-H₂O aerosols are needed. Accordingly, we performed a series of experiments that addressed these uncertainties. Experiments included freezing measurements on 3:1 (moles H₂O:moles HNO₃) and 2:1 stoichiometric particles and freezing measurements of non-stoichiometric particles ranging in composition from 3:1 to 1.2:1. This research, which has been partially reported in the literature,^{76,77} is described in this chapter. The goal of this research was to understand the freezing of nitric acid-water aerosols in general and to determine the feasibility of the “Meilinger *et al.* and

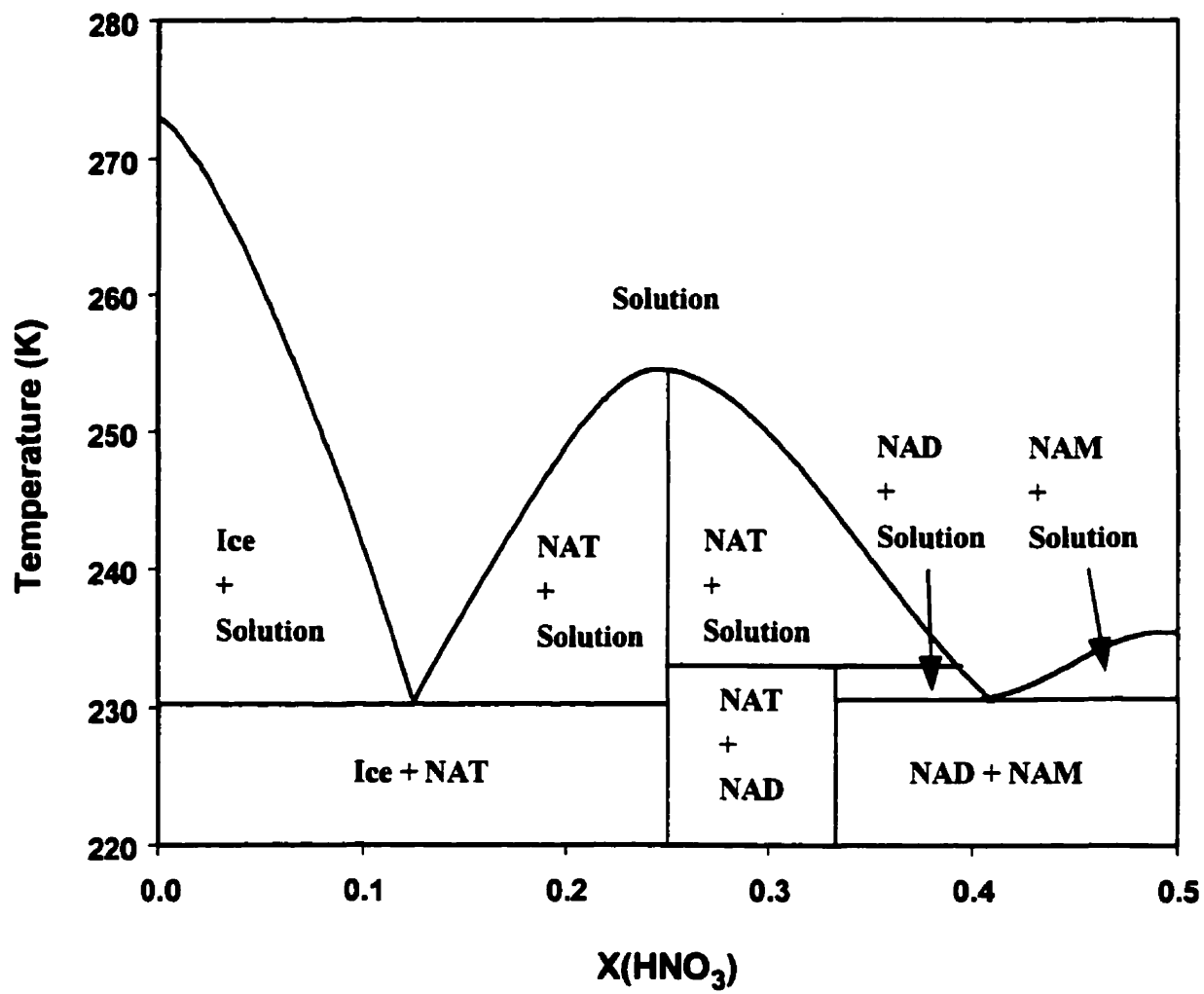


Figure 5.2 Phase diagram of the nitric acid-water system. The figure was reproduced from reference 72.

Tsias *et al.* freezing mechanism” (step 9 in the transition diagram displayed in figure 1.1) in particular.

5.2 NITRIC ACID DIHYDRATE AEROSOLS

The first crystalline phase we observed while studying nitric acid-water aerosols was nitric acid dihydrate (NAD). Upon further investigation, we noticed that this crystal formed readily for a range of aerosol compositions. This finding led us to investigate in detail the freezing properties of 2:1 aerosols. (The notation $x:y$, where x refers to moles of water and y refers to moles of nitric acid, is used almost exclusively in this chapter to define the composition). First, a technique of generating and characterizing a 2:1 liquid aerosol was developed, and then freezing measurements were performed on this stoichiometric aerosol. The spectroscopic techniques used in these measurements are the same as in the sulfate experiments, but several aspects of this experiment are either different or improved since the sulfate work.

5.2.1 Experimental

A schematic of the flow tube used in these measurements is shown in figure 5.3. The flow tube, 3.5” ID, consists of three copper sections separated and thermally isolated by thin-walled stainless steel bellows. The first (inlet) and second sections are each 9” long and the final (observation) section is 23” long. The temperatures of all three sections can be varied independently from room temperature to 120 K by flowing cooled N_2 through copper tubing soldered to the walls of each section. The thermal isolation provided by the thin walled stainless bellows permits temperature differences of 100 K to exist between adjacent sections, while their individual temperatures can be stabilized to better than ± 1.5 K. The flow tube is mounted inside a 6” square stainless steel vacuum jacket, for thermal insulation.

Three copper/constantan thermocouples, accurate to ± 1 K, are fixed to the wall of each of the inlet and middle sections, and four are located on the wall of the observation section. These temperatures are monitored continuously during each experiment and do not vary by more than ± 1.6 K - the total temperature uncertainty - during the experiment.

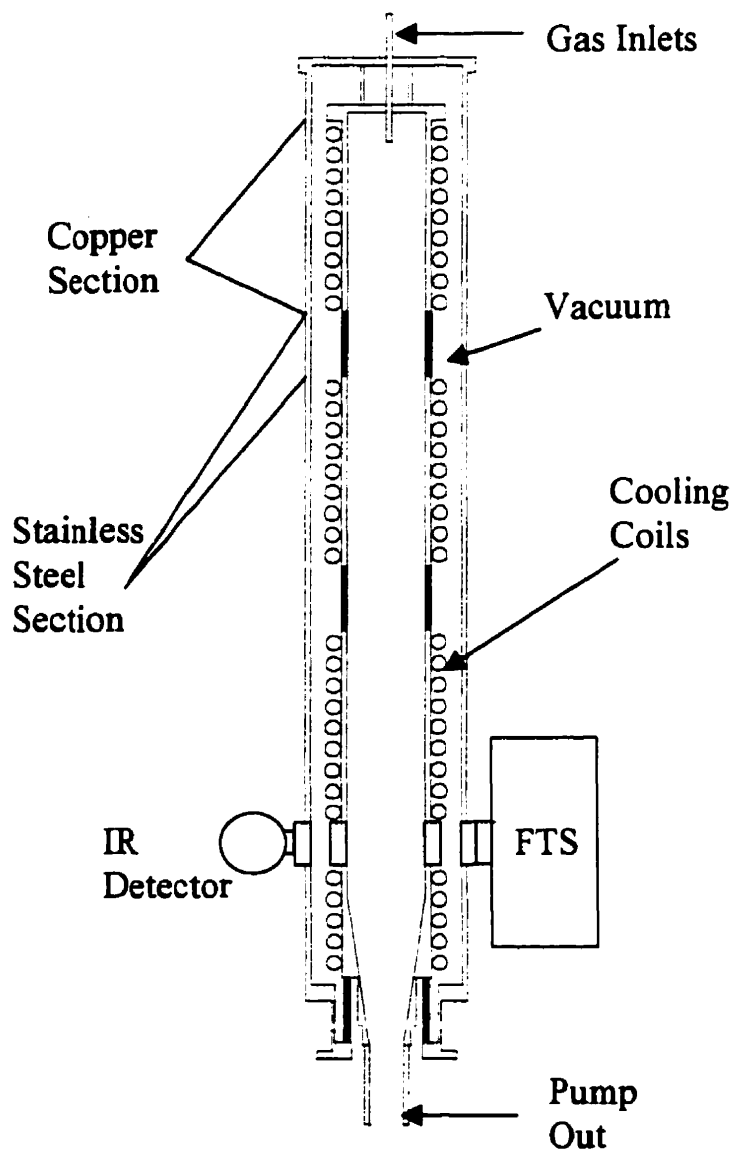


Figure 5.3 Schematic cross section of the double walled flow tube apparatus. Not all gas and coolant inlets are shown. Coolant circuits for all three copper sections are independent.

To determine how rapidly the gas temperature equilibrates with the wall temperature of this new flow tube, a long nylon rod fitted with two thermocouples was moved axially along the tube, to measure directly the gas temperature profile along the centre axis of the flow tube. In addition, thermocouples fixed to a small arm attached to the rod at right angles to its axis were used to look for radial temperature gradients. Under typical experimental conditions (flow: 2.5 SLPM; pressure: 250 torr) these measurements showed that the temperature of the gas radially across the tube is within 1 K (the accuracy of the thermocouples) of the wall temperature in each of the sections, and the axial gas temperature reaches the wall temperature within the first inch after the gas enters a cooling section. Thereafter the radial and axial temperature gradients in each of the sections are less than the uncertainty quoted above.

The aerosol extinction spectra are recorded with a Mattson 6021 spectrometer operating at 8 cm^{-1} resolution over the range 4500 cm^{-1} to 500 cm^{-1} . The observations are made in single pass mode perpendicular to the flowing aerosol stream through ZnS windows located near the end of the final section. In a similar manner to the sulfuric acid experiments, background spectra are recorded immediately before the aerosol is introduced into the tube and immediately after the freezing experiment when the aerosol flow is shut off. In all cases the spectra were identical; as a result, the recorded extinction spectra are of the suspended aerosol, not aerosols deposited on the windows.

Nitrogen carrier gas is first passed through a 5 SLPM Omega mass flow meter and then split into two streams, each of which is further metered through a floating ball flow meter, then directed through two saturators containing nitric acid and water. The two flows are then recombined and enter the flow tube. The temperatures of both the first and second sections of the flow tube are maintained at 188 K for all of the experiments reported here. This causes condensation of the mixture of nitric acid and water vapors and production of liquid nitric acid particles, but does not cause crystallization of the liquid particles. This was verified by holding the final section at 188 K and observing the characteristic spectrum of the liquid particles. The liquid particles produced in the first sections flow into the final (observation) section, where the temperature is carefully controlled at a value ranging from

188 K down to less than 160 K. IR spectra are recorded at various temperatures of the observation section.

The required aerosol composition (2:1 HNO₃:H₂O) is determined directly from the extinction spectra. This is an important aspect of the experiment, so the following detailed procedure was developed to establish the flow rates of the separated carrier gas streams needed to produce NAD, which is a precise 2:1 aerosol. First, the approximate flows are determined by comparing aerosol extinction spectra (taken at low temperatures, known to produce crystallization) with published thin film NAD spectra.⁷⁵ Visual comparison of the spectra cannot give the NAD composition accurately, however, because features characteristic of NAD appear in the experimental spectra over a wide range of vapor compositions. Figure 5.4 will be used to illustrate the remaining steps necessary to ensure that the H₂O-HNO₃ composition ratio is that of NAD. Curves (a), (b), and (c) respectively, are experimental spectra for which the H₂O-HNO₃ ratio is less than, approximately equal to and greater than 2. Curve (d) is a calculated NAD aerosol spectrum, generated with optical constants derived from thin film measurements⁷⁸ and a particle size distribution determined by fitting to our measured spectra. Comparison of spectrum (d) with the others shows that the major features of NAD are present in all three experimental spectra.

The 947 cm⁻¹ feature, which is present in thin film spectra of solid HNO₃ and also liquid solutions of HNO₃ and H₂O but absent from the spectra of the crystalline mono- di- and tri-hydrates, indicates molecular HNO₃.^{15,75} The 3490 cm⁻¹ and 3255 cm⁻¹ peaks are OH frequencies characteristic of H₂O occupying different positions in the NAD crystal.^{15,75} The 3255 cm⁻¹ feature is very close to the peak of the broad OH band in liquid H₂O-HNO₃ at about 3305 cm⁻¹. The edge of liquid band also underlies part of the 3490 cm⁻¹ peak, but its effect on the area of the 3255 cm⁻¹ peak is much greater, and consequently, the area ratio A(3255)/A(3490) is a minimum when all of the H₂O is in crystalline NAD. The enhancement of the 3255 cm⁻¹ band in spectrum (c) indicates the presence of liquid solution due to an excess of H₂O.

To achieve a 2:1 concentration, we adjust the flows until a spectrum like (a) is produced, which has excess HNO₃, as indicated by the presence of the peak at 947 cm⁻¹. Then the flow of the HNO₃ carrier gas is decreased in steps while holding the H₂O carrier

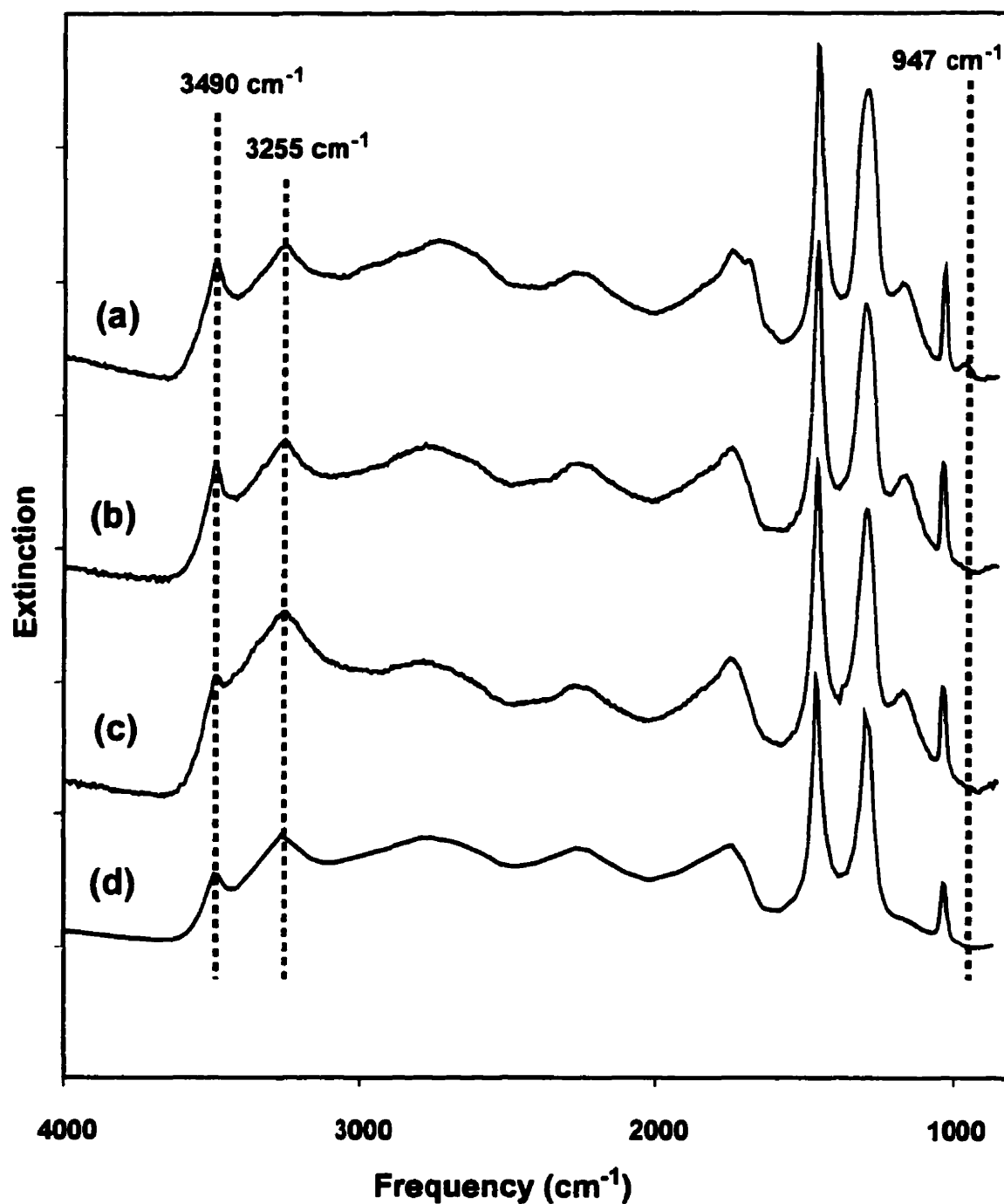


Figure 5.4 Low-temperature NAD aerosol spectra. Curves a, b, and c are measured spectra, for which the $\text{H}_2\text{O}/\text{HNO}_3$ ratio is less than, approximately equal to, and greater than 2, respectively. Curve d is a calculated spectrum. The spectra have been offset in the vertical direction.

gas flow constant. Spectra and flow meter readings are taken at each step until a spectrum like (c) is observed, where the 947 cm^{-1} peak has disappeared and the ratio $A(3255)/A(3490)$ has increased significantly. The area ratio $A(3255)/A(3490)$ and the area of the 950 cm^{-1} peak in the spectra are measured, and plotted as a function of the HNO_3 carrier gas flow.

The resulting plot is shown in figure 5.5. The solid curve, referenced to the vertical axis on the left, is the $A(3255)/A(3490)$ area ratio. The dashed curve, referenced to the vertical axis to the right is the normalized area of the 947 cm^{-1} peak. The former is small when there is no liquid, and the latter is zero if all HNO_3 is in the form of NAD. Both are small at the point where the entire sample is composed of pure NAD. Figure 5.5 shows that there is a unique flow ratio that causes both to be small simultaneously. This flow ratio is assumed to be that which produces pure NAD. The horizontal axis in figure 5.5 simply indicates the observation number; the HNO_3 carrier gas flow was decreased by approximately equal amounts between observations. The uncertainty in the flow rates and integrations contribute to an overall uncertainty in the aerosol composition of $\pm 0.05:1$ (moles H_2O : moles HNO_3).

A freezing measurement consists of cooling the first two sections of the flow tube to 188 K and the final section of the flow tube to 173 K (the temperature at which 2:1 aerosols completely crystallize). Then flows that produce an aerosol composed of pure crystalline NAD are established as described above. When the correct 2:1 stoichiometry has been achieved, the measurement is carried out by increasing the temperature of the final section slowly, and taking spectra at regular temperature intervals, while holding the temperature of the first two sections at 188 K. The complete temperature profile of the flow tube walls is recorded as each spectrum is taken. Near the expected phase transition, spectra are recorded at temperature intervals in the final section of approximately 1 K. As noted in section 3.2, the experiment consists of the continuous creation, cooling and freezing of new particles, rather than the observation of the same sample of particles over a long time period.

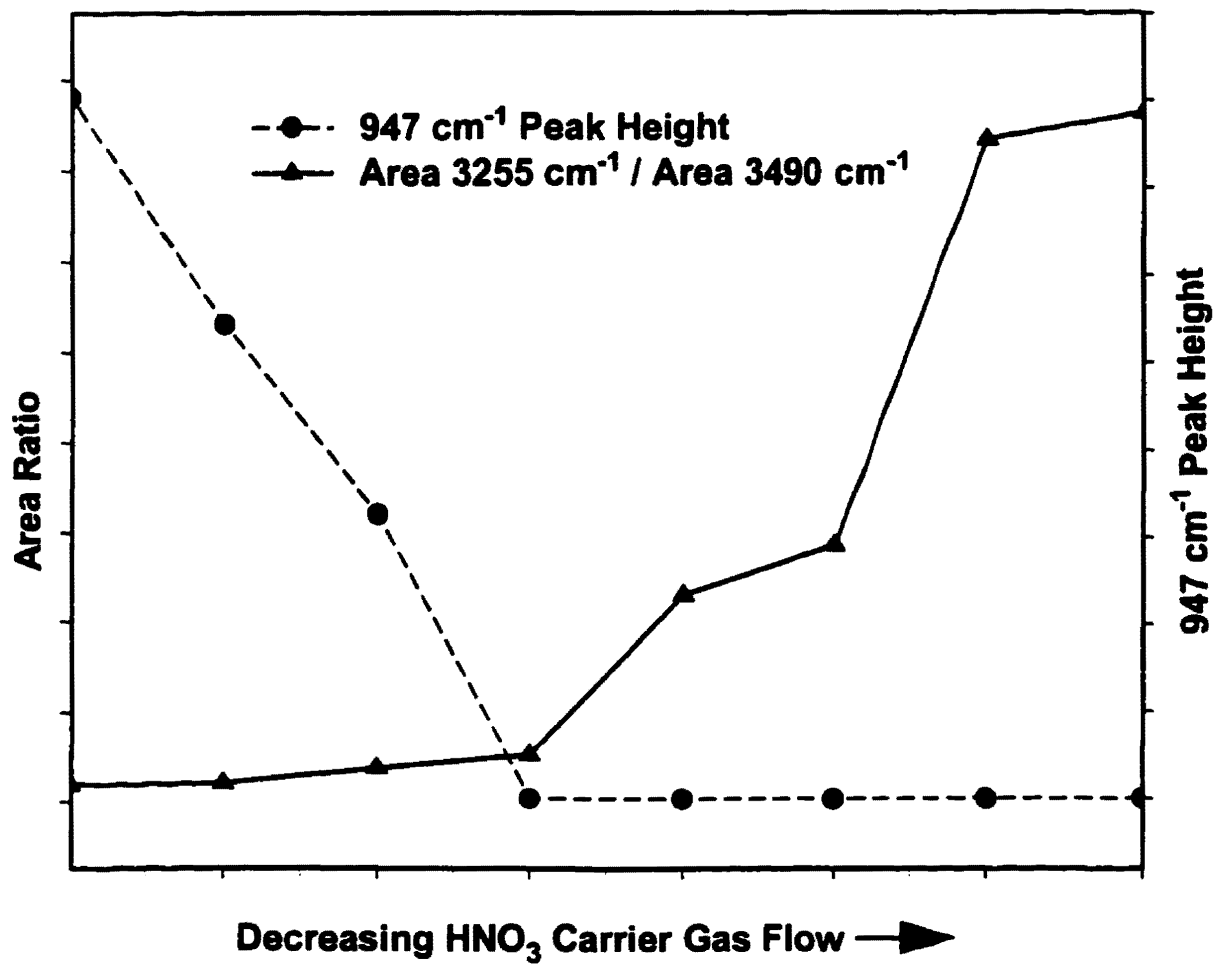


Figure 5.5 Plot used to establish the flows which produced a 2:1 $\text{H}_2\text{O}:\text{HNO}_3$ aerosol in the flow tube.

5.2.2 Results

As demonstrated above, liquid particles with a composition of 2:1 completely crystallize to nitric acid dihydrate when the temperature of the final section is held at 173 K. At temperatures above 179 K, however, the particles remain completely liquid. This was determined by comparing the aerosol spectrum with published spectra of nitric acid-water solutions.^{75,79} A series of absorbance spectra that encompass the transition from liquid to solid are shown in figure 5.6. The spectra are displaced vertically for clarity, but are plotted on the same vertical scale. The sharp features characteristic of crystalline NAD are evident in the top (low temperature) spectrum at frequencies of 3490, 3255 and 1030 cm^{-1} , and the broad features characteristic of liquid $\text{HNO}_3\text{-H}_2\text{O}$ are evident in the bottom spectrum.^{75,79} The intermediate spectra show features from both NAD and liquid $\text{HNO}_3\text{-H}_2\text{O}$. The most extensive changes occur in the OH region between 3100 cm^{-1} and 3650 cm^{-1} during freezing, so this spectral range was chosen to determine the NAD freezing point (the temperature where NAD first appears in the IR spectrum). Figure 5.7 is an enlarged view of this region. It shows seven spectra which were recorded at temperatures differing by about 1 K, and normalized at 3490 cm^{-1} in order to eliminate the effects of small fluctuations (less than 5%) in the number of particles in the observation region. The extreme pairs of curves at the top and bottom each consist of two spectra which are nearly indistinguishable at the vertical magnification of this figure. The top two are both spectra of the liquid. Their identical shape and intensity show that the liquid spectra are not temperature dependent near the NAD freezing point. The next lower spectrum shows the 3490 cm^{-1} and 3255 cm^{-1} OH features in NAD beginning to be distinguishable from the neighbouring broad OH band. As the temperature decreases (going downwards in the figure) the relative intensities of the OH absorption from liquid $\text{HNO}_3\text{-H}_2\text{O}$ diminish and the NAD OH features become more prominent. In the bottom two spectra, again indistinguishable at this magnification, the freezing process has been completed and the spectra (now of crystalline NAD) are once again temperature independent.

Several methods were examined to find the most accurate way of quantify the NAD freezing temperature. The shapes of the bands change substantially on freezing. The liquid spectrum is smooth and monotonic, while the solid has sharper features. The method we

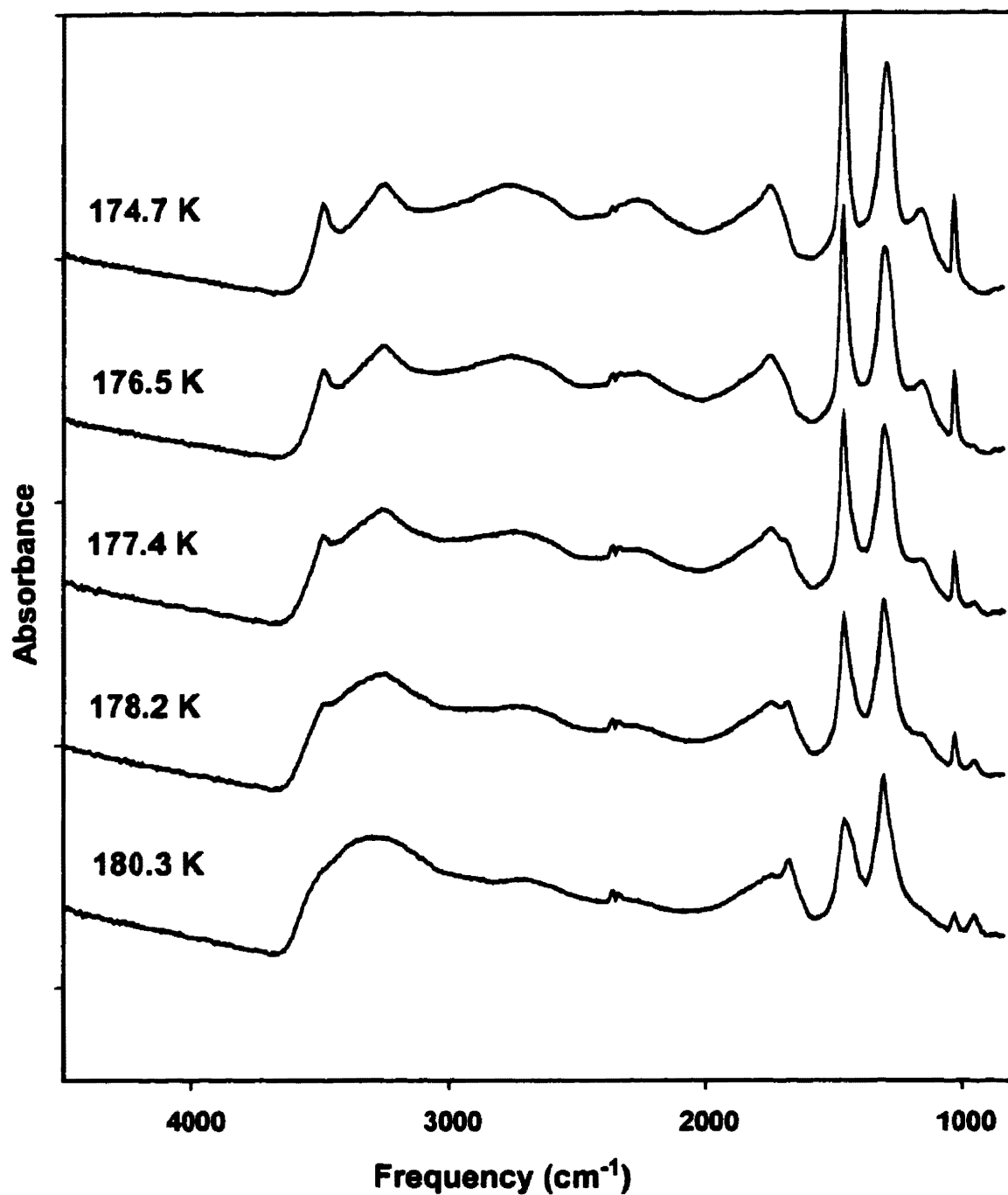


Figure 5.6 Change in the absorbance spectrum of a 2:1 H₂O:HNO₃ aerosol upon freezing. The bottom spectrum is completely liquid, the top is completely solid. Freezing begins near 179 K. The spectra have been offset in the vertical direction.

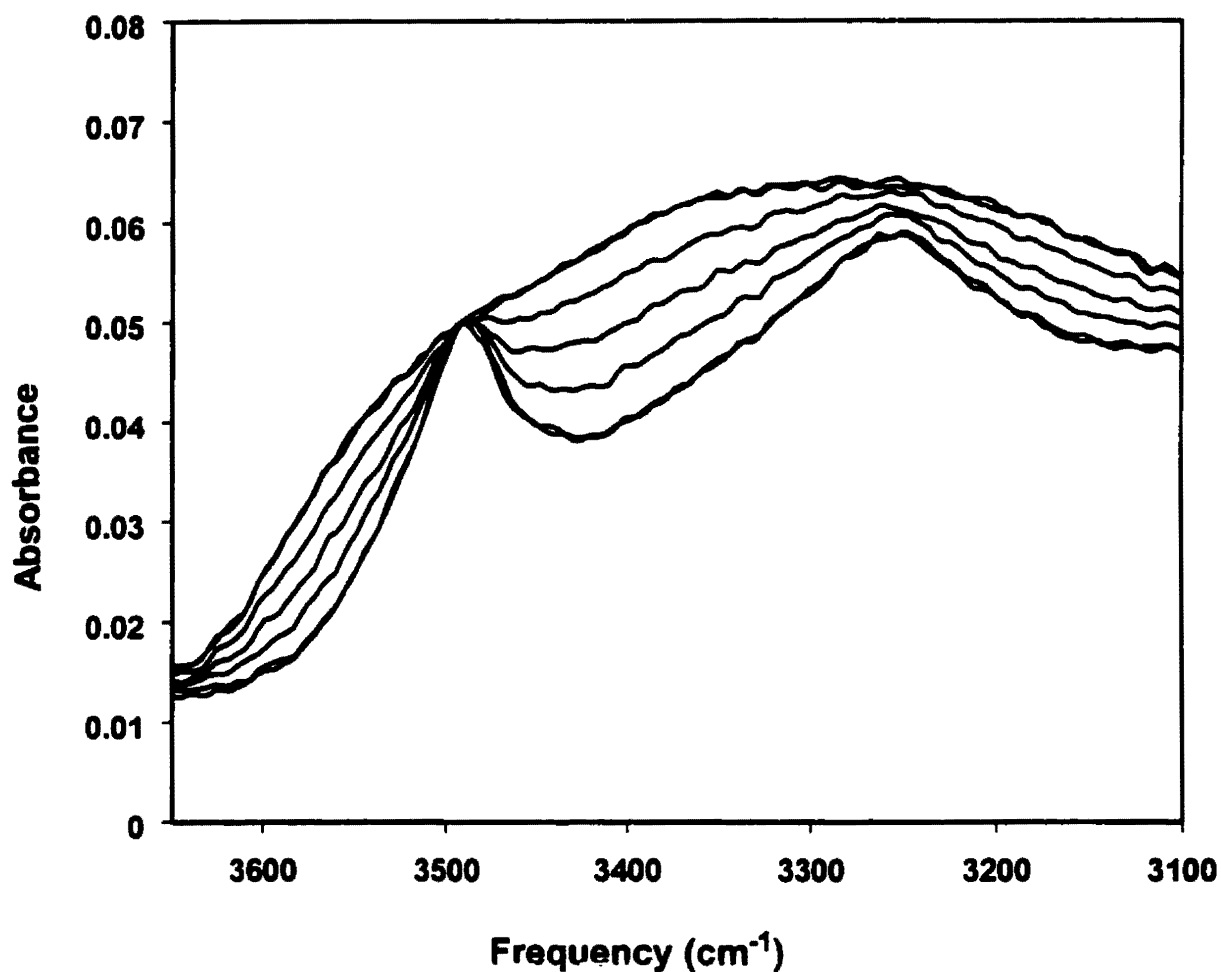


Figure 5.7 An enlarged view of seven spectra chosen for the freezing point measurement of NAD. The spectra were recorded at temperatures differing by about 1 K, over a range which includes the freezing of the aerosol. The top and bottom curves each show two pairs of spectra (liquid and solid, respectively) which are nearly indistinguishable at this magnification.

finally chose involved determining the difference between each spectrum and a reference spectrum. A liquid spectrum recorded within a few degrees of the freezing point was chosen as the reference and the differences between this and the other spectra were calculated in the frequency range shown in Figure 5.7 (3100 cm^{-1} to 3650 cm^{-1}). As a further test, the same procedure was repeated for several other spectral regions. The results from all regions were the same, but the region from 3100 cm^{-1} to 3650 cm^{-1} was chosen for the final measurement because it had the best signal to noise.

The differences between the reference spectrum and the spectra at the indicated temperatures, normalized such that the largest difference is 1.0, are shown in Figure 5.8. The points represent experimental measurements; the solid lines are described below. The values between 181.8 K and 179.6 K are indistinguishable from zero at the 2σ confidence level, consistent with the fact that the liquid spectrum does not vary over this small temperature range. The solid line through these four points is a least squares regression line; the dashed lines above and below this show the locations of the 2σ values. The freezing point is defined as the temperature at which the difference changes from zero by a distinguishable amount (greater than 2σ). This occurs between the data points at 179.6 K and 178.8 K, so the onset of freezing is assigned the value $179.2 \pm 0.4\text{ K}$.

The measured differences increase between 178.8 K and 174.7 K. At the latter temperature, the spectrum is that of crystalline NAD. Below 174.7 K, this spectrum also remains invariant with temperature at the 2σ level down to 171 K. The changes between the onset of freezing at 179.2 K and its completion at 174.7 K reflect the increase in the fraction of the aerosol volume that has crystallized. If the final section of the flow tube is cooled below the glass temperature (161 K^{72}), the amorphous phase is formed. As this section is allowed to warm, the amorphous phase continues to be observed up to about 163 K, and a mixture of the amorphous phase and the crystalline phase is observed up to about 168 K. Above this temperature, the spectrum is that of crystalline NAD. The appearance of the amorphous phase at temperature below 168 K is the result of either a small crystal growth rate or a small nucleation rate (see section 2.4 for a further discussion on this).

The information in Figure 5.8 can be used to derive the homogeneous nucleation rate (J) for the formation of NAD critical nuclei in 2:1 solutions. (Recall that J values

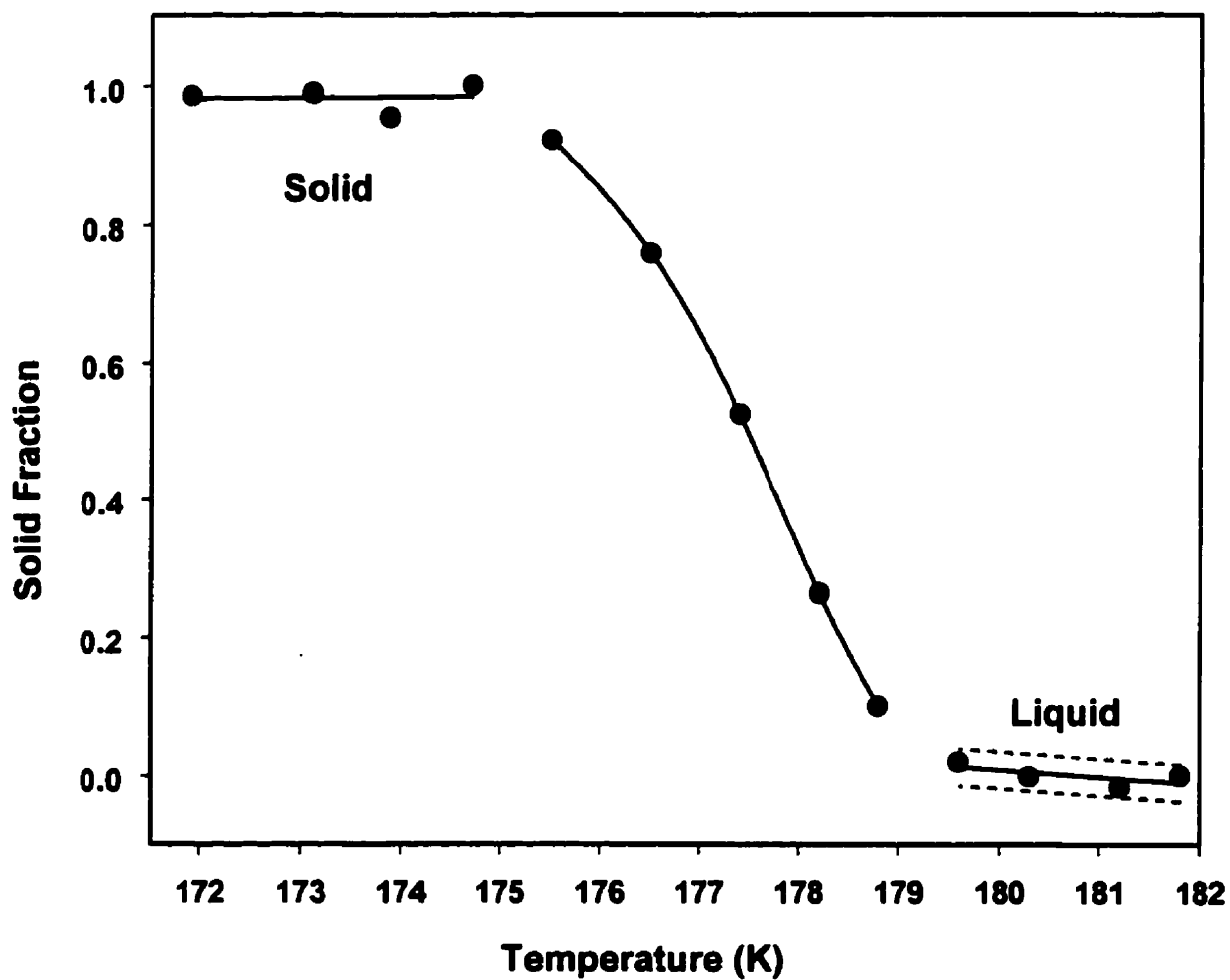


Figure 5.8 Change in the OH region (3650 to 3100 cm^{-1}) of the 2:1 spectrum as a function of temperature. The maximum change has been normalized to 1.

were determined for sulfate solutions using similar results.) To obtain a nucleation rate from this result, it is necessary to assume that crystallization is rapid with respect to the residence time. At temperatures ranging from 175 K to 171 K the liquid particles completely crystallize (see figure 5.8), so crystal growth is fast with respect to the residence time over this temperature range. At temperatures between 175 K and 182 K the crystal growth rate must also be fast because the crystal growth rate increases with temperature between 171 K and 182 K.⁸⁰ Consequently, the assumption of rapid crystallization is valid for the freezing temperatures we investigated. It is worth noting that crystallization is expected to be particularly fast for this system because the liquid has precise 2:1 stoichiometry (see section 2.3 for a further discussion on this).

As discussed in section 4.5, the equation that relates the homogeneous nucleation rate to the fraction of the aerosol volume that has frozen is

$$F_V(r, T) = \frac{f(r)V(r)(1 - \exp\{-J(T)V(r)\Delta t\})}{V_0} \quad (5.1)$$

where Δt is the residence time in the final section of the flow tube. Based on the flow rates and pressures in this experiment, Δt is 15 ± 1 seconds. The difference values plotted in Figure 5.8 yield a direct measurement of the volume fraction of droplets frozen at each temperature. Thus, if the size distribution function $f(r)$ is known, the nucleation rate constant can be obtained from equation 5.1.

The method we use to determining the size of our aerosol particles was described in section 3.4 and discussed further in section 4.3. In the present case, NAD optical constants from reference 78 were used in the Mie calculations. These have some slight inaccuracies when applied to aerosols at spectral frequencies below about 1250 cm^{-1} , so this region of the spectrum was excluded from the comparison. Spectra were calculated for a matrix of log-normal parameters r_g and σ_g spanning the following range: $r_g = 0.01$ to $0.41 \text{ }\mu\text{m}$ and $\sigma_g = 1.0$ to 2.1 , in steps of 0.01 for each parameter. Figure 5.9 shows a contour plot that was generated from this matrix of parameters (see section 3.4 for further discussion on this). The minimum runs diagonally from upper left to lower right in the plot, and along

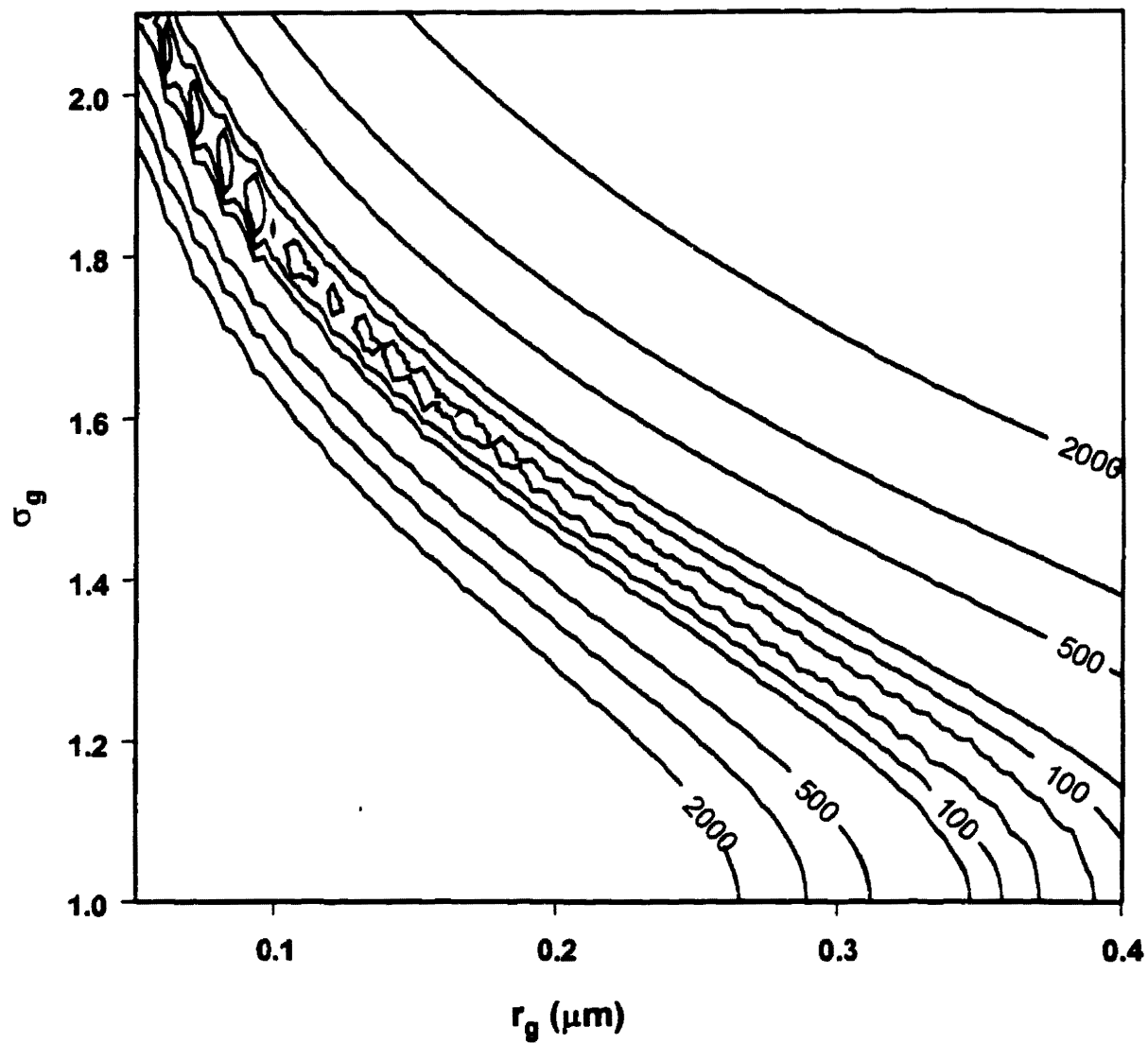


Figure 5.9 Contour plot generated by comparing a measured NAD spectrum with calculated spectra of particles having the log-normal size parameters indicated.

the minimum the values are nearly equal. This trend was also observed in the sulfuric acid experiments. A unique solution is not obtainable from a contour plot with this type of topology (see section 4.3); nevertheless, it is possible to estimate limits from the contour shape. From figure 5.9, we estimate upper limits of $r_g = 0.17 \mu\text{m}$ and $\sigma_g = 1.6$ and lower limits of $r_g = 0.38 \mu\text{m}$ and $\sigma_g = 1.0$ (the latter corresponds to a monodisperse aerosol). Shown in figure 5.10, is the calculated spectrum that corresponds to the lower limits of these log-normal size parameters ($r_g = 0.38 \mu\text{m}$ and $\sigma_g = 1.0$), as well as the experimental spectrum that was used to generate the contour plot.

The values of the nucleation rate constant, $J(T)$, obtained from equation 5.1, are shown in Table 5.1 for three temperatures, and 5 combinations of r_g and σ_g taken along the minimum in Figure 5.9. The temperatures were obtained from the data in Figure 5.8, and correspond to values of the volume fraction frozen, $F_V(r, T)$, equal to 0.1, 0.5 and 0.9.

Table 5.1 Nucleation rate constant, $J(T)$, as a function of temperature and log-normal size distribution. All values are in units of $10^{12} \text{ cm}^{-3} \text{ s}^{-1}$.

Temperature (K) ; $F_V(r, T)$	178.8 ; 0.1	177.5 ; 0.5	175.8 ; 0.9
$\langle r \rangle = 0.38 \mu\text{m}$, $\sigma = 1.001$	0.031	0.20	0.67
$\langle r \rangle = 0.37 \mu\text{m}$, $\sigma = 1.101$	0.029	0.20	0.70
$\langle r \rangle = 0.34 \mu\text{m}$, $\sigma = 1.201$	0.028	0.20	0.83
$\langle r \rangle = 0.25 \mu\text{m}$, $\sigma = 1.401$	0.024	0.22	1.46
$\langle r \rangle = 0.17 \mu\text{m}$, $\sigma = 1.601$	0.021	0.26	2.52

5.2.3 Discussion

Our data indicate that homogeneous nucleation of NAD from liquid aerosol droplets occurs at relatively low temperatures. We observe a flowing aerosol having an average

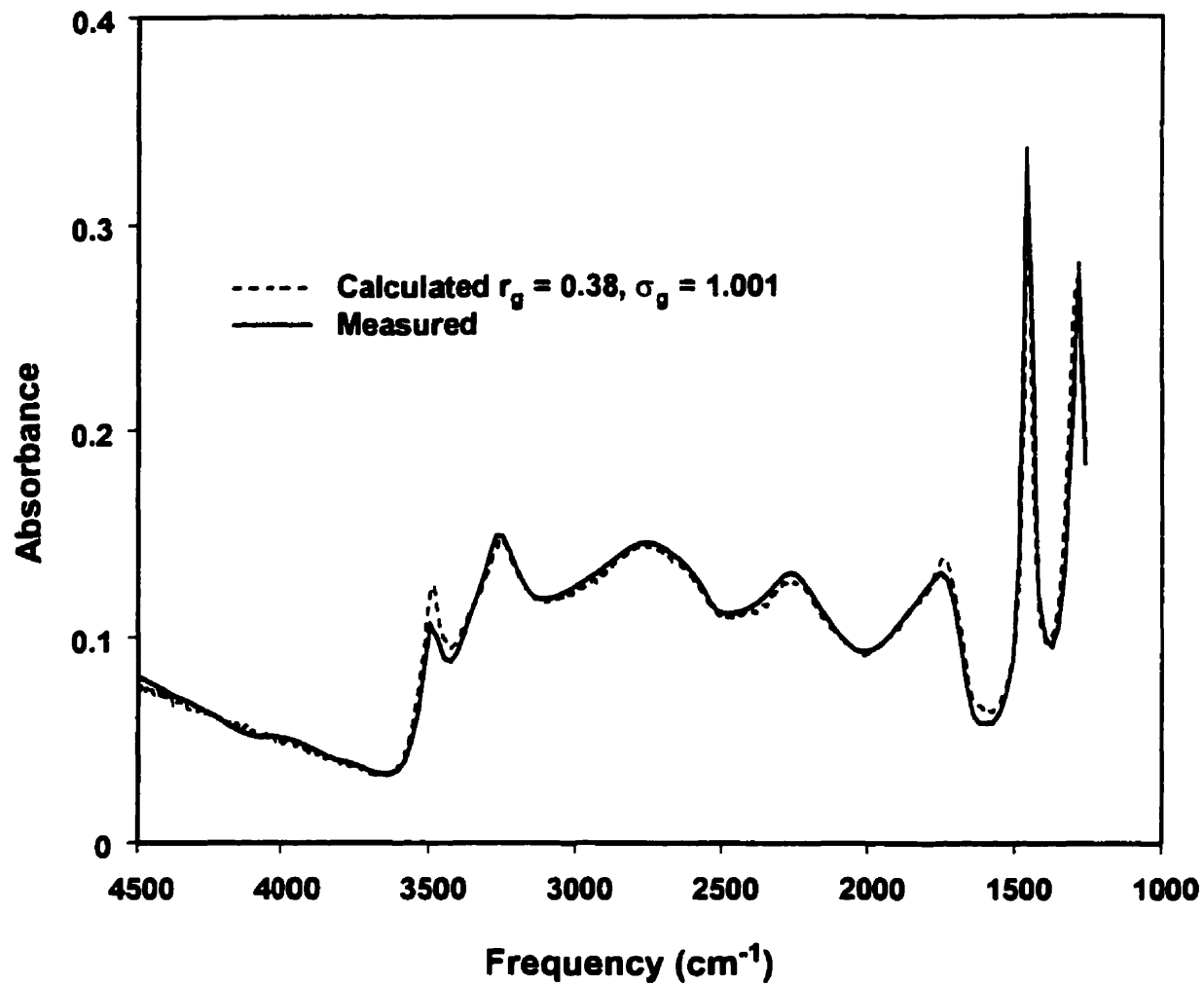


Figure 5.10 Comparison of measured NAD aerosol spectrum with a calculated spectrum having the log-normal parameters indicated.

radius of approximately 0.4 μm , after it has spent approximately 15 seconds at a known temperature. On this time scale, the temperature for the onset of nucleation is between 179.6 K and 178.8 K. As we reduce the temperature of the observation section, we find that 10% of the sample has frozen after 15 seconds at a temperature of 178.8 K, 50% has frozen at 177.5 K and 90% at 175.8 K. These results indicate that $J(T)$ increases with decreasing temperature in the range between 180 K and 175 K. At lower temperatures, especially nearing the glass temperature, the viscosity becomes high, and $J(T)$ is expected to decrease with decreasing temperature.

Homogeneous nucleation rates of NAD have been previously reported in the literature. These rates, as well as our measured rates, are displayed in figure 5.11. Our data are represented by the triangles. The horizontal error bars represent the maximum uncertainty in the absolute temperature (± 1.6 K) from all sources, and the vertical error bars reflect uncertainties in the residence time and the size distribution. The vertical error bars associated with the lower two rates are smaller than the data points.

The hatched region in figure 5.11 shows results from Barton *et al.*⁷⁹ Using a static aerosol chamber, these authors observed rapid crystallization (<1 minute) of 2:1 droplets at temperatures within a few degrees of 173 K. From this information and their estimated particle size (< 1 micron), we calculated limits for $J(T)$ that correspond to their results. The hatched region in figure 5.11 represents these limits. Our results agree with these limits to well within our quoted uncertainty of ± 1.6 K.

The squares in figure 5.11, which are connected by line segments for clarity, show results from Mackenzie *et al.*⁶⁵ These rates were calculated using the “Turnbull correlation”, an approximation to classical nucleation theory. The temperature dependence of our measured $J(T)$ values are in excellent agreement with that predicted by the calculations, although the absolute values of the temperatures are uniformly between three and four Kelvin below those of the MacKenzie work, for equivalent $J(T)$ values.

The circles in figure 5.11 show results from Disselkamp *et al.*⁸¹ These rates were measured using a similar technique to that employed by Barton *et al.* The solid line that connects the Disselkamp *et al.* data is the result of a calculation by Tisdale *et al.*⁸⁰ The

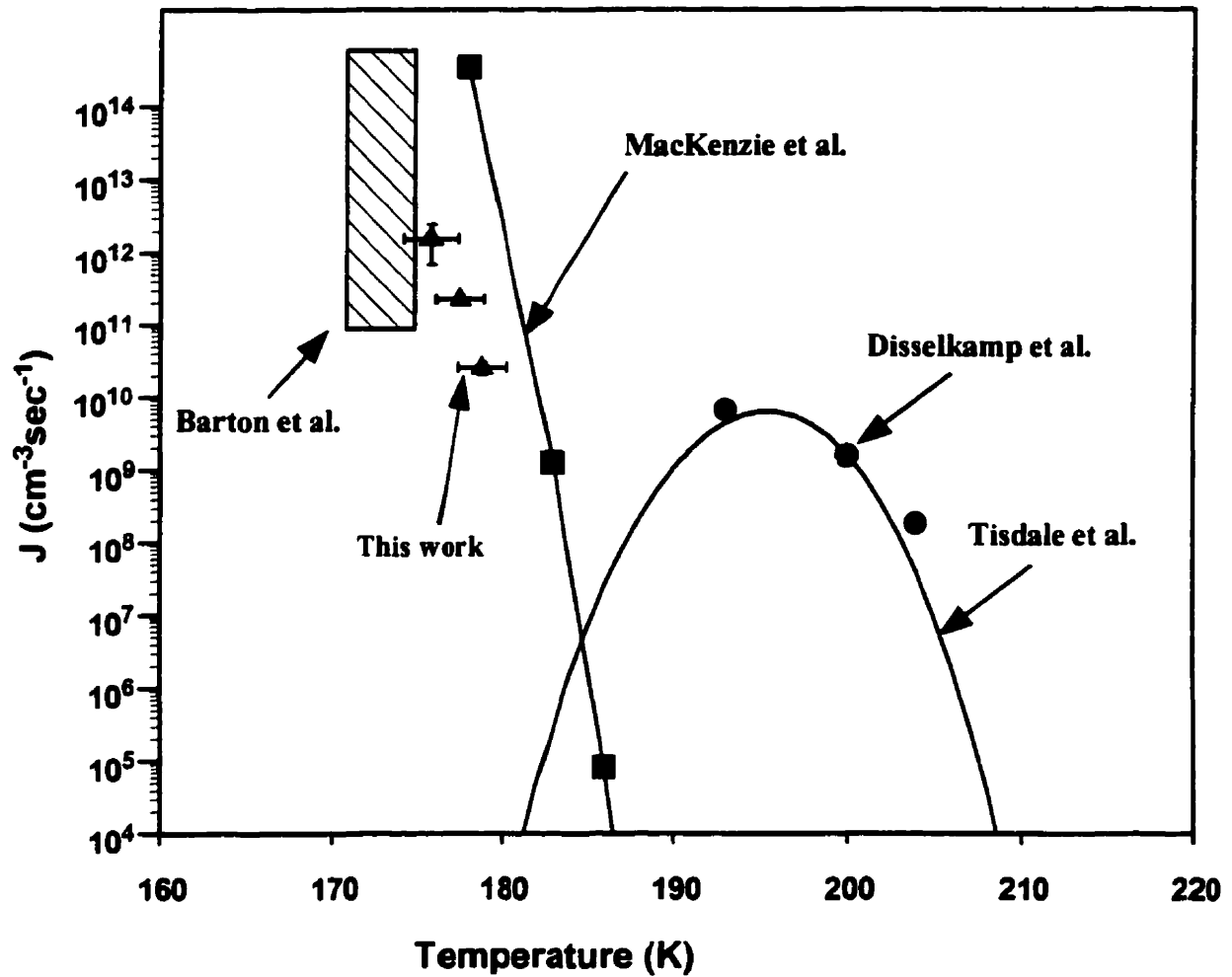


Figure 5.11 Comparison of the nucleation rates of NAD derived from the measurements reported here (triangles) with values which have been calculated (squares and lines) and measured (circles and hatched region).

calculation was based on classical nucleation theory and was constrained to the rates reported by Disselkamp *et al.* Our nucleation rates do not agree with those reported by Disselkamp *et al.* and Tisdale *et al.* As shown in figure 5.11, Disselkamp *et al.* reported nucleation rates on the order of $10^9 \text{ cm}^{-3} \text{ s}^{-1}$ at temperatures about 20 K higher than our results would indicate. Also, the curve reported by Tisdale *et al.* indicate that $J(T)$ decreases to values below $10^4 \text{ cm}^{-3} \text{ s}^{-1}$ at temperatures below 180 K, yet we measured rates above $10^{12} \text{ cm}^{-3} \text{ s}^{-1}$ at these temperatures.

Meilinger *et al.* and Tsias *et al.* predicted that liquid ternary PSCs can become essential binary nitric acid-water aerosols under certain conditions. These authors also speculated that the binary aerosols would freeze as either NAD or NAT at polar stratospheric temperatures. For 1 % of these small particles ($r=0.2 \mu\text{m}$) to freeze in 5 minutes (typical time of a rapid temperature fluctuation), the homogeneous nucleation rate must be $1 \times 10^9 \text{ cm}^{-3} \text{ sec}^{-1}$. If our J 's are extrapolated to this value, corresponding temperatures of 182 K to 185 K are obtained. Although very low, these temperatures are occasionally reached during the Antarctic winter. In the warmer Arctic region, however, temperatures usually remain a few degrees above these values.⁸² Furthermore, at temperatures below approximately 185 K, the precipitation of ice is believed to be the dominant freezing mechanism.

Finally, it should be emphasized that the above discussion refers to the homogeneous nucleation of NAD from $\text{HNO}_3\text{-H}_2\text{O}$ solutions having exactly 2:1 stoichiometry. It is not expected on the basis of current models that nitric acid aerosols in the stratosphere would reach this composition. Meilinger *et al.* and Tsias *et al.* predicted concentrations ranging from 52 wt % HNO_3 to 58 wt % HNO_3 , whereas a 2:1 composition corresponds to 64 wt % HNO_3 . Nevertheless, ideas on the stratospheric aerosol composition are still evolving; therefore, it is desirable to have freezing data for a wide range of compositions extending beyond those presently expected in nature.

5.3 NITRIC ACID TRIHYDRATE AEROSOLS

The second set of nitric acid-water experiments were performed on aerosols with a stoichiometric 3:1 composition (54 wt % acid). This composition is within the range

predicted by Meilinger *et al.* and Tsias *et al.* (52-58 wt % acid). The 3:1 freezing experiments were very similar to the 2:1 freezing experiments, except for the temperature profile in the flow tube. It was necessary to cycle the temperature of the 3:1 aerosol to obtain complete crystallization to NAT (see below). Using this method, we determined homogeneous nucleation rates for the NAT freezing process.

5.3.1 Experiment

The same cryogenic flow tube and associated apparatus used in the 2:1 aerosol experiments were also used in the 3:1 experiments (see section 5.2.1 for a further description of this set-up). The technique of composition determination also was very similar in both experiments. The procedure for 3:1 determination is outlined below.

Features characteristic of NAT appear in the experimental spectra over a wide range of vapor compositions, as illustrated in figure 5.12. The top three curves were recorded with the temperatures of the first, middle and last sections held at 188 K, 153 K, and 178 K, respectively. At these temperatures, all of the liquid aerosol particles that formed in the first section, nucleate stable crystalline embryos in the middle section, and these embryos grow rapidly in the last section before the observation area. This results in complete crystallization of the aerosol particles. (The temperature cycling technique that gives these results is discussed in greater detail below.) The concentrations of the aerosols that correspond to the top three spectra in figure 5.12 are less than, approximately equal to and greater than 3:1, respectively. The bottom curve is a Mie-theory calculation of the spectrum of pure NAT, calculated with the optical constants reported in reference 83. Clearly, all of the measured spectra contain substantial contributions from crystalline NAT, and thus, it is not possible to determine by visual inspection the flows that give NAT, a precise 3:1 aerosol.

The carrier gas flow rates that gave NAT were obtained by plotting the intensities of relevant spectral features as a function of the ratio of the H₂O and HNO₃ flows. In practice, the HNO₃ flow is kept constant, so intensities were plotted as a function of H₂O flow. Figure 5.13 shows one of these plots. The 3430 cm⁻¹ and 3215 cm⁻¹ bands are due to H₂O in different NAT crystal sites.^{15,75} In addition, these two bands can have contributions

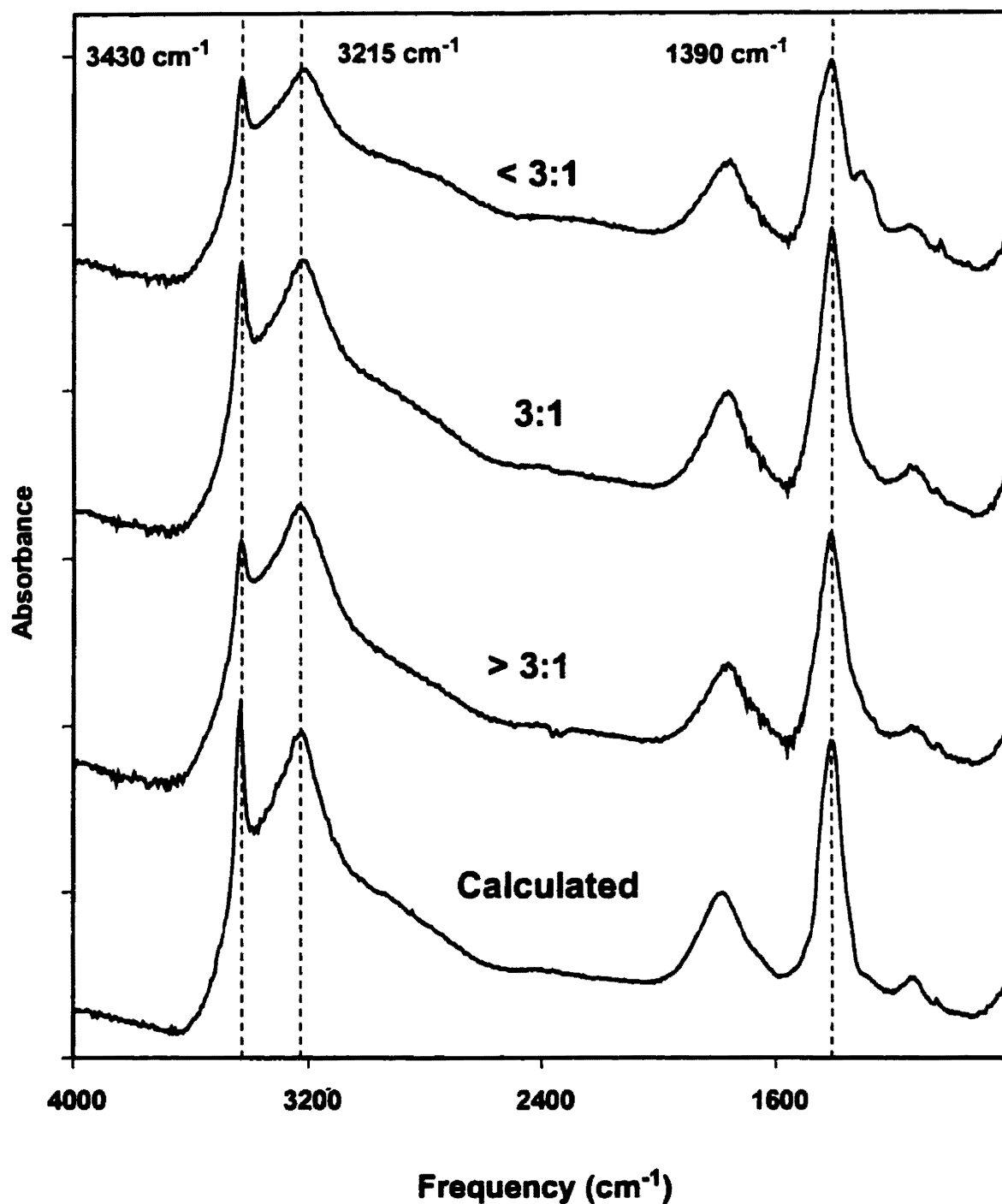


Figure 5.12 Low-temperature nitric acid trihydrate aerosol spectra. The top three curves are measured spectra, for which the HNO₃/H₂O ratio is less than, approximately equal to, and greater than 3. The bottom curve is a calculated spectrum. The spectra have been offset in the vertical direction.

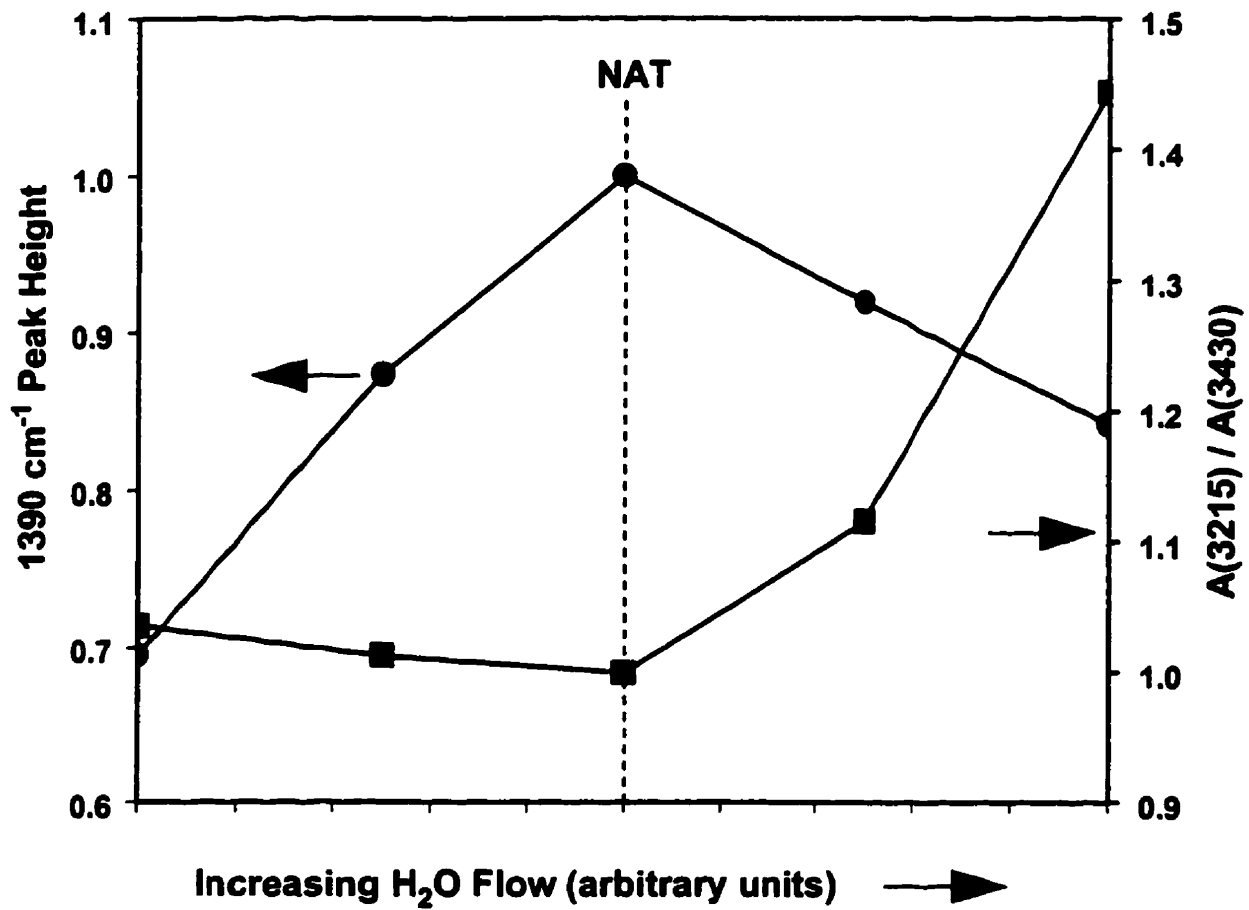


Figure 5.13 Plot used to establish the flows which produced a 3:1 aerosol in the flow tube.

from the OH absorption of liquid $\text{HNO}_3\text{-H}_2\text{O}$, which stretches from 2600 cm^{-1} to 3600 cm^{-1} . The ratio of the areas of the 3430 cm^{-1} and 3215 cm^{-1} bands gives a measure of the NAT:liquid ratio because the 3215 cm^{-1} band is near the maximum of the liquid absorption, while the 3430 cm^{-1} band is near its edge. Consequently, the area ratio $A(3215)/A(3430)$ will be a minimum when the aerosol particle is completely NAT. The intensity of the 1390 cm^{-1} band corresponds to the $\text{NO}_3(\nu_3)$ singlet band of NAT.¹⁵ This band is a maximum at the same flow that the $A(3215)/A(3430)$ is a minimum, indicating that this flow ratio yields the 3:1 NAT composition. The uncertainty associated with the flow rates and the integrations leads to a total uncertainty in the composition of $\pm 0.05:1$ (moles H_2O :moles HNO_3).

Critical nuclei are too small to be measured by FTIR extinction spectroscopy, so nucleation is detected by ensuring that the critical nuclei grow to an observable size during the observation time of the experiment. Complete crystallization of the aerosol particle is preferred, because this gives the maximum signal for a nucleation event. The temperature profile used to achieve this depends on the magnitudes and overlap of the nucleation rate and the crystal growth rate (see section 2.4). If the crystal growth rate and nucleation rate overlap for some temperature range and the crystal growth rate is appreciable (see figure 2.2a), then the dashed profile in Figure 5.14 will induce complete crystallization. (For the remainder of the thesis, this profile is referred to as the two-stage temperature profile.) In this case, the temperatures of the first two sections are held constant at a value that produces liquid droplets, and the temperature of the final section is varied. This temperature profile was used in the previous measurements of NAD nucleation.

Unlike NAD, however, NAT has a slow crystal growth rate near its nucleation temperature, so to detect NAT nucleation accurately, we used the temperature profile indicated by the solid line in Figure 5.14. (This profile is referred to as a three-stage temperature profile for the remainder of the thesis.) In this case, the temperatures of the first and third sections are held constant at 188 K and 178 K, respectively. The former causes condensation of liquid aerosol droplets from the gas phase, but produces no solid particles. The latter is too high to nucleate NAT in the liquid droplets, but causes rapid crystal growth in droplets that have been nucleated at the (lower) temperature of the middle

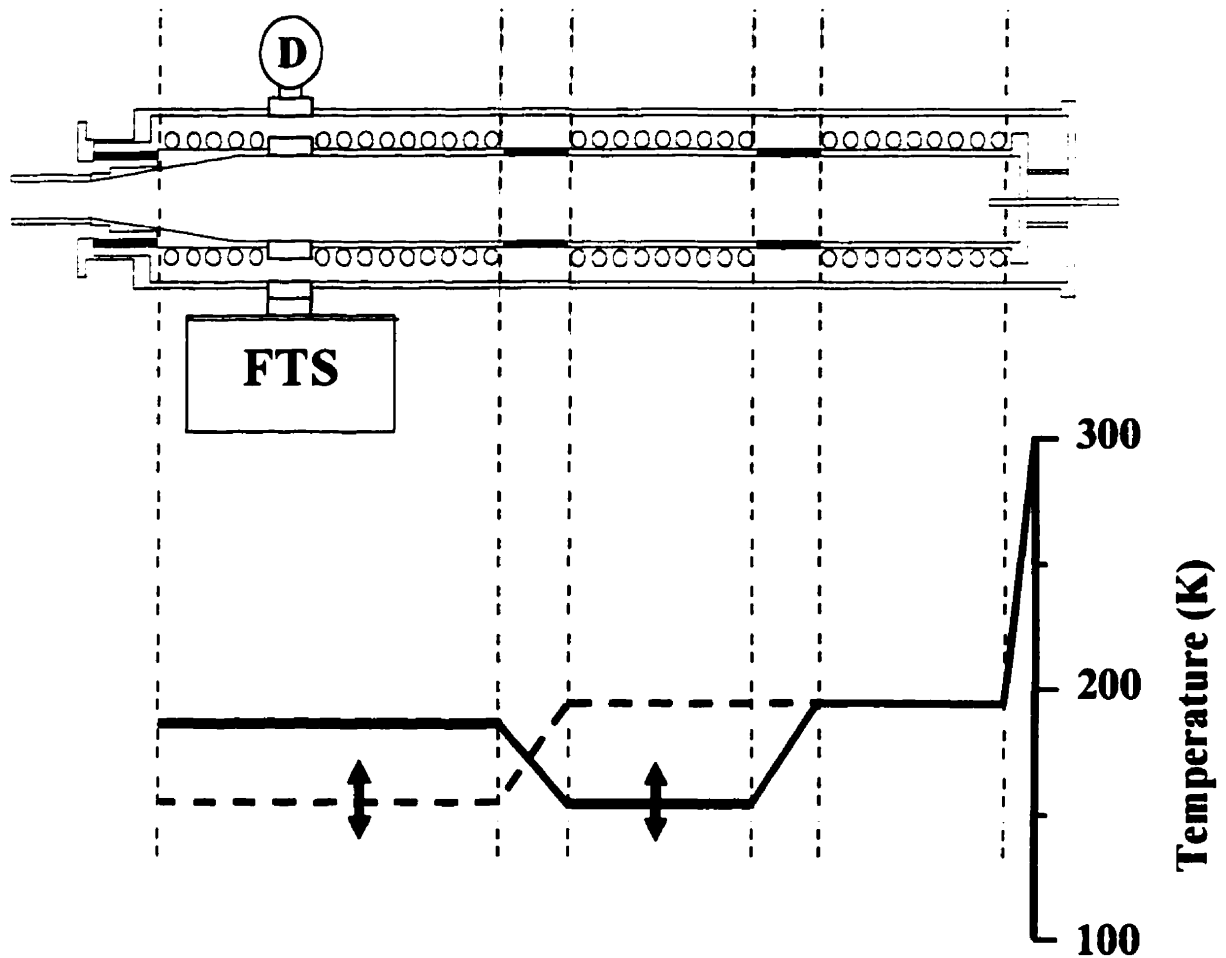


Figure 5.14 Schematic cross section of the flow tube is shown at the top of the figure. The temperature profiles used in the NAD and NAT experiments are at the bottom. The dashed line is the two-stage temperature profile; the solid line is the three-stage temperature profile.

section. (Only the spectra of the liquid aerosol droplets are seen if the temperature of the middle section is set at either 188K or 178 K.) When the temperature of the middle section is low enough, NAT begins to nucleate there (see below), and large crystals grow from these nuclei when the droplets move into the third section.

To do a 3:1 freezing experiment, we first set the temperatures of the first, second, and third section at 188, 153, and 178 K, respectively, and then flows are adjusted until the 3:1 composition is established. Finally, the temperature of the middle section is slowly raised, while infrared spectra are continuously recorded.

5.3.2 Results

Figure 5.15 shows a selection of spectra covering the range from 169.1 K to 159.1 K. At the upper end of this range, the H₂O absorption in the 3400 cm⁻¹ region is broad and continuous, indicating that the sample is completely liquid,^{75,79} whereas at 159.1 K, the characteristic sharp absorptions are clearly visible at 3430 cm⁻¹ and 3215 cm⁻¹, indicating the presence of solid NAT crystals.^{15,75,83} From these spectra, it is possible to quantify the fraction of the total aerosol volume that has frozen at a given temperature. The general procedure, which has been discussed in section 5.2, involves plotting the change in some feature of the spectrum versus temperature. As long as the particles remain liquid or solid, very little or no change is observed in the spectra. As the sample freezes, however, the feature (if chosen correctly) will change monotonically with the fraction of the sample that has crystallized.

Two spectral features were considered for this measurement: the integral over the H₂O absorptions in the NAT crystal (the frequency range from 3000 cm⁻¹ to 3600 cm⁻¹) and the integral over the NO₃ (ν₃) band near 1400 cm⁻¹. These gave the same results, with approximately the same signal to noise values; the latter was chosen for the final nucleation measurements. As can be seen in Figure 5.15, this band changes from a broad doublet in the liquid to a sharp single absorption located between about 1350 cm⁻¹ and 1450 cm⁻¹ when the sample changes from liquid droplets to NAT. The fraction of the total aerosol volume that has frozen is the change in the integral of this band, normalized such that the largest difference is 1.0. In Figure 5.16, this fraction is plotted against the temperature of

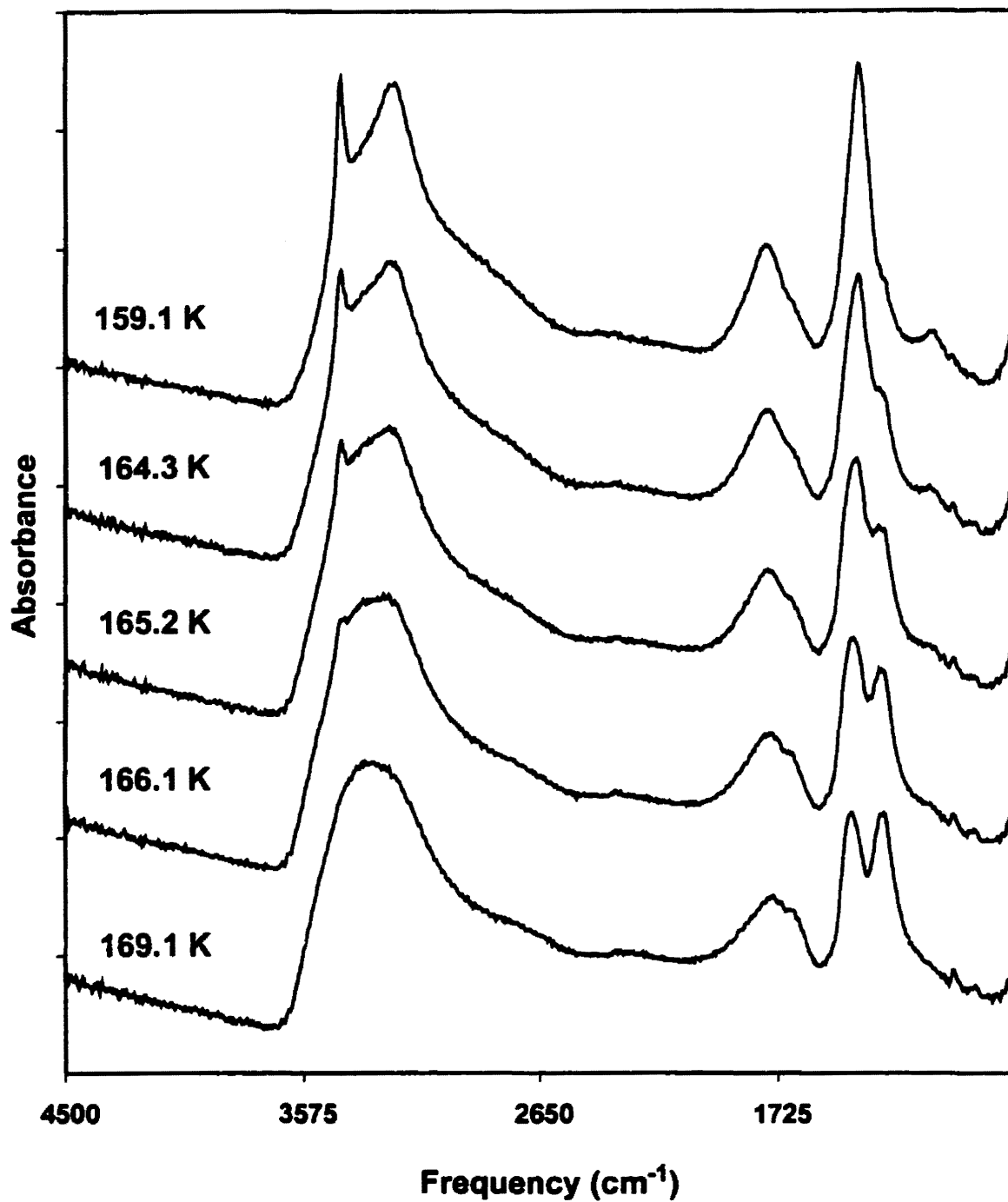


Figure 5.15 Changes in the absorbance spectra of a 3:1 aerosol upon freezing. The bottom spectrum is completely liquid; the top is completely solid. Freezing begins near 168 K. The spectra have been offset in the vertical direction.

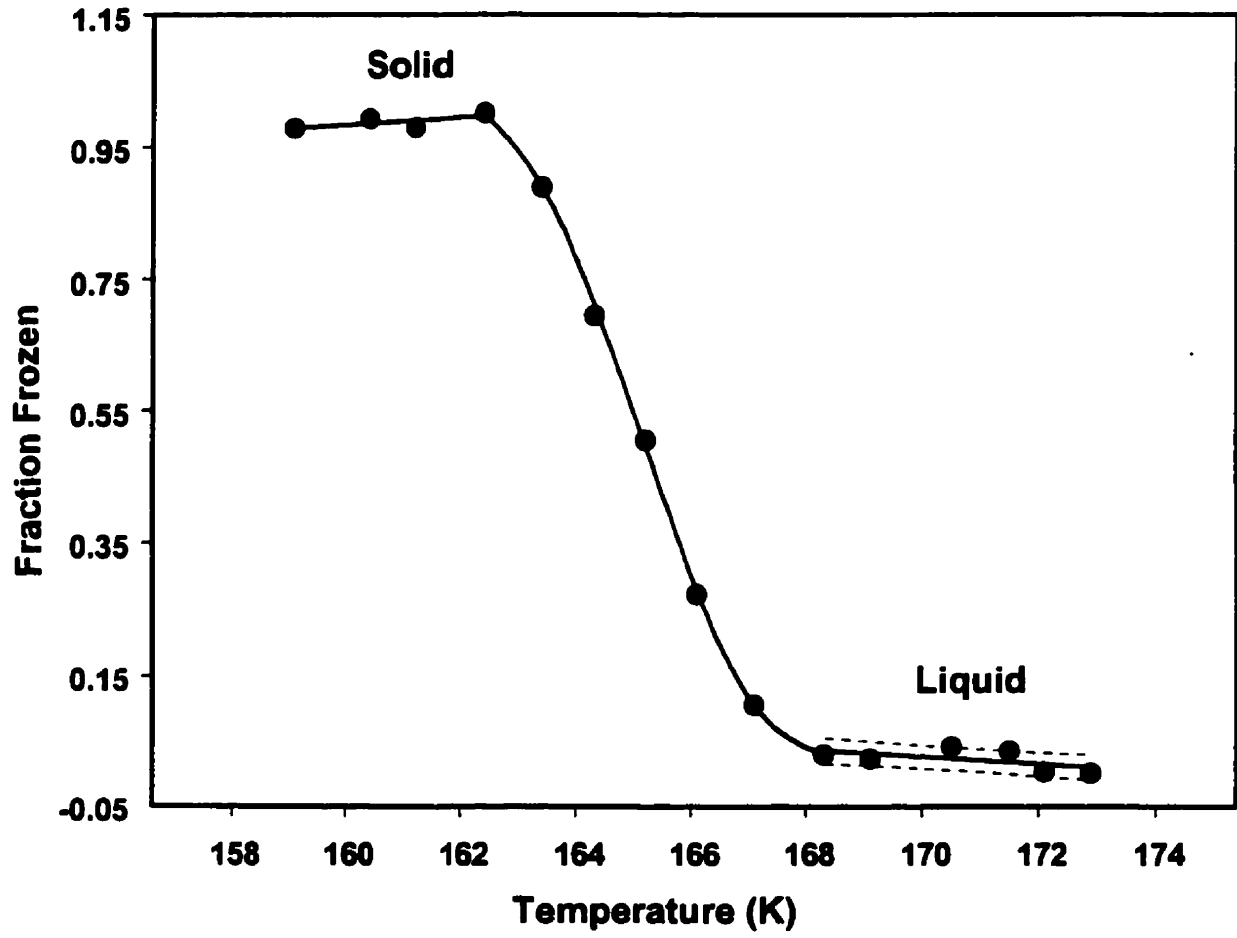


Figure 5.16 Change in the nitrate band of the 3:1 spectrum as a function of temperature. The maximum change has been normalized to 1.

the middle section. The dashed line shows the 2σ values for a linear regression to the data points from 172.9 K to 168.3 K. The fraction frozen becomes non-zero between 167 and 168 K, and rises smoothly until 162.4 K where it again becomes constant with decreasing temperature. Thereafter, no change in the spectra was observed down to 158 K.

Shown in figure 5.17 is the contour plot used to determine the log-normal size parameters of the 3:1 aerosols. This contour plot was generated by comparing an experimental spectrum of NAT with calculated spectra of NAT (see section 3.4 for a further discussion on the technique). The optical constants used to calculate the NAT spectra were taken from reference 83. From this contour plot, we conclude that the best fit to the experimental spectrum occurs for $r_g = 0.10 \mu\text{m}$ and $\sigma_g = 1.8$. We estimate an error associated with r_g of $\pm 0.05 \mu\text{m}$ and σ_g of ± 0.2 . This covers the entire range of the lowest contour in figure 5.17. Shown in figure 5.18 is the experimental spectrum of NAT that was used in these calculations, as well as the calculated spectrum that gave the best fit to the experimental data.

In the 3:1 experiments, the crystal growth rate was large because the temperature of the aerosol was increased to 178 K in the final section of the flow tube. As a result, the homogeneous nucleation rate is related to the volume fraction frozen (figure 5.16) through equation 5.1 (see section 5.2 for a further discussion). Using this equation, we calculated the following nucleation rates: (in units of $\text{cm}^{-3} \text{s}^{-1} \times 10^{11}$) 0.38 ± 0.18 , 7.4 ± 3.9 and 97 ± 63 at temperatures of 167.2 K, 165.2 K and 163.5 K respectively. These values were calculated for $F_V(r, T)$ equal to 0.1, 0.5 and 0.9. The quoted errors represent the combined effects of uncertainties in the size distribution and the residence time.

5.3.3 Discussion

The rate constants, $J(T)$, we determined from our data are shown as the square points in Figure 5.19. The error bars represent the uncertainty in the temperature (± 1.6 K), the residence time, and the size distribution parameters. The solid line to the right of these points shows the rates calculated for the nucleation of NAT from liquid aerosol droplets having a 3:1 stoichiometry.⁶⁵ Also shown in the Figure 5.19 (as triangular points) are the rates, which we reported in section 5.2.3 for the homogeneous nucleation of NAD from an

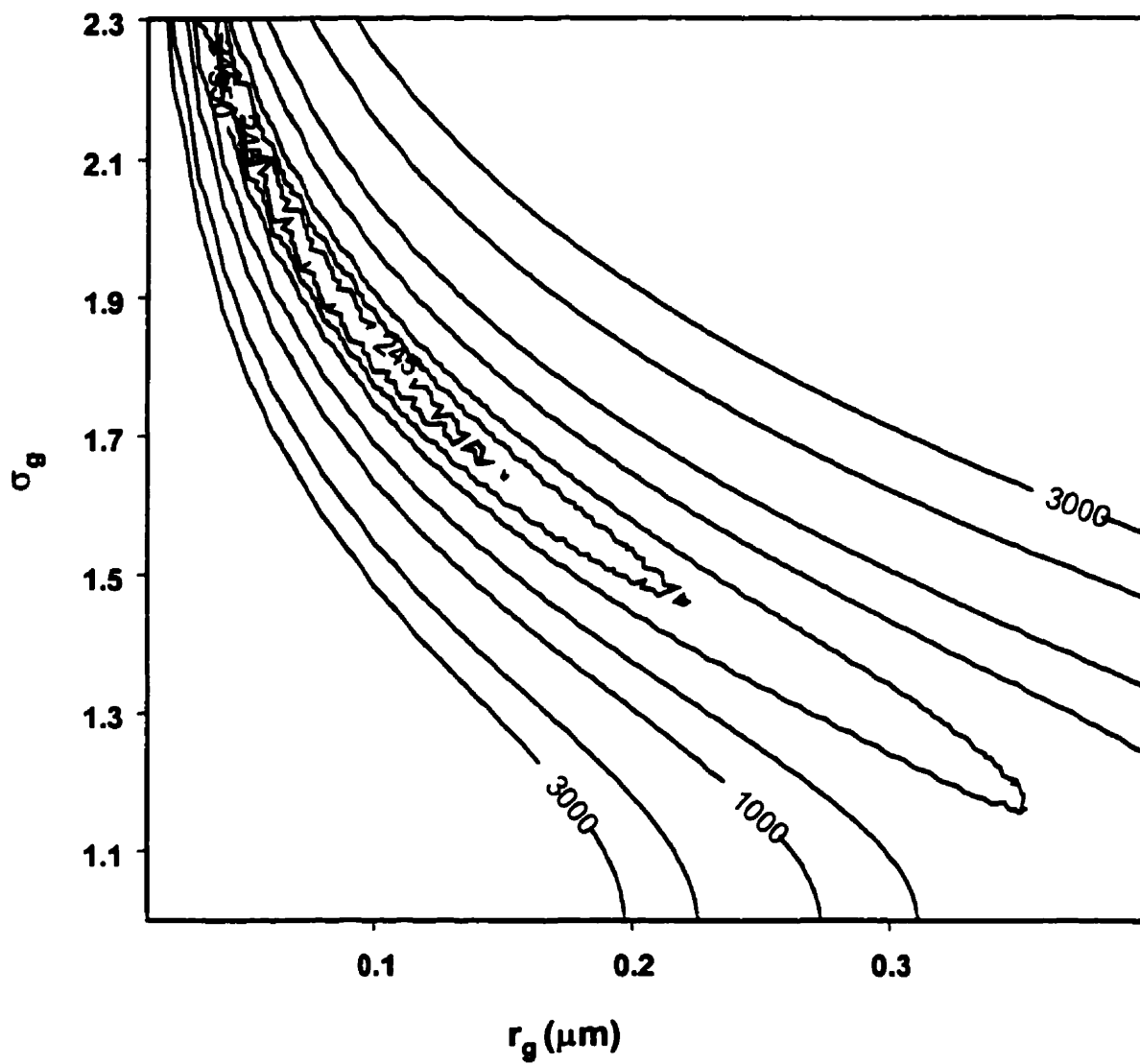


Figure 5.17 Contour plot generated by comparing a measured NAT spectrum with calculated spectra having the log-normal size parameters indicated.

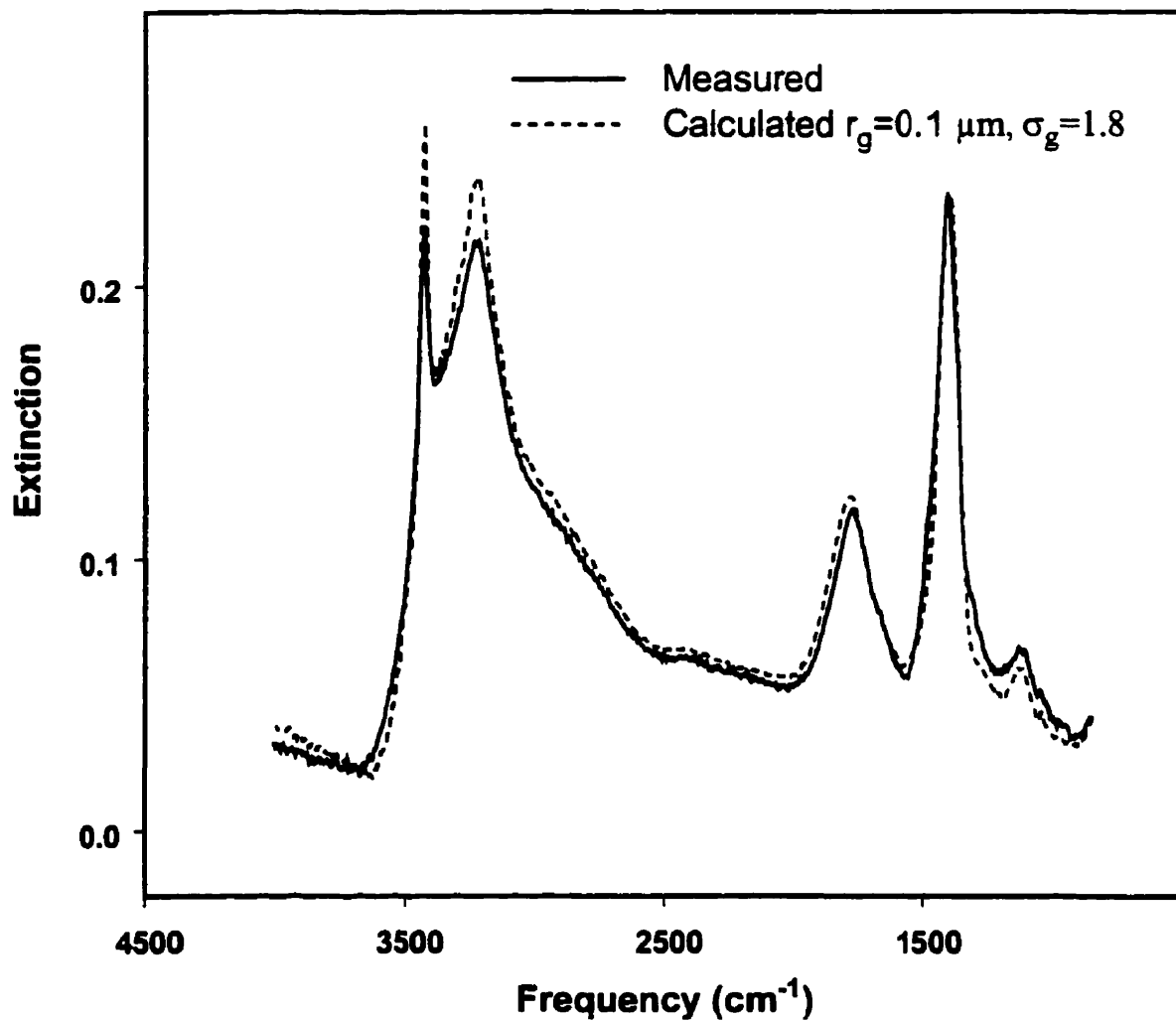


Figure 5.18 Comparison of a measured NAT aerosol spectrum with a calculated spectrum of NAT particles having the log-normal size parameters indicated.

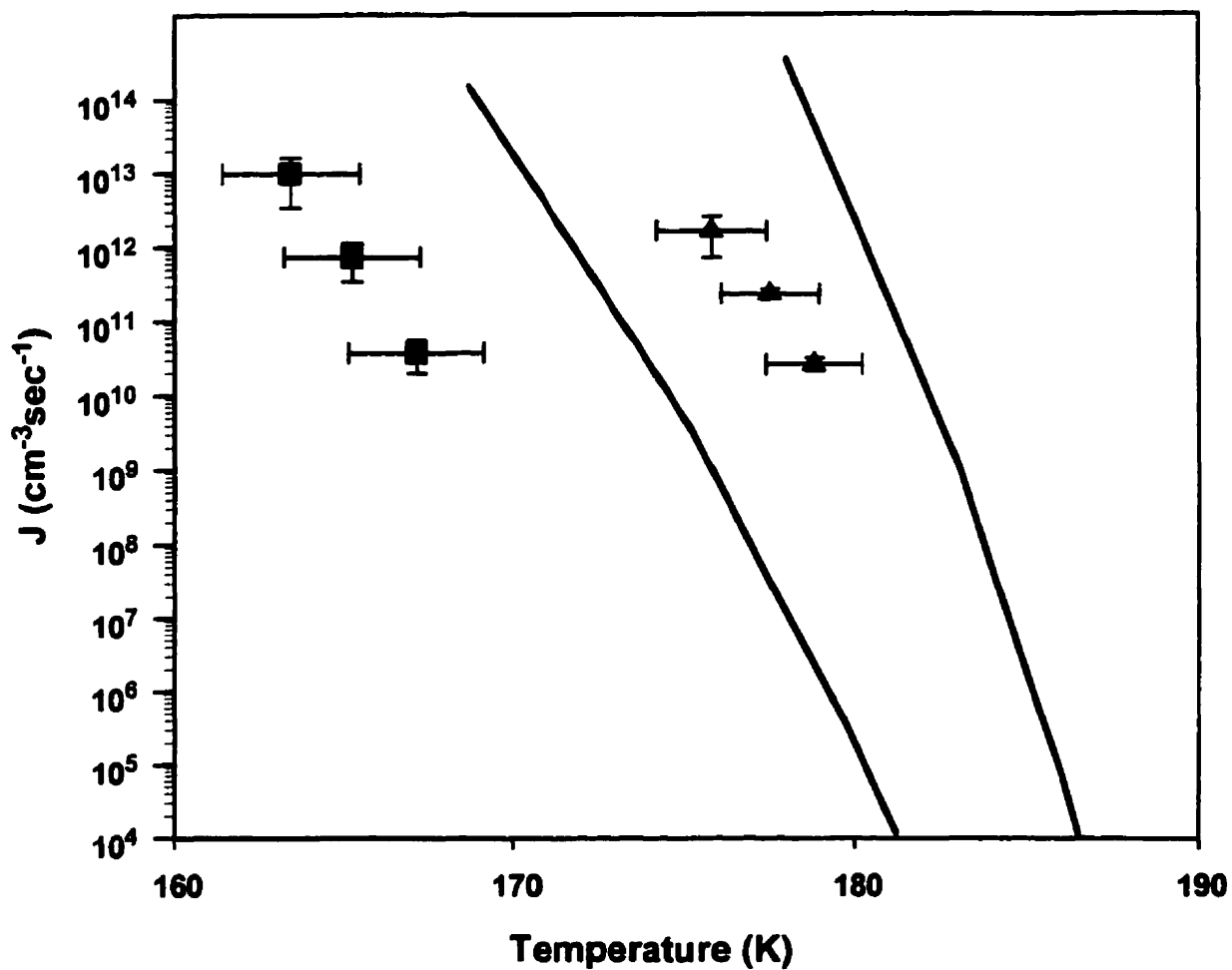


Figure 5.19 Comparison of the rate constants, $J(T)$, reported here for NAT nucleation in a 3:1 aerosol (squares) with the nucleation of NAD in a 2:1 aerosol (triangles). The lines to the right of each set of data points show the corresponding calculated rates.

aerosol having a 2:1 composition. The line to the right of these points shows the calculation by MacKenzie *et al.* for the corresponding NAD solution.⁶⁵ The agreement between the relative values of the experimental and calculated rates is very good, but for corresponding $J(T)$ values, the calculations are consistently about 3 - 8 K higher in temperature than the measurements. The relative values of the nucleation rates are also in agreement with the work of Worsnop *et al.*,¹⁶ which showed that the nucleation of NAD is favoured over nucleation of NAT.

Two other investigations of the homogenous freezing of 3:1 aerosols have been reported. Neither used temperature cycling; in both cases, the vapor was cooled to a low temperature in a single step, and the IR extinction spectrum of the resulting aerosol was monitored as a function of time. Disselkamp *et al.*⁸¹ found no crystallization of 3:1 nitric acid particles at temperatures down to 190 K. In contrast, Barton *et al.*⁷⁹ reported freezing of 3:1 aerosols at approximately 175 K. These authors monitored crystallization of sub-micron diameter aerosols for approximately 22 minutes, and they observed NAD crystallization within a few minutes and NAT crystallization during the remaining observation time. In our experiments (which had a much shorter observation time) NAD did not form if the liquid aerosol composition was precisely 3:1, although it did form from aerosols of non-stoichiometric compositions between 2:1 and 3:1. (This is discussed in detail in the following section.)

These experiments have shown that at temperatures slightly above the glass transition temperature (between 161 K and 150 K for the 3:1 composition)⁸⁴ the crystal growth rate of NAT is slow, but the homogeneous nucleation rate is high. As a consequence, accurate laboratory measurements of NAT homogenous nucleation rates from liquid aerosol droplets by FTIR extinction measurements require enhancement of the crystal growth by raising the droplet temperature after nucleation.

For 1% of the small particles to freeze during a rapid temperature fluctuation, the homogeneous nucleation rate must be $1 \times 10^9 \text{ cm}^{-3} \text{ sec}^{-1}$ (see section 5.2.3). Extrapolation of our data to higher temperatures shows that 3:1 solutions have a rate of this magnitude at temperatures of 170 to 175 K. These temperatures are lower than those observed in the

polar stratosphere, so it is unlikely that freezing of 3:1 aerosol particles is a direct pathway for the formation of solid particles in the stratosphere.

5.4 NON-STOICHIOMETRIC HNO₃-H₂O AEROSOLS

The final experiments were performed on H₂O-HNO₃ aerosols with compositions ranging from 3:1 to 1.2:1. The range from 3:1 to 2:1 includes the compositions predicted by Meilinger *et al.* and Tias *et al.* (see section 5.1). The range from 2:1 to 1.2:1, even though not necessarily stratospherically relevant, is of interest because very little is known about freezing as a function of particle composition in this range. A systematic study over this range of compositions should increase our understanding of freezing in aqueous solutions, particularly nitric acid solutions.

5.4.1 Experimental

The low-temperature flow tube used in the non-stoichiometric work was the same as the one used in the stoichiometric experiments (see section 5.2.1 for a description of the apparatus). For all concentrations between 1.4:1 and 3:1, a two-stage temperature profile was used (see figure 5.14). Particles with concentrations between 1.4:1 and 2:1 did not freeze with this profile (proof of this is given in the following sections), so a three-stage temperature profile was implemented for these experiments (see figure 5.14). This profile is designed for compositions having a slow crystal growth rate at low temperatures. (A further discussion on the profiles used in each freezing experiment is given in the following sections.)

The major difference between the non-stoichiometric experiments and the stoichiometric experiments was the method for determining the composition. The composition of the stoichiometric aerosols was determined by relating changes in spectral bands to reagent flow. The correct flow ratio correlated with maxima in the spectral peaks assigned to the pure crystal. This technique, however, is incapable of determining the composition of non-stoichiometric aerosols because no corresponding maxima occur in this case. For non-stoichiometric aerosols, the composition is determined using the following method. First, the aerosol flow exiting the low-temperature flow tube is diverted to a glass

cell where the aerosol temperature is increased to 293 K. As a result, the aerosol particles completely vaporize and form nitric acid and water vapors. The partial pressures of these resulting vapors are then determined by FTIR spectroscopy. The ratio of these partial pressures is a direct measure of the aerosol composition, because this ratio is the same as the ratio of H₂O molecules to HNO₃ molecules in the aerosol particles. This, of course, assumes that the amount of vapor phase H₂O and HNO₃ in the low-temperature flow tube is much smaller than total H₂O and HNO₃, a reasonable assumption in these experiments.

A block diagram of the apparatus used for these measurements is shown in figure 5.20. The low-temperature flow tube is displayed in the top part of the figure, and the glass cell used for gas phase analysis is displayed in the bottom part of the figure. The flow tube is connected to the glass cell by a piece of Teflon tubing which is 1/2 " ID and 24 " long. This Teflon tube is heated to ensure the vapors that enter the glass cell are at 293 K. A thermocouple (type K) situated at the inlet of the glass cell monitors this temperature. The glass cell is 1 " ID and 7.5 " long and has AgCl windows attached on both ends by Teflon mounts. This assembly is located in the sample compartment of a Bruker FTIR spectrometer. Spectra of the cell contents are recorded with this spectrometer at 0.5 cm⁻¹ resolution over the range of 500 cm⁻¹ to 4500 cm⁻¹.

The IR spectrum was calibrated for nitric acid and water vapor by recording IR spectra of known partial pressures of these gases. The source of these known partial pressures was a saturator, a glass vessel containing various solutions of nitric acid and water. (The vapor pressures of these solutions were calculated from an equilibrium model.)⁸⁵ During the calibration experiments, the saturator was connected directly to the glass cell shown in figure 5.20, and a slow flow of nitrogen was passed through the saturator and then through the glass cell. At the same time, spectra of the cell contents were recorded. Saturation of the carrier gas was verified by monitoring the spectrum of the vapors as a function of the flow rate of the carrier gas. For a range of flow rates, the intensities of the IR bands remain constant, but as the flow increased above a certain value, the intensity of these bands decreased. For all flow rates less than this certain value, we assumed the carrier gas was saturated. The flow rate used in the calibration experiments was less than half of the flow rate needed for saturation.

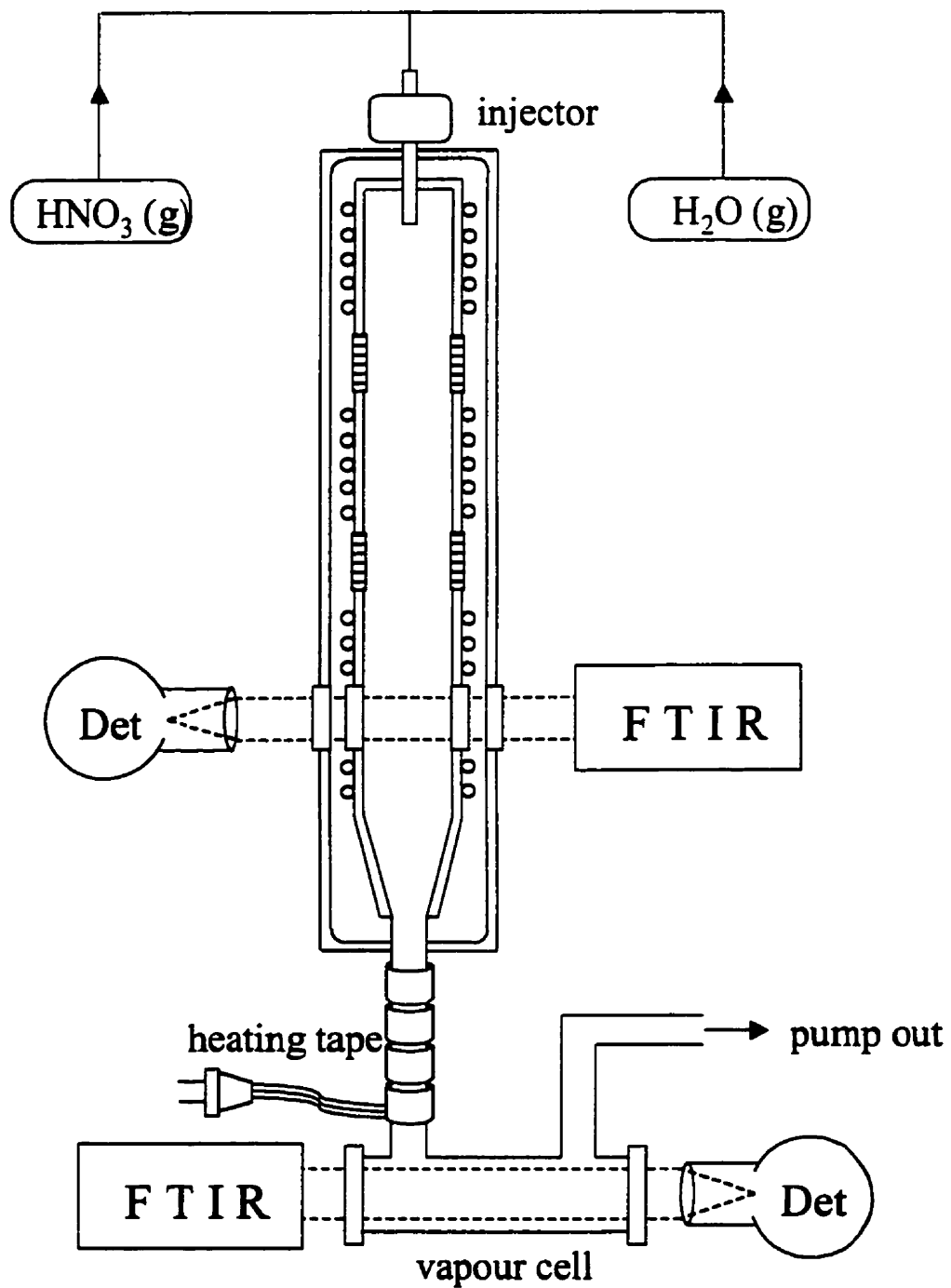


Figure 5.20 Schematic diagram of the apparatus used in the non-stoichiometric freezing experiments.

Using the technique described above, we recorded IR spectra for a range of nitric acid and water partial pressures. Shown in figure 5.21 are three of these spectra. As indicated in the figure, the sharp features at approximately 3700 and 1500 cm^{-1} are from water vapor, and the unresolved features at 3550, 1710, 1320 and 880 cm^{-1} , are from nitric acid vapor. Also indicated in the bottom part of this figure are the water lines (1889, 1990 cm^{-1}) and the nitrate band (760 cm^{-1}) we used for calibration purposes. Plotted in figures 5.22 and 5.23 are the integrated areas of these features as a function of partial pressure. The curve in each figure is the result of a least squares fit (second order polynomial) to the data. The parameters of each fit were used to convert absorption intensities into vapor pressures of nitric acid and water.

The error associated with this method of compositional analysis was estimated by preparing stoichiometric 3:1 and 2:1 aerosols in the low-temperature flow tube. (The method for preparing and characterizing precise 3:1 and 2:1 aerosols was described in the previous two sections.) We then determined the composition of these aerosols independently by measuring the gas phase as described above. In all cases, the ratio determined with our new technique agreed with the stoichiometric ratios to within $\pm 0.2:1$ ($\text{H}_2\text{O}:\text{HNO}_3$). We quote this as our uncertainty in determining the composition of non-stoichiometric particles.

To do a non-stoichiometric freezing experiment, we first set the temperatures of the cooling sections to their appropriate values (see above for a discussion on the temperature profiles used in these experiments). After the temperatures are established, the flows of nitric acid and water vapor are adjusted until the desired particle composition is obtained. The temperature of either the second or final cooling section is then increased while both aerosol and gas phase spectra are recorded. The phase of the aerosol is determined from the aerosol spectra, and the composition is determined from the gas phase spectra.

5.4.2 Results

1.2:1 < H₂O:HNO₃ < 1.4:1

Shown in figure 5.24 are results from an experiment performed on 1.2:1 particles. The spectra correspond to temperatures ranging from 186 K to 156 K, yet there is virtually

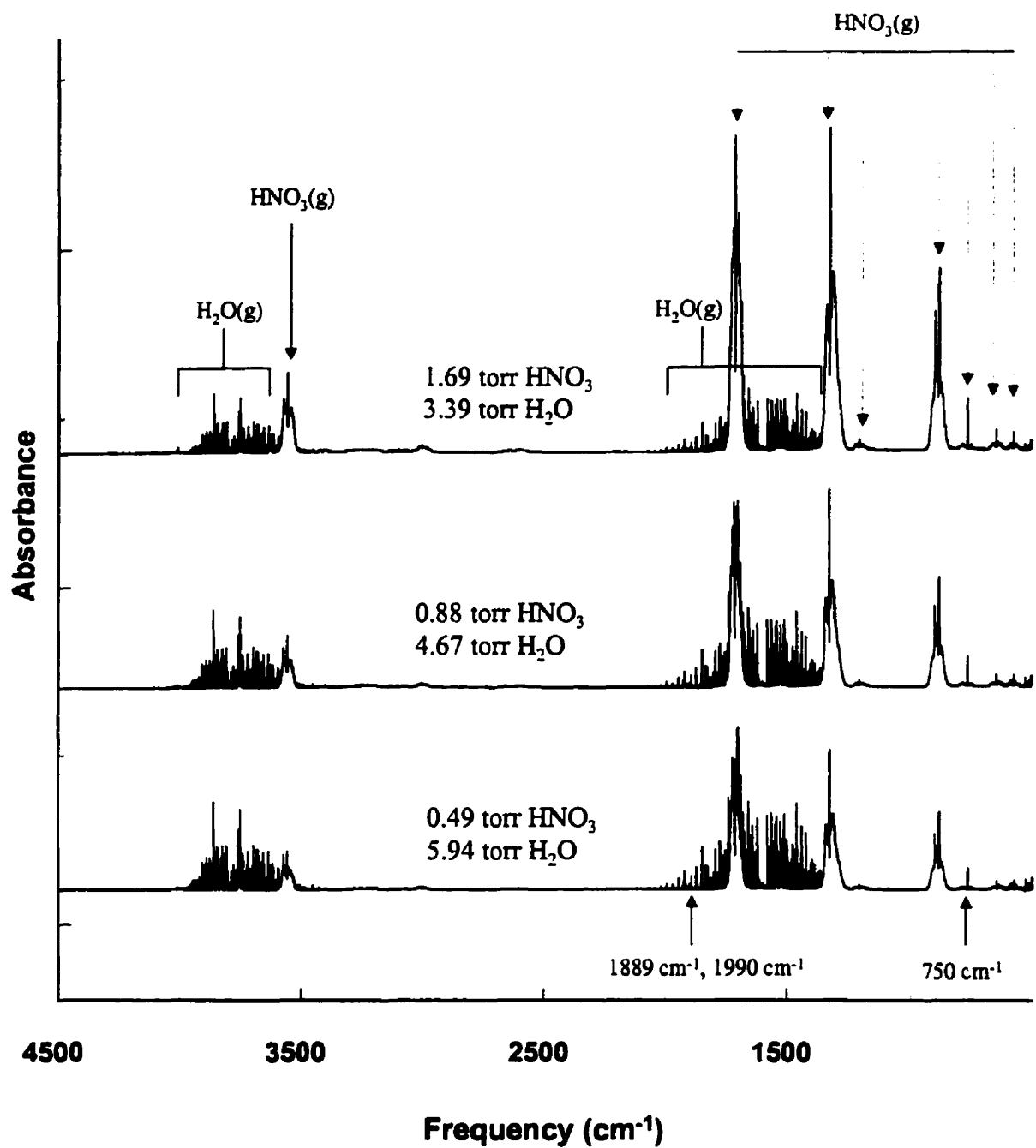


Figure 5.21 IR spectra of nitric acid and water vapors. The vapor pressures which correspond to each spectrum are indicated in the figure.

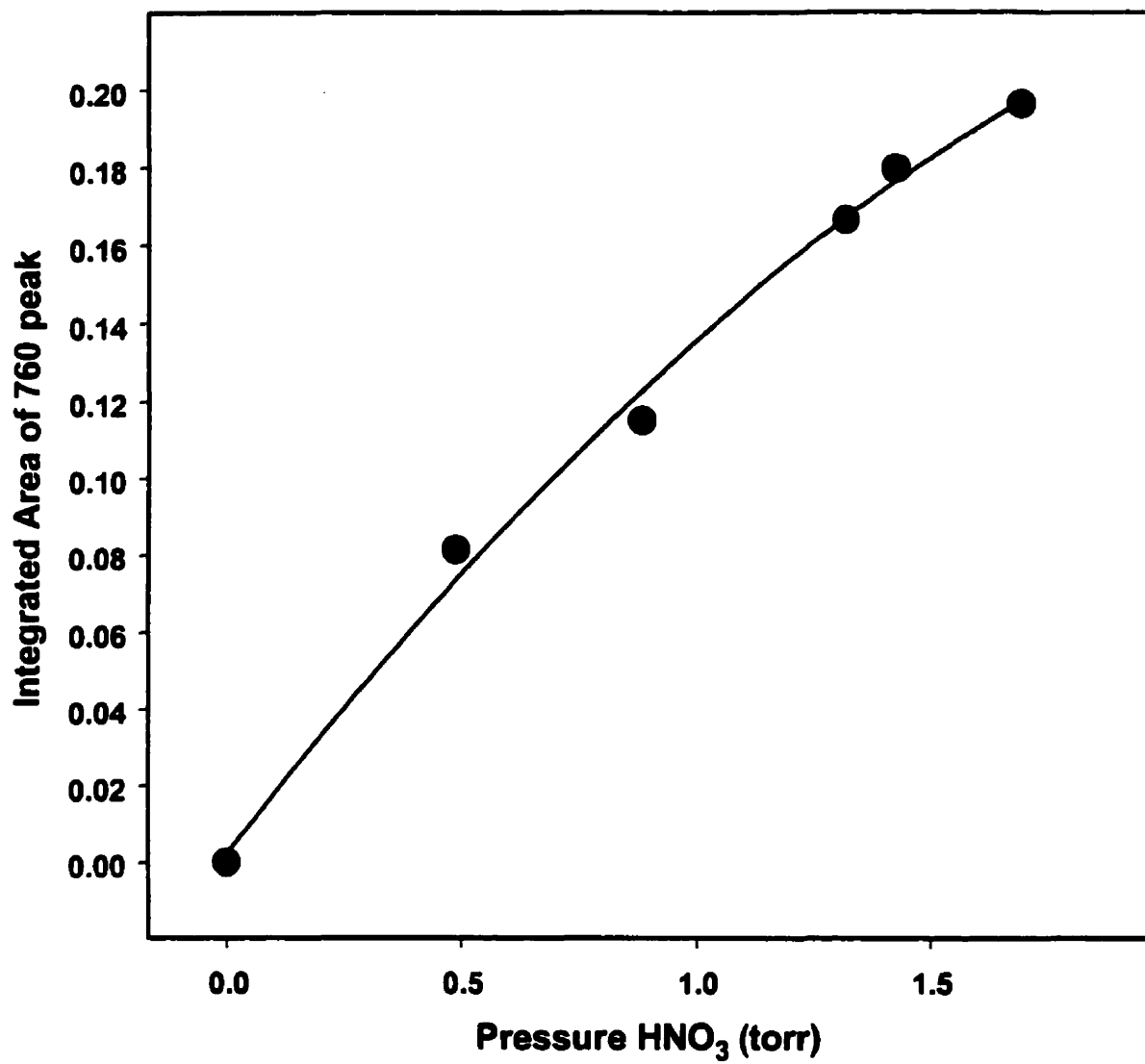


Figure 5.22 HNO₃(g) calibration curve for the non-stoichiometric experiments.

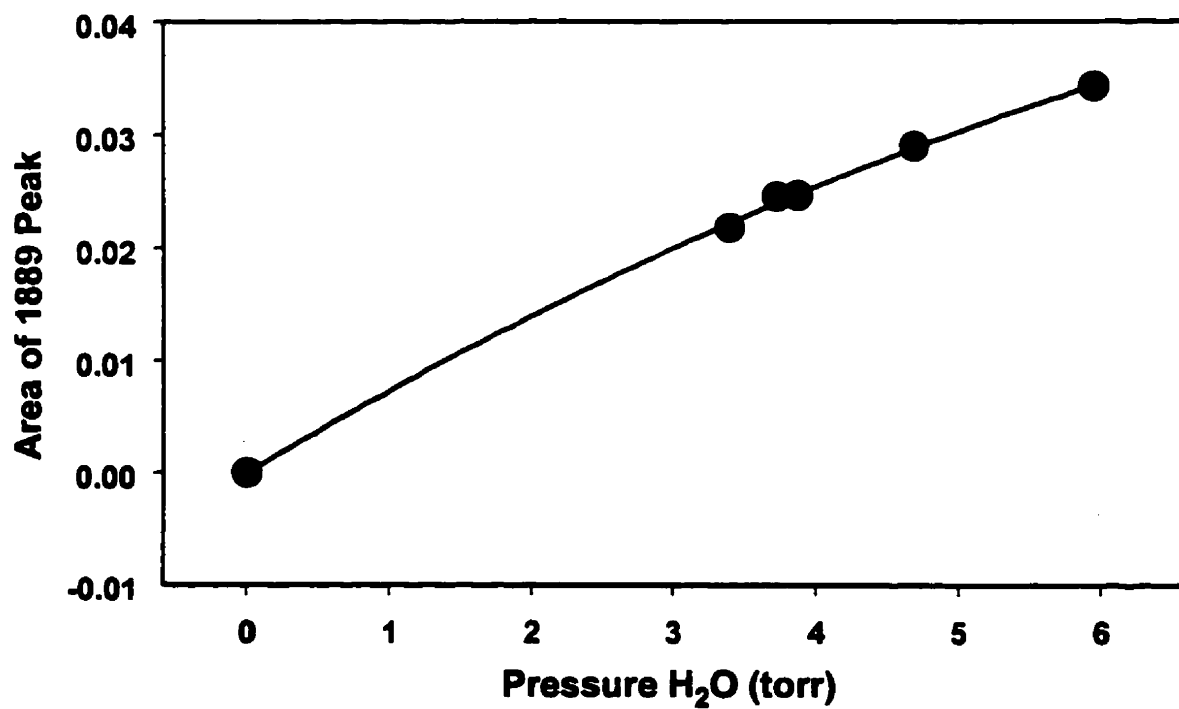
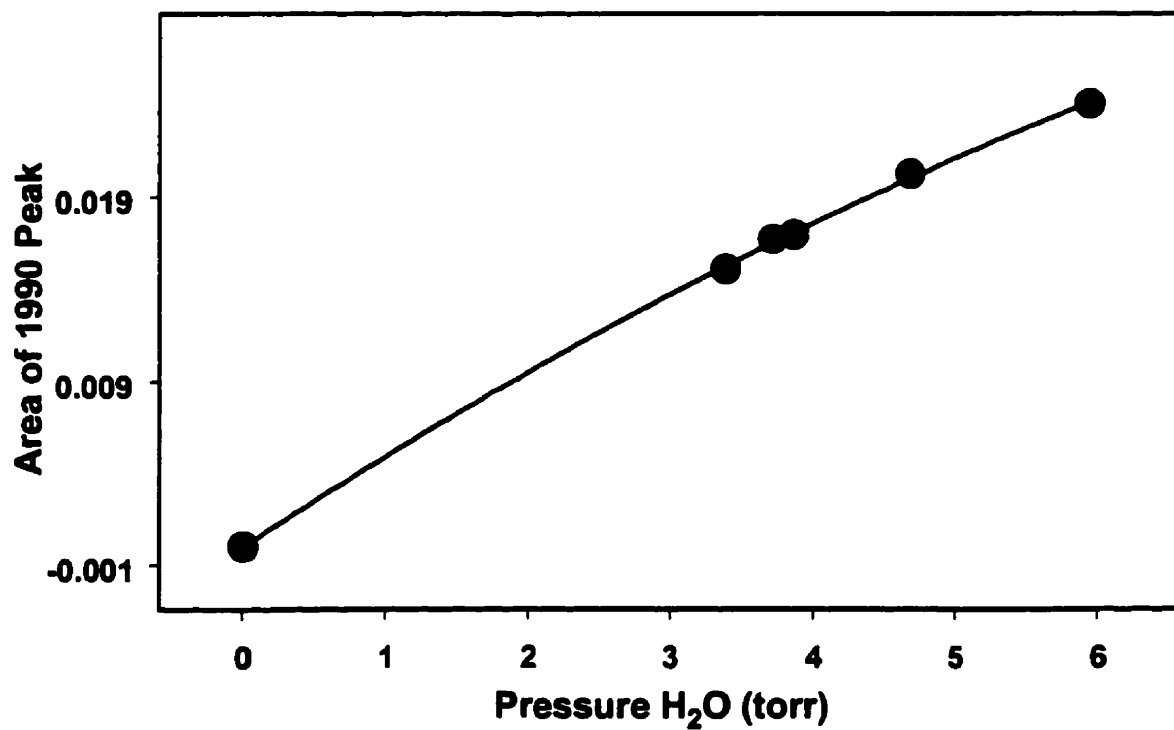


Figure 5.23 H₂O(g) calibration curves for the non-stoichiometric experiments.

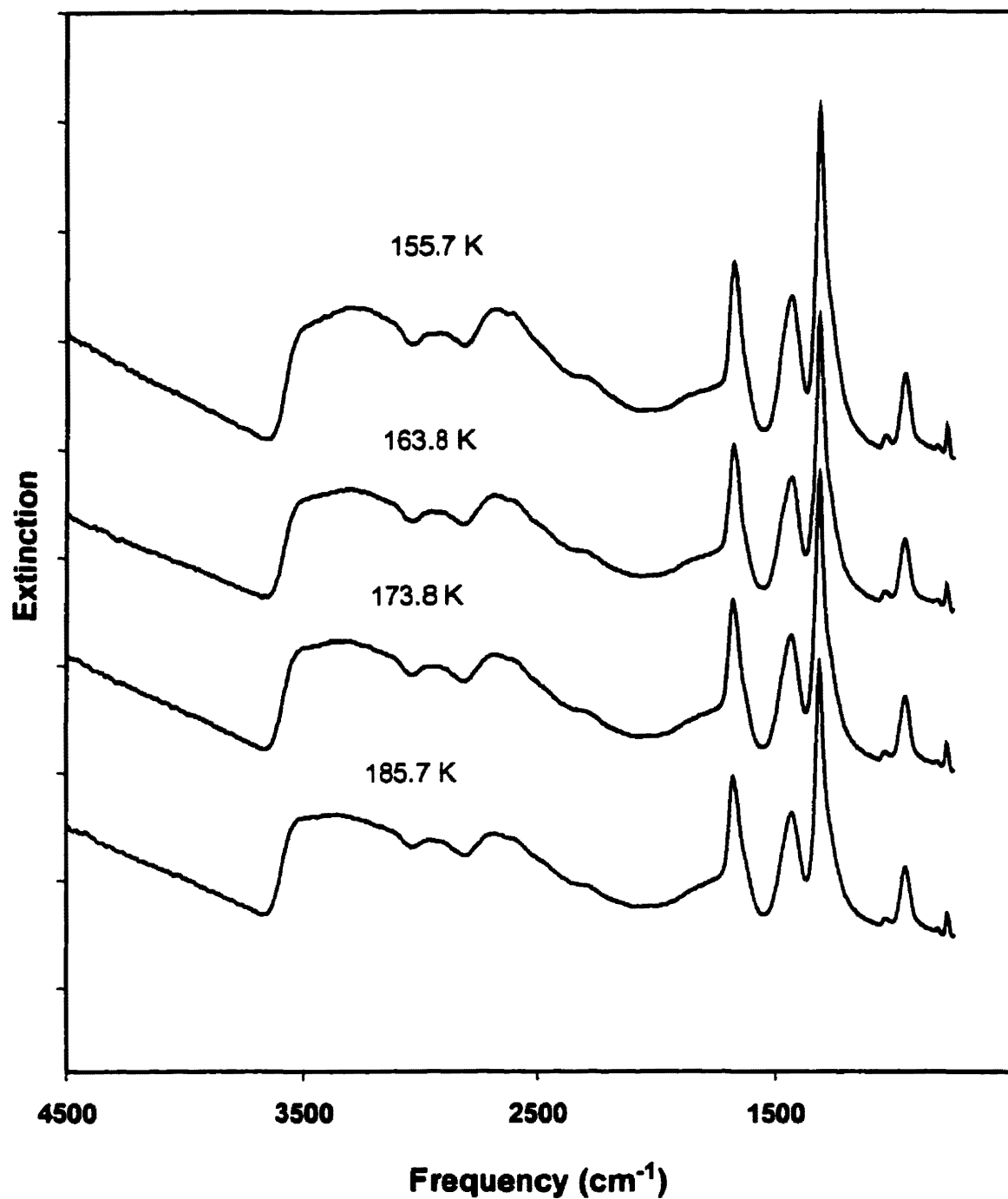


Figure 5.24 Temperature dependent spectra of a HNO₃-H₂O aerosol with a composition of 1.2:1. The spectra have been offset in the vertical direction.

no differences among any of the spectra. There are subtle changes during cooling, most noticeably in the OH region: the shape of the 3500 cm^{-1} band changes slightly as the aerosol is cooled. These changes, however, are consistent with cooling of a liquid aerosol.^{75,79} We also subtracted successive spectra to make small changes more discernible, but even with this sensitive technique, we were unable to detect crystallization.

Because of the similarity in the concentrations, we expected nitric acid monohydrate (NAM) to crystallize in the 1.2:1 particles. A calculated spectrum of this hydrate (curve a) is displayed in figure 5.25. The optical constants used to calculate the spectrum were taken from reference 78. Also included in this figure, for comparison purposes, is the top spectrum in figure 5.24. Clearly, the experimental spectrum doesn't resemble the calculated spectrum of NAM. Furthermore, there are no features in the experimental spectrum that would indicate crystallization of any hydrate.⁷⁵

The spectra displayed in figure 5.24 were recorded with a two-stage temperature profile; that is, the first two sections were held at 188 K and the final section was varied. We also carried out experiments on 1.2:1 particles with a three-stage temperature profile. (The first and third sections were held at 188 K and 178 K respectively, while the middle section was varied.) Nevertheless, results identical to the ones displayed in figure 5.24 were obtained. Because the three-stage profile increases the crystal growth rate (see section 5.3), we conclude that the homogeneous nucleation rate of 1.2:1 particles is below our detection limit.

The results observed in the 1.2:1 experiments were typical for compositions ranging from 1.2:1 to 1.4:1. In all cases, no features associated with crystallization were observed in the IR spectrum over the entire temperature range investigated.

1.4:1 < H₂O:HNO₃ < 2:1

Unlike the spectra described above, the spectra of particles with compositions ranging from 1.4:1 to 2:1 do change noticeably between 170 K and 180 K. These changes are shown in figure 5.26 for the case of the 1.6:1 composition. The bottom spectrum has broad features that are characteristic of liquid HNO₃-H₂O.^{75,79} In contrast, the top three spectra clearly have sharp features at 3490 , 3250 , 1455 , and 1030 cm^{-1} that are

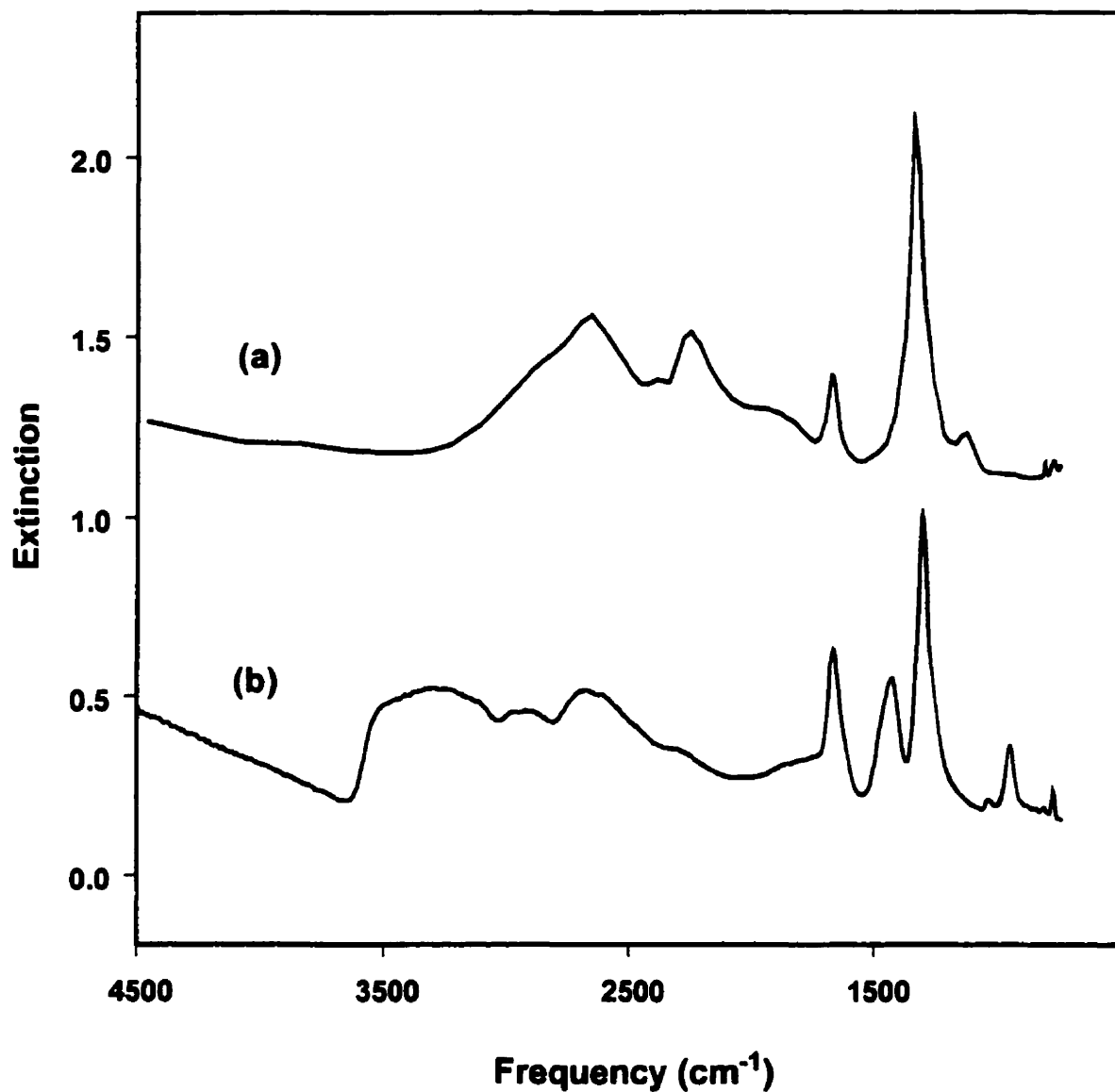


Figure 5.25 Curve (a) is a calculated spectrum of nitric acid monohydrate (NAM). Curve (b) is a measured spectrum of a 1.2:1 aerosol at 155.7 K. The spectra have been offset in the vertical direction.

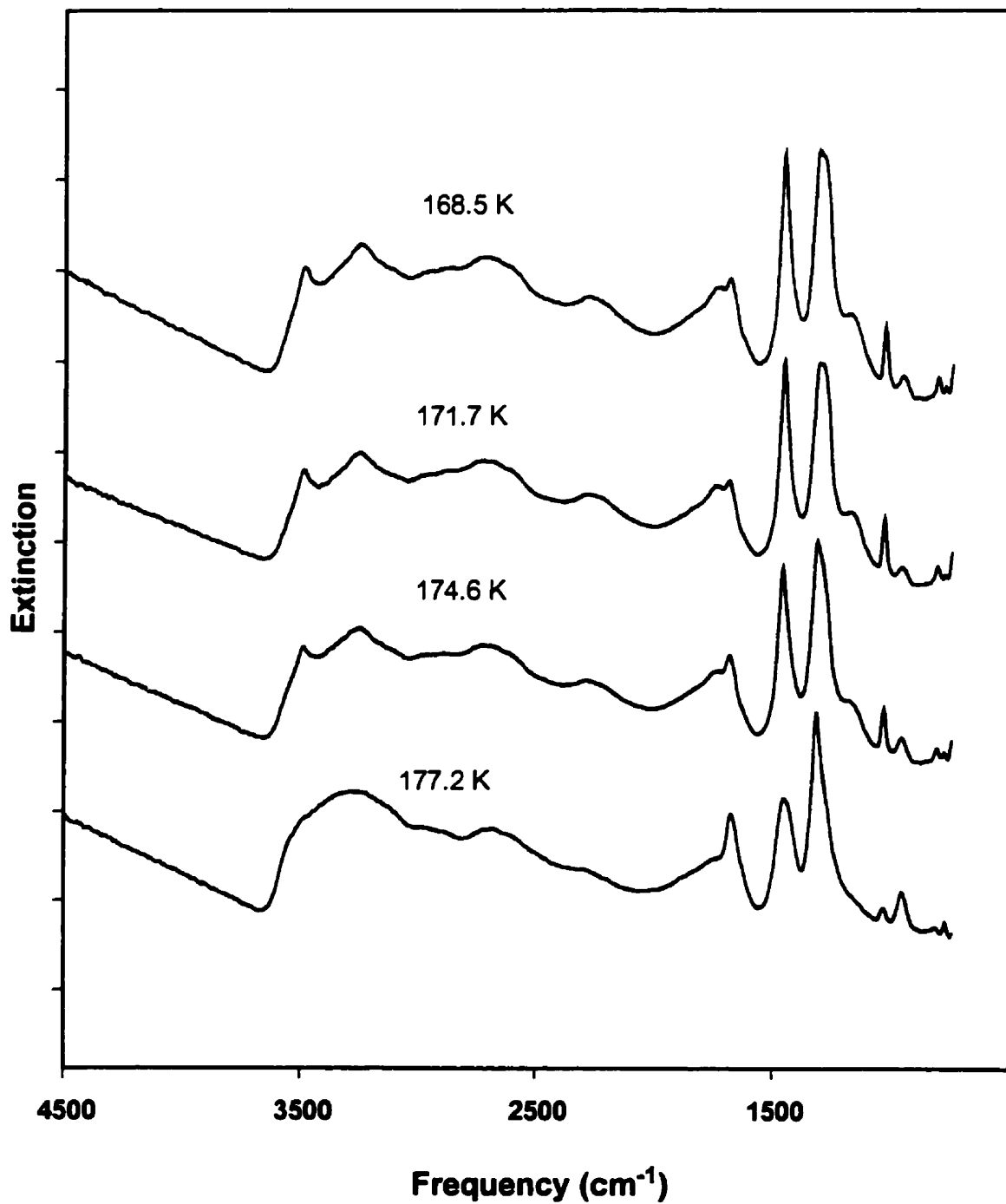


Figure 5.26 Spectra of a HNO₃-H₂O aerosol with a composition of 1.6:1. The temperature that corresponds to each spectrum is indicated in the figure. The spectra have been offset in the vertical direction.

characteristic of NAD.^{75,79} From this we conclude that a 1.6:1 aerosol remains liquid until approximately 175 K, at which temperature NAD forms in the aerosol particles.

Because the spectra in figure 5.26 correspond to a 1.6:1 aerosol, it is not possible for the entire aerosol to freeze as NAD, which has a 2:1 stoichiometry. To determine what remains in the aerosol particles after NAD formation, we subtracted an aerosol spectrum of pure NAD from the spectrum recorded at 174.6 K. (The aerosol spectrum of pure NAD was recorded during the 2:1 stoichiometric work, which is described in section 5.2.) The resulting spectrum, displayed in figure 5.27, is very similar to the liquid spectrum of 1.6:1 particles, which is also displayed in the same figure for comparison purposes. There are, however, slight differences between the subtracted spectrum and the liquid spectrum. First of all, the ratio of the peak height at 950 cm^{-1} to the peak height at 1035 cm^{-1} is slightly larger in the subtracted spectrum than in the original liquid spectrum. In addition, the relative peak height at 1675 cm^{-1} is larger in the subtracted spectrum. Both the 950 cm^{-1} and the 1675 cm^{-1} features are due to molecular HNO_3 in solution, whereas the 1035 cm^{-1} feature is due to NO_3^- in solution.^{15,75} An increase in the HNO_3 features with respect to the NO_3^- feature indicates that a liquid solution remains in the particle after NAD formation and that the liquid is slightly more concentrated than the original solution. The results described above were observed for all aerosols with compositions between 1.4:1 and 2:1.

2.7:1 < H₂O:HNO₃ < 3:1

Spectra of 2.8:1 particles at temperatures ranging from 177.3 to 169.2 K are shown in figure 5.28. The bottom spectrum is the characteristic spectrum of liquid $\text{HNO}_3\text{-H}_2\text{O}$.^{75,79} This spectrum, however, changes considerably as the aerosol is cooled. In the nitrate region, the bands at 1455, 1295, and 1030 cm^{-1} sharpen and grow in intensity while the shoulder at 1160 cm^{-1} develops. These changes are consistent with crystallization of NAD.^{75,79} The formation of peaks at 3490 and 3250 cm^{-1} in the OH region are also consistent with this freezing mechanism. The only other major change in the spectrum with temperature is the development of a small feature at 3430 cm^{-1} . This peak indicates that NAT, in addition to NAD, forms in the particles as they are cooled.^{75,83} (The peaks assigned to NAD and NAT are indicated in the figure.)

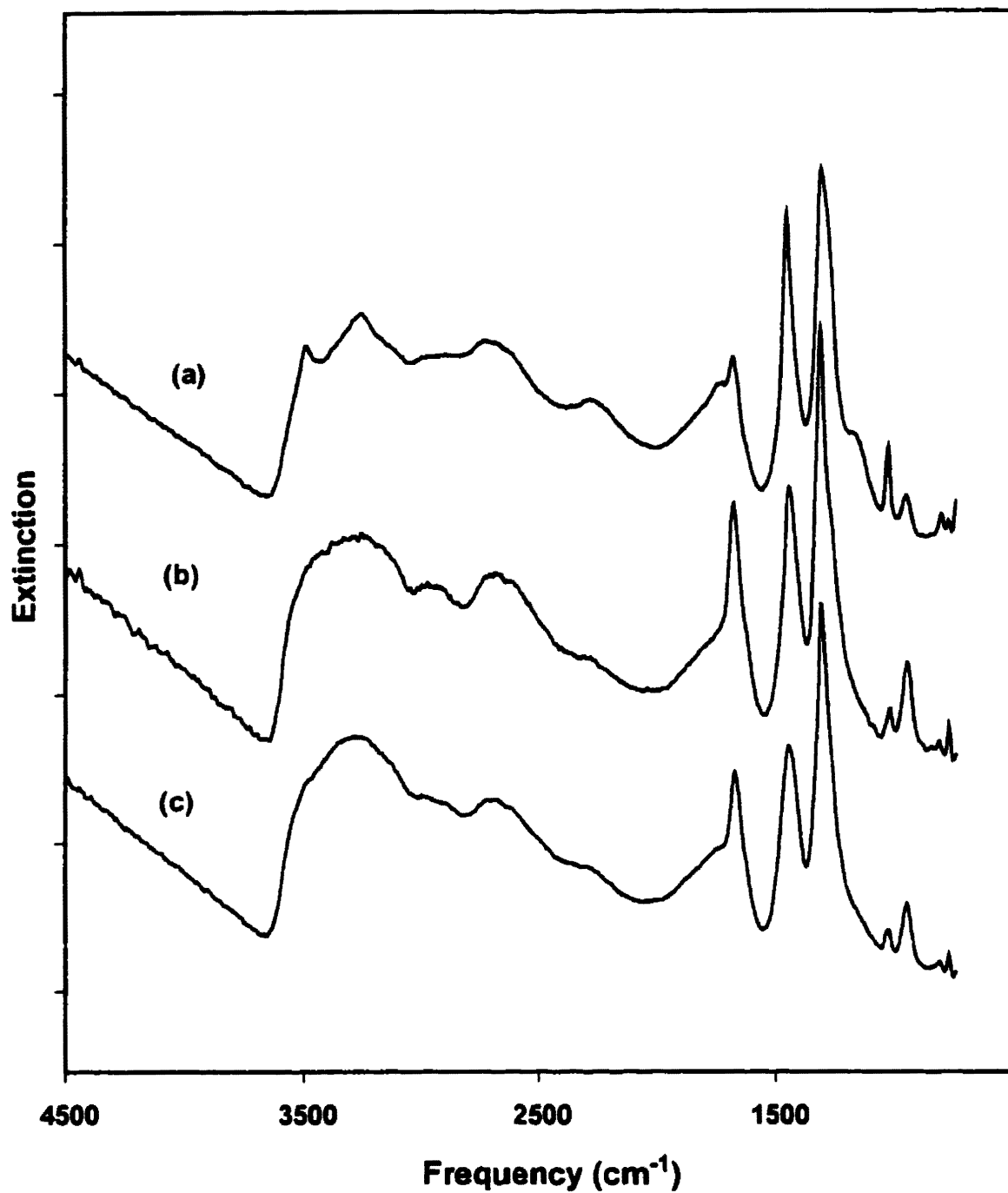


Figure 5.27 Curve (a) is a measured spectrum of a 1.6:1 aerosol at 174.6 K. Curve (b) is the result of subtracting a NAD spectrum from curve (a). Curve (c) is a measured spectrum of a 1.6:1 aerosol at 177.2 K. The spectra have been offset in the vertical direction.

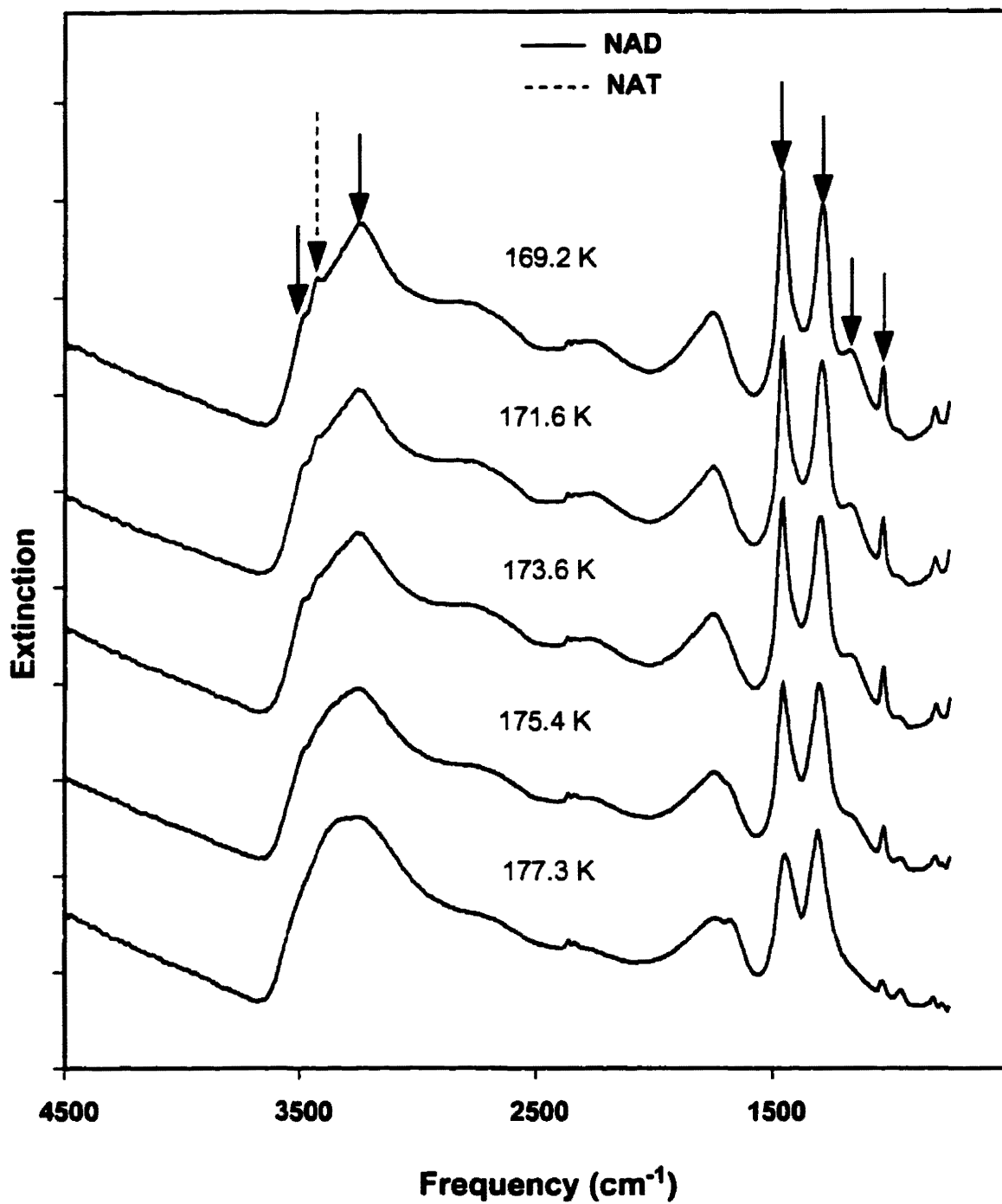


Figure 5.28 Temperature dependent spectra of a HNO₃-H₂O aerosol with a composition of 2.8:1. The spectra have been offset in the vertical direction.

The freezing mechanism proposed above (NAD and NAT crystallization in 2.8:1 particles) is further supported by the results shown in figure 5.29. Spectrum a is the 171.6 K spectrum from figure 5.28, while spectrum d is the 177.5 K spectrum from the same figure. Spectrum b is the result of subtracting an aerosol spectrum of pure NAD from spectrum a. Clearly, there are features in this difference spectrum that cannot be assigned to the liquid: for example, the OH region. Spectrum c is the result of adding an aerosol spectrum of pure NAT to the liquid spectrum (d). (The aerosol spectrum of pure NAT was recorded during the stoichiometric work, which is described in section 5.3.) The resulting spectrum (c) is very similar to spectrum b. From this, we conclude that 2.8:1 particles at temperatures below approximately 172 K are composed of NAD, NAT and liquid HNO₃-H₂O. A similar trend was observed for all compositions ranging from 2.7:1 to 3:1. In all cases, both NAD and NAT features appeared in the IR spectrum.

Freezing points

From the temperature dependent spectra of the non-stoichiometric aerosols, we also determined the precise temperatures at which crystallization first occurred (freezing point). The procedure for determining the freezing point has been discussed in detail in both sections 5.2 and 5.3. Briefly, the method involves calculating the difference between each spectrum and a liquid spectrum recorded within a few degrees of the freezing point. For these experiments, we calculated the difference over the frequency range of 3100 cm⁻¹ to 3650 cm⁻¹. This region was chosen because both NAD and NAT, the two hydrates identified in this work, have spectral features in this range. Shown in figure 5.30 are the differences calculated from the results of the 2.8:1 experiment. Unlike the differences determined in the stoichiometric experiments, these differences are not normalized to 1. In the stoichiometric experiments, the particles completely crystallized at low temperatures. Consequently, we normalized the largest difference to 1 and assumed that the resulting differences represent the volume fraction frozen. In these experiments, however, the particles did not completely crystallize. The points in figure 5.30 represent the experimental measurements. The solid line (a) that goes through the points above 176 K is a linear regression to the data; the dashed lines above and below this show the location of

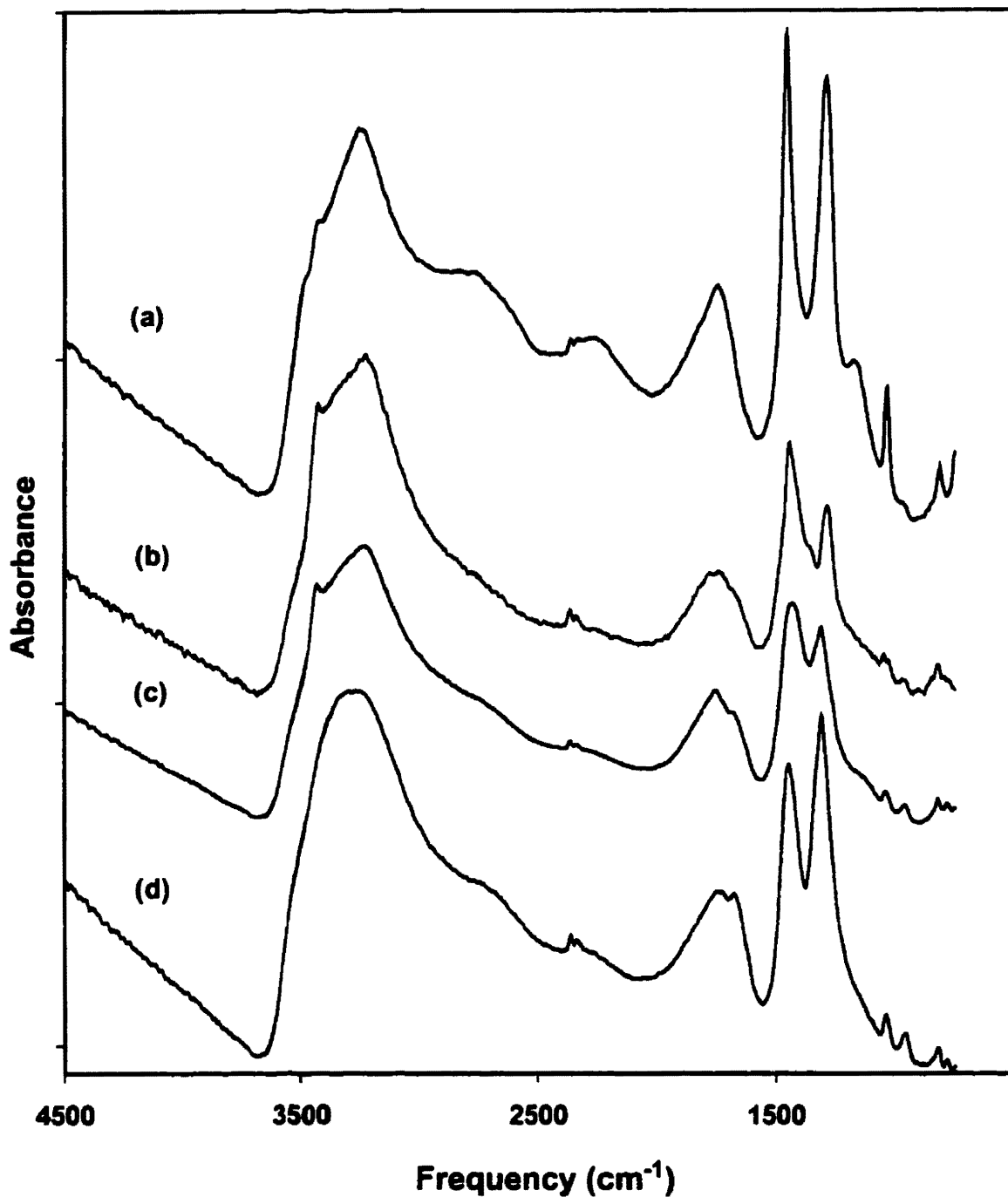


Figure 5.29 Curve (a) is a spectrum of a 2.8:1 aerosol at 171.6 K. Curve (b) is the result of subtracting an aerosol spectrum of pure NAD from curve (a). Curve (c) is the result of adding an aerosol spectrum of pure NAT to curve (d). Curve (d) is a spectrum of a 2.8:1 aerosol at 177.3 K. The spectra have been offset in the vertical direction.

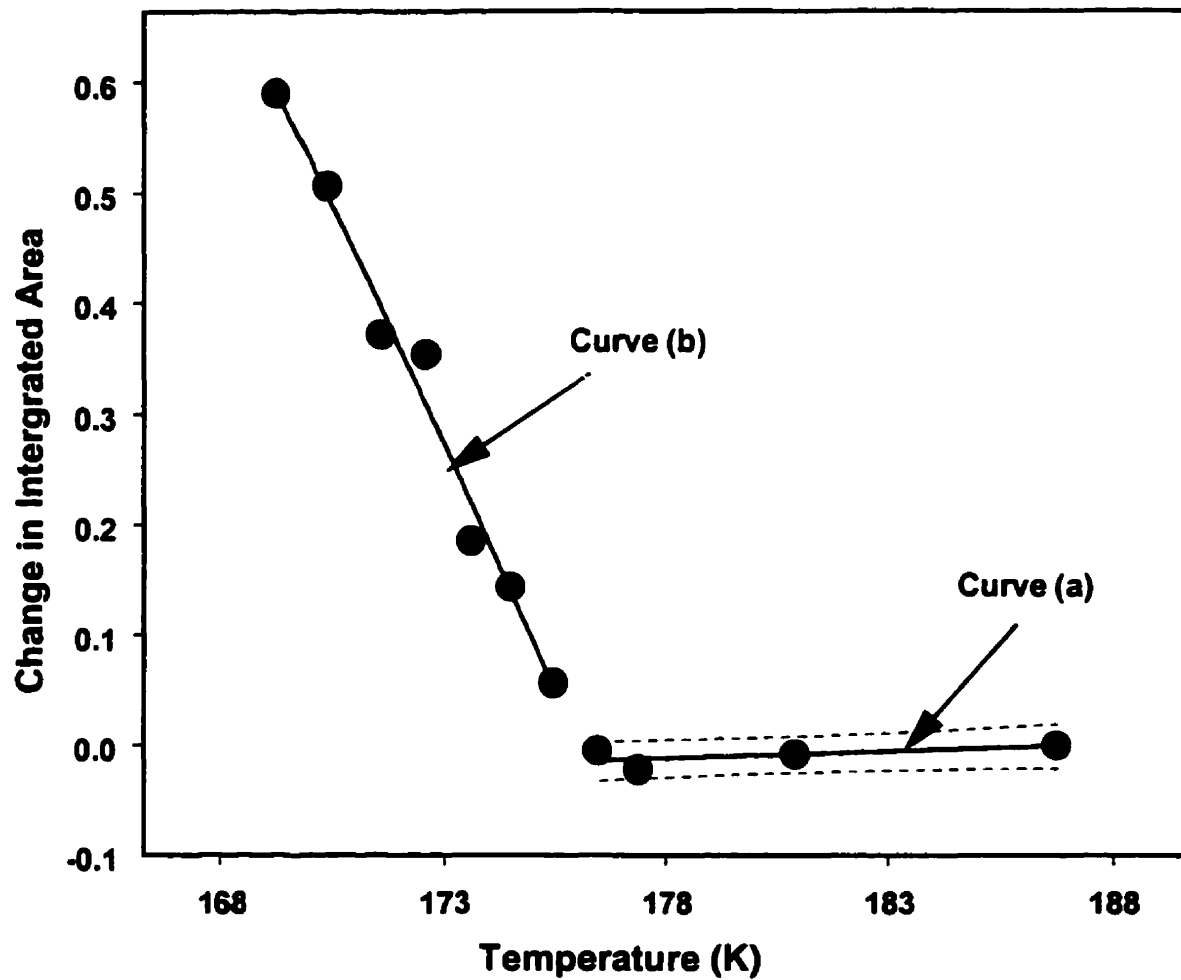


Figure 5.30 Plot of the change in the OH region of the 2.8:1 spectrum as a function of temperature. The change in area is a result of freezing.

the 2σ values of this least squares fit. The curve (b) in the figure is a least squares fit to the points below 176 K. The freezing point is determined by extrapolating this curve and the linear regression line (a) until the two intersect. The point at which the two intersect is considered the freezing point.

Shown in figure 5.31 are freezing points as a function of particle composition. The hatched region represents the concentration and temperature range where no freezing was observed. The temperature range investigated in these experiments was 188 K to 153 K, but the hatched region has been truncated at 158 K for presentation purposes. The circles in the figure represent freezing points of non-stoichiometric particles. The squares represent freezing points of stoichiometric particles (these results were discussed in section 5.2 and 5.3.) The solid curve is a least squares fit (third order polynomial) to all the freezing points.

The freezing points in figure 5.31 indicate that the maximum freezing temperature for compositions ranging from 1.2:1 to 3:1 occurs at a composition of 2:1. The curve in figure 5.31, however, indicates the maximum is at approximately 2.2:1; further measurements in this range are needed to verify this categorically. The freezing point data also indicate that the freezing temperature decreases substantially as the composition deviates from 2:1.

5.4.3 Discussion and Conclusions

Nitric acid-water particles with average radii of approximately 0.4 microns have been studied over the range of 188 K to 153 K. The time the aerosol was held at these temperatures was approximately 15 seconds. From the temperature dependent spectra of these aerosols, the following conclusions were drawn: Aerosols with compositions between 1.2:1 and 1.4:1 did not crystallize at any of the temperatures investigated. NAD formed in particles with compositions ranging from 1.4:1 to 2:1, and NAD and NAT formed in particles with compositions ranging from 2.7:1 to 3:1. From the temperature dependent spectra, freezing temperatures of these particles were also determined. These results indicate that the maximum freezing temperature for compositions ranging from 1.2:1 to 3:1 occurs at a composition of approximately 2:1.

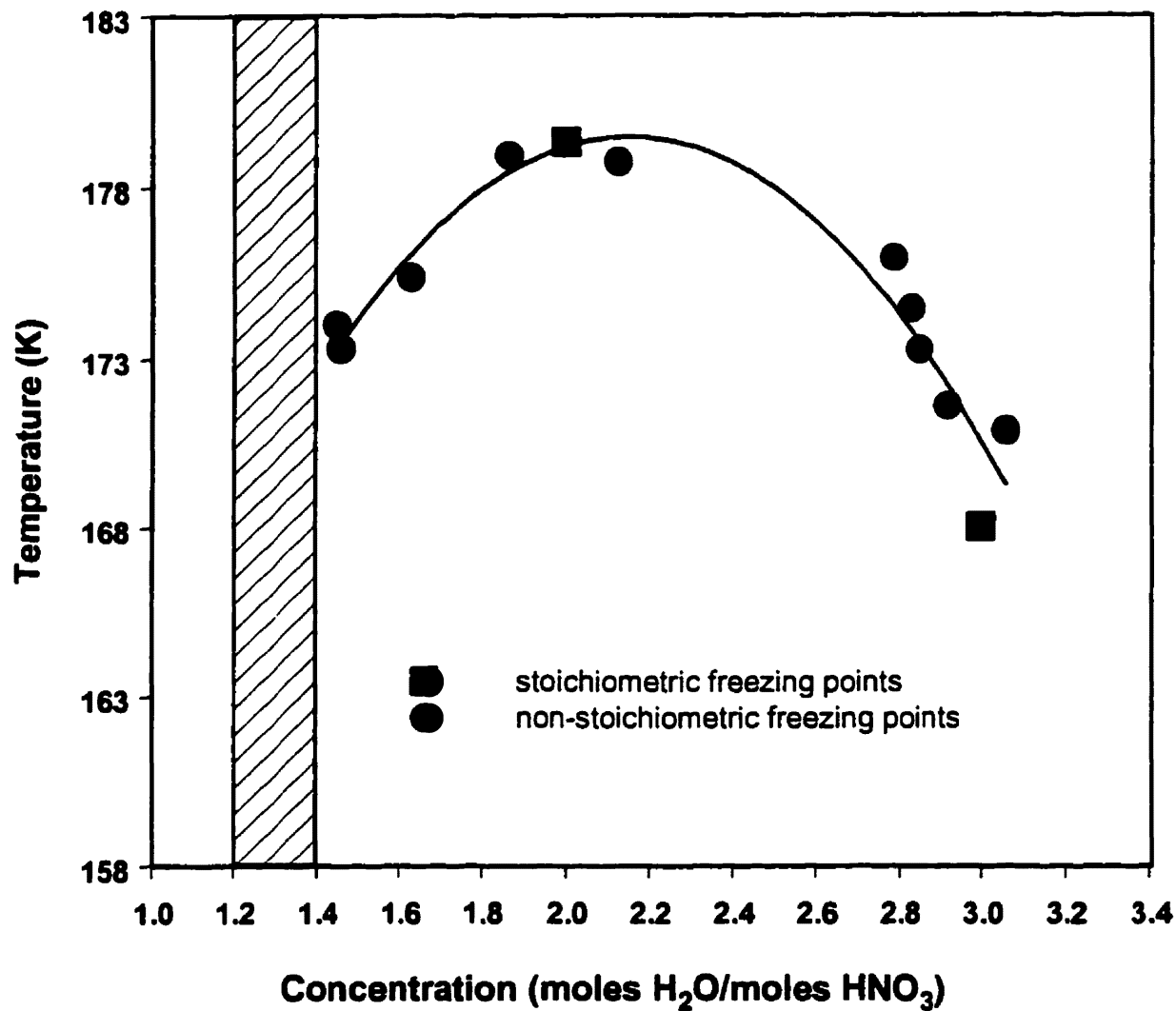


Figure 5.31 Freezing data from the stoichiometric and non-stoichiometric experiments. The hatched region represents the the temperature and composition range where no freezing was detected. The circles represent the freezing points from the non-stoichiometric experiments. The squares represent the freezing points from the stoichiometric experiments.

Barton *et al.*⁷⁹ have also investigated the freezing of non-stoichiometric solutions of $\text{HNO}_3\text{-H}_2\text{O}$. These authors observed NAD formation in particles with compositions ranging from approximately 1.2:1 to 2.5:1, and NAD and NAT formation in particles with compositions ranging from 2.5:1 to 3:1. These results are consistent with our observations, except for compositions less than 1.4:1. Our results indicate that particles with concentrations between 1.2:1 and 1.4:1 remain supercooled at temperatures as low as 153 K, whereas Barton *et al.* observed NAD formation at 185 K with similar compositions. These apparently contradictory results are probably due to the different observation times in the two experiments. Barton *et al.* noted that it took approximately 8 minutes to form NAD in concentrated particles. In our experiments, however, the aerosol is only held at the final temperature for approximately 15 seconds. Barton *et al.* also investigated non-stoichiometric solutions with compositions between 3:1 and 4:1. Formation of both NAD and NAT was reported for this concentration range. We have not investigated this range; however, we did not see NAD form in the particles with a composition of 3:1 (see section 5.3 for a further discussion).

Non-equilibrium models by Meilinger *et al.*²⁶ and Tsias *et al.*²⁷ predict that PSCs can approach a binary nitric acid solution with concentrations ranging from 52 wt % to 58 wt %. These authors speculated that these binary particles freeze as NAT or NAT during a rapid temperature fluctuation. In section 5.2.3, we argued that 2:1 aerosols will not freeze under these conditions. Since the maximum freezing point temperature in figure 5.31 corresponds to the 2:1 composition, we also suggest that freezing will not occur for any of the compositions predicted by Meilinger *et al.* and Tsias *et al.* This, of course, assumes that the homogeneous nucleation rates of the 2:1 solution and the non-stoichiometric solutions have similar temperature dependencies. (To predicting freezing at stratospheric temperatures, we must extrapolate our measured rates to higher temperatures.) The temperature dependence of the 2:1 and 3:1 freezing rates are virtually identical (see figure 5.19). Therefore, it is reasonable to assume that the nucleation rates of solutions with compositions between 2:1 and 3:1 will also have a similar temperature dependence.

CHAPTER SIX

CONCLUDING REMARKS

6.1 CONCLUSIONS

In the previous chapters, experiments on $\text{H}_2\text{SO}_4\text{-H}_2\text{O}$ and $\text{HNO}_3\text{-H}_2\text{O}$ aerosols were described. The apparatus and techniques used in these experiments proved to be extremely useful for determining phases and phase transition kinetics of aerosol particles. Using IR spectroscopy, we were able to determine the phases of the aerosols and the precise temperature at which the phase transitions occurred. We were also able to determine, using Mie scattering calculations, the size of the particles under investigation. In most cases only limits for the log-normal size parameters were determined, but the sensitivity to particle size could be increased in future experiments by working with larger particles. From the experimental results, we were also able to determine the kinetics of the phase transitions. This information allowed us to predict the long-time behavior of stratospheric aerosols from our short-time observations.

It is unlikely, based on the results presented in this thesis, that steps 1 and 9 in figure 1.1 are important in PSC freezing. We observed concentrated $\text{H}_2\text{SO}_4\text{-H}_2\text{O}$ aerosols at temperatures ranging from approximately 240 K to 180 K, yet no freezing was detected. This finding is in agreement with recent laboratory results on this system which strongly suggest that step 1 does not occur at stratospheric conditions. Unlike concentrated $\text{H}_2\text{SO}_4\text{-H}_2\text{O}$ aerosols, $\text{HNO}_3\text{-H}_2\text{O}$ aerosols did freeze in our experiments. NAD crystallized in particles with concentrations ranging from 1.4:1 to 2:1, and both NAD and NAT crystallized in particles with concentrations ranging from 2.7:1 to 3:1. From these experimental results, we determined that the homogeneous nucleation rate is relatively large at temperatures below approximately 175 K. The homogeneous nucleation rates determined by extrapolating our measured rates to stratospheric temperatures, however, are not large enough to cause significant freezing of PSCs. Consequently, step 9 is also unlikely.

The results from the $\text{H}_2\text{SO}_4\text{-H}_2\text{O}$ and $\text{HNO}_3\text{-H}_2\text{O}$ experiments suggest that another pathway besides steps 1 and 9 are responsible for the formation of solid PSCs. One

possibility is step 6 in figure 1.1. This step involves the precipitation of ice out of dilute nitric acid particles that have only a small fraction of sulfuric acid (<5 wt %). We have shown that ice precipitates out of dilute sulfuric acid particles at approximately 35 K below the equilibrium freezing temperatures. Also, recent calculations suggest that dilute nitric acid solutions behave in a similar manner to dilute sulfuric acid solutions.⁸⁶ Consequently, step 6 is likely responsible for the formation of solid PSCs below the ice frost point (the temperature below which ice is thermodynamically stable). Other possibilities for solid formation include the freezing of ternary aerosols (step 4) and heterogeneous nucleation.

6.2 CONSIDERATIONS FOR FURTHER WORK

The obvious starting point for future work is steps 4 through 7 in the transition diagram displayed in figure 1.1. This thesis has focused on step 1 and step 9. Studies on steps 4 through 7 would complete this work. Steps 6 and 7 involve the freezing of a dilute nitric acid solution with a H₂SO₄ concentration less than 5 wt %. Both ice and NAT have been proposed as the freezing products.²³ The importance of steps 6 and 7 in PSC freezing could be addressed by simply extending the nitric acid work described in section 5.4 to include dilute compositions. (The binary aerosol is a reasonable approximation to this ternary aerosol because of the low concentration of H₂SO₄ in the particles.) Steps 4 and 5 involve the freezing of ternary solutions (see figure 5.1 for relevant temperatures and concentrations). The importance of these steps could also be addressed with the current apparatus, but a method of determining the composition of ternary particles would have to be developed. A method similar to those described in this thesis should be appropriate and relatively easy to implement.

Besides PSC formation, cirrus cloud formation is another possible topic to investigate with the current apparatus. Recent field and theoretical work has indicated that ammoniated and nitrated aerosols play a role in cirrus cloud formation.^{87,88,89} Laboratory data to support these findings, however, is sparse. Freezing studies on the following aerosols would further our understanding of cirrus cloud formation: (NH₄)₂SO₄, NH₄H₂PO₄, and NH₄NO₃. These aerosols are just a few of the much larger number of atmospherically relevant aerosols that need to be studied.

Although the apparatus developed during the course of this PhD work is adequate for most of the studies proposed above, the addition of an instrument capable of determining the composition of any aerosol (volatile at room temperature or non-volatile at room temperature) would make a substantial improvement to the current apparatus. An example of an essentially universal technique for compositional analysis is single particle mass spectroscopy (SPMS).^{90,91} This technique involves sampling the aerosol particles into a high vacuum chamber, vaporizing the particles with a laser or a filament, and analysing the resulting vapor with a mass spectrometer. With the addition of this type of instrument, a wider range of systems could be investigated.

Another possible avenue to follow in this research is atmospheric heterogeneous chemistry. The apparatus described in this thesis would be an ideal initial stage to a second flow tube where heterogeneous reactions could be investigated; that is, the current apparatus would produce and supply particles to a second flow tube where a trace gas would be introduced into the aerosol stream. With appropriate methods for trace gas analysis, the rates and products of the heterogeneous reactions could be monitored. This set-up would allow the unique opportunity to monitor a reaction between a gas and an aerosol while the phase of the aerosol is varied.

Clearly, the possibilities for future work are numerous.....

REFERENCES

1. Molina, M.J.; Rowland, F.S. *Nature* **1974**, *249*, 810.
2. Molina, L.T.; Molina, M.J. *J. Phys. Chem.* **1985**, *89*, 3779.
3. Farman, J.C.; Gardiner, B.G.; Shanklin, J.D. *Nature* **1985**, *315*, 207.
4. Solomon, S.; Garcia, R.R.; Rowland, F.S.; Wuebbles, D.J. *Nature* **1986**, *321*, 755.
5. Toon, O.B.; Hamill, P.; Turco, R.P.; Pinto, J. *Geophys. Res. Lett.* **1986**, *13*, 1284.
6. Solomon, S. *Rev. Geophys.* **1988**, *26*, 131.
7. Solomon, S. *Nature* **1990**, *347*, 347.
8. Ravishankara, A.R.; Hanson, D.R. *J. Geophys. Res.* **1996**, *101*, 3885.
9. Del Negro, L.A. *et al. J. Geophys. Res.* **1997**, *102*, 13255.
10. Poole, L.R.; McCormick, M.P. *Geophys. Res. Lett.* **1988**, *15*, 21.
11. Fahey, D.W.; Kelly, K.K.; Ferry, G.V.; Poole, L.R.; Wilson, J.C.; Murphy, D.M.; Loewenstein, M.; Chan, K.R. *J. Geophys. Res.* **1989**, *94*, 11299.
12. Toon, O.B.; Browell, E.V.; Kinne, S.; Jordan, J. *Geophys. Res. Lett.* **1990**, *17*, 393.
13. Browell, E.V. *et al. Geophys. Res. Lett.* **1990**, *17*, 385.
14. Hanson, D.; Mauersberger, K. *Geophys. Res. Lett.* **1988**, *15*, 855.
15. Ritzhaupt, G.; Devlin, J.P. *J. Phys. Chem.* **1991**, *95*, 90.
16. Worsnop, D.R.; Fox, L.E.; Zahniser, M.S.; Wofsy, S.C. *Science* **1993**, *259*, 71.
17. Marti, J.J.; Mauersberger, K. *J. Phys. Chem.* **1994**, *98*, 6897.
18. Fox, L.E.; Worsnop, D.R.; Zahniser, M.S.; Wofsy, S.C. *Science* **1995**, *267*, 351.
19. Zhang, R.; Wooldridge, P.J.; Abbatt, P.D.; Molina, M. *J. Phys. Chem.* **1993**, *97*, 8541.
20. Koop, T.; Carslaw, K.S.; Peter, T. *Geophys. Res. Lett.* **1997**, *24*, 2199.
21. Pool, L.R.; McCormick, M.P. *J. Geophys. Res.* **1988**, *93*, 8423.
22. Carslaw, K.S.; Luo, B.P.; Clegg, S.L.; Peter, T.; Brimblecombe, P.; Crutzen, P.J. *Geophys. Res. Lett.* **1994**, *21*, 2479.
23. Tabazadeh, A.; Turco, R.P.; Drdla, K.; Jacobson, M.Z.; Toon, O.B. *Geophys. Res. Lett.* **1994**, *21*, 1619.

24. Molina, M.J.; Zhang, R.; Wooldridge, P.J.; McMahon, J.R.; Kim, J.E.; Chang, H.Y.; Beyer, K.D. *Science* **1993**, *261*, 1418.
25. Koop, T.; Biermann, U.M.; Raber, W.; Luo, B.P.; Crutzen, P.J.; Peter, T. *Geophys. Res. Lett.* **1995**, *22*, 917.
26. Meilinger, S.K.; Koop, T.; Luo, B.P.; Huthwelker, T.; Carslaw, K.S.; Krieger, U.; Crutzen, P.J.; Peter, T. *Geophys. Res. Lett.* **1995**, *22*, 3031.
27. Tsias, A.; Prenni, A.J.; Carslaw, K.S.; Onasch, T.P.; Luo, B.P.; Tolbert, M.A.; Peter, T. *Geophys. Res. Lett.* **1997**, *24*, 2303.
28. Hagen, D.E.; Anderson, R.J.; Kassner, J.L.Jr. *J. Atmos. Sci.* **1981**, *38*, 1236.
29. Rawson, H. *Properties and Applications of Glass*, Elsevier Scientific Publishing Co., New York, 1980.
30. Varshneya, A.K. *Fundamentals of Inorganic Glasses*, Academic, San Diego, 1994.
31. Zarzycki, J. *Glasses and the Vitreous State*, Cambridge Univ. Press, New York, 1991.
32. Beyer, K.D.; Seago, S.W.; Chang, H.Y.; Molina, M.J. *Geophys. Res. Lett.* **1994**, *21*, 871.
33. Song, N. *Geophys. Res. Lett.* **1994**, *21*, 2709.
34. Middlebrook, A.M.; Berland, B.S.; George, S.M.; Tolbert, M.A.; Toon, O.B. *J. Geophys. Res.* **1994**, *99*, 25655.
35. Iraci, L.T.; Middlebrook, A.M.; Tolbert, M.A. *J. Geophys. Res.* **1995**, *100*, 20969.
36. Flagan, R.C.; Seinfeld, J.C. *Fundamentals of Air Pollution Engineering*, Prentice-Hall, New Jersey, 1988.
37. Fuchs, N.A. *The Mechanics of Aerosols*, Pergamon Press, New York, 1964.
38. Tang, I.N.; Munkelwitz, H.R.; Davis, J.G. *J. Aerosol Sci.* **1977**, *8*, 149.
39. Mozurkewich, M.; Calvert, J.G. *J. Geophys. Res.* **1988**, *93*, 15889.
40. Fried, A.; Henry, B.E.; Calvert, J.G.; Mozurkewich, M. *J. Geophys. Res.* **1994**, *99*, 3517.
41. Reist, P.C. *Aerosol Science and Technology*, McGraw-Hill Inc., New York, 1993.
42. Bohren, C.F.; Huffman, D.R. *Absorption and Scattering of Light by Small Particles*, Wiley, New York, 1983.

43. Van de Hulst, H.C. *Light Scattering by Small Particles*, Wiley and Sons, New York, 1957.
44. Kerker, M. *The Scattering of Light and Other Electromagnetic Radiation*, Academic Press, New York, 1969.
45. Pope, S.K.; Tomasko, M.G.; Williams, M.S.; Perry, M.L.; Doose, L.R.; Smith, P.H. *Icarus* **1992**, *100*, 203.
46. Perry, R.J.; Huffman, D.R. *Appl. Opt.* **1978**, *17*, 2700.
47. Holland, A.C.; Draper, J.S. *Appl. Opt.* **1967**, *6*, 511.
48. Turco, R.P.; Whitten, R.C.; Toon, O.B. *Rev. Geophys.* **1982**, *20*, 233.
49. Hofmann, D.J. *Rev. Geophys.* **1987**, *25*, 734.
50. Steele, H.M.; Hamill, P. *J. Aerosol. Sci.* **1981**, *12*, 517.
51. Tabazadeh, A.; Toon, O.B.; Clegg, S.L.; Hamill, P. *Geophys. Res. Lett.* **1997**, *24*, 1931.
52. Gable, C.M.; Betz, H.F.; Maron, S.H. *J. Am. Chem. Soc.* **1950**, *72*, 1445.
53. Luo, B.; Peter, T.; Crutzen, P.J. *Ber. Bunsen Ges. Phys. Chem.* **1992**, *96*, 334.
54. Luo, B.P.; Peter, T.; Crutzen, P. *Geophys. Res. Lett.* **1994**, *21*, 1447.
55. Jensen, E.J.; Toon, O.B. *Geophys. Res. Lett.* **1991**, *18*, 1857.
56. Middlebrook, A.M.; Iraci, L.T.; McNeill, L.S.; Koehler, B.G.; Wilson, M.A.; Daastad, O.W.; Tolbert, M.A.; Hanson, D.R. *J. Geophys. Res.* **1993**, *98*, 20473.
57. Ohtake, T. *Tellus* **1993**, *45*, 138.
58. Bertram, A.K.; Patterson, D.D.; Sloan, J.J. *J. Phys. Chem.* **1996**, *100*, 2376.
59. Palmer, K.F.; Williams, D. *Appl. Opt.* **1975**, *14*, 208.
60. Anthony, S.E.; Tisdale, R.T.; Disselkamp, R.S.; Tolbert, M.A.; Wilson, J.C. *Geophys. Res. Lett.* **1995**, *22*, 1105.
61. Giguere, P.A.; Savoie, R. *J. Am. Chem. Soc.* **1963**, *85*, 287.
62. Jensen, E.J.; Toon, O.B.; Westphal, D.L.; Kinne, S.; Heymsfeld, A.J. *J. Geophys. Res.* **1994**, *99*, 10421.
63. Jensen, E.J.; Toon, O.B. *Geophys. Res. Lett.* **1994**, *21*, 2019.
64. Pruppacher, H.R.; Klett, J.D. *Microphysics of Clouds and Precipitation*, Reidel Publishing Co., Boston, 1978.

65. MacKenzie, A.R.; Laaksonen, A.; Evangelos, B.; Kulmala, M. *J. Geophys. Res.* **1998**, *103*, 10875.
66. Clapp, M.L.; Niedziela, R.F.; Richwine, L.J.; Dransfield, T.; Miller, R.E.; Worsnop, D.R. *J. Geophys. Res.* **1997**, *102*, 8899.
67. Carleton, K.L.; Sonnenfroh, D.M.; Rawlins, W.T.; Wyslouzil, B.E.; Arnold, S. *J. Geophys. Res.* **1997**, *102*, 6025.
68. Martin, S.T.; Salcedo, D.; Molina, L.T.; Molina, M.J. *J. Phys. Chem. B* **1997**, *101*, 5307.
69. Imre, D.G.; Xu, J.; Tridico, A.C. *Geophys. Res. Lett.* **1997**, *24*, 69.
70. Koop, T.; Luo, B.; Biermann, U.M.; Crutzen, P.J.; Peter, T. *J. Phys. Chem. A* **1997**, *101*, 1117.
71. Kuster, F.W.; Kremann, R.Z. *Anorg. Chem.* **1904**, *41*, 1.
72. Ji, K. *Etudes de la compositions des aerosols stratospheriques polaires au moyen des diagrammes de phase stables, metastables et cinetiques des systems: HNO₃/H₂O HCl/H₂O et H₂SO₄/H₂O*, Ph.D. Thesis, L'universite de paris, Paris, 1994.
73. Hanson, D; Mauersberger, K. *J. Phys. Chem.* **1988**, *92*, 6167.
74. Tolbert, M.A.; Middlebrook, A.M. *J. Geophys. Res.* **1990**, *95*, 22423.
75. Koehler, B.G.; Middlebrook, A.M.; Tolbert, M.A. *J. Geophys. Res.* **1992**, *97*, 8065.
76. Bertram, A.K.; Sloan, J.J. *J. Geophys. Res.* **1998**, *103*, 3553.
77. Bertram, A.K.; Sloan, J.J. *J. Geophys. Res.* **1998**, *103*, 13261.
78. Toon, O.B.; Tolbert, M.A.; Koehler, B.G.; Middlebrook, A.M.; Jordan, J. *J. Geophys. Res.* **1994**, *99*, 25631.
79. Barton, N.; Rowland, B.; Devlin, J.P. *J. Phys. Chem.* **1993**, *97*, 5848.
80. Tisdale, R. T.; Middlebrook, A. M.; Prenni, A. J.; Tolbert, M. A. *J. Phys. Chem. A* **1997**, *101*, 2112.
81. Disselkamp, R.S.; Anthony, S.E.; Prenni, A.J.; Onasch, T.B.; Tolbert, M.A. *J. Phys. Chem.* **1996**, *100*, 9127.
82. Peter, T. *Annu. Rev. Phys. Chem.* **1997**, *48*, 785.
83. Richwine, L.J.; Clapp, M.L.; Miller, R.E.; Worsnop, D.R. *Geophys. Res. Lett.* **1995**, *22*, 2625.

84. Satoh, K.; Kanno, H. *Bull. Chem. Soc. Jpn.* **1982**, *55*, 1645.
85. Taleb, D; Ponche, J.; Mirabel, P. *J. Geophys. Res.* **1996**, *101*, 25967.
86. Tabazadeh, A.; Toon, O.B.; Jensen, E.J. *Geophys. Res. Lett.* **1997**, *24*, 2007.
87. Tabazadeh, A; Toon, O.B. *Geophys. Res. Lett.* **1998**, *25*, 1379.
88. Talbot, R.W.; Dibb, J.E.; Loomis, M.B. *Geophys. Res. Lett.* **1998**, *25*, 1367.
89. Jensen, E.J. *et al.* *Geophys. Res. Lett.* **1998**, *25*, 1363.
90. Allen, J.; Gould, R.K. *Rev. Sci. Instrum.* **1981**, *52*, 804.
91. Thomson, D.S.; Murphy, D.M. *Appl. Opt.* **1993**, *32*, 6818.